

AD \_\_\_\_\_

GRANT NUMBER DAMD17-96-1-6010

TITLE: Microvasculature Magnetic Resonance Imaging for the  
Diagnosis of Breast Cancer

PRINCIPAL INVESTIGATOR: Cynthia F. Maier  
Brian K. Rutt, Ph.D.

CONTRACTING ORGANIZATION: John P. Robarts Research Institute  
London, Ontario, Canada N6A 5K8

REPORT DATE: June 1997

TYPE OF REPORT: Annual

PREPARED FOR: Commander  
U.S. Army Medical Research and Materiel Command  
Fort Detrick, Frederick, Maryland 21702-5012

DISTRIBUTION STATEMENT: Approved for public release;  
distribution unlimited

The views, opinions and/or findings contained in this report are those of the author(s) and should not be construed as an official Department of the Army position, policy or decision unless so designated by other documentation.

**DMIC QUALITY INSPECTED 2**

**19971210 037**

# REPORT DOCUMENTATION PAGE

Form Approved  
OMB No. 0704-0188

Public reporting burden for this collection of information is estimated to average 1 hour per response, including the time for reviewing instructions, searching existing data sources, gathering and maintaining the data needed, and completing and reviewing the collection of information. Send comments regarding this burden estimate or any other aspect of this collection of information, including suggestions for reducing this burden, to Washington Headquarters Services, Directorate for Information Operations and Reports, 1215 Jefferson Davis Highway, Suite 1204, Arlington, VA 22202-4302, and to the Office of Management and Budget, Paperwork Reduction Project (0704-0188), Washington, DC 20503.

1. AGENCY USE ONLY (Leave blank)		2. REPORT DATE June 1997		3. REPORT TYPE AND DATES COVERED Annual (1 May 96 - 30 Apr 97)	
4. TITLE AND SUBTITLE Microvasculature Magnetic Resonance Imaging for the Diagnosis of Breast Cancer				5. FUNDING NUMBERS DAMD17-96-1-6010	
6. AUTHOR(S) Cynthia F. Maier Brian K. Rutt, Ph.D.					
7. PERFORMING ORGANIZATION NAME(S) AND ADDRESS(ES) John P. Robarts Research Institute London, Ontario, Canada N6A 5K8				8. PERFORMING ORGANIZATION REPORT NUMBER	
9. SPONSORING/MONITORING AGENCY NAME(S) AND ADDRESS(ES) Commander U.S. Army Medical Research and Materiel Command Fort Detrick, Frederick, Maryland 21702-5012				10. SPONSORING/MONITORING AGENCY REPORT NUMBER	
11. SUPPLEMENTARY NOTES					
12a. DISTRIBUTION / AVAILABILITY STATEMENT Approved for public release; distribution unlimited				12b. DISTRIBUTION CODE	
13. ABSTRACT (Maximum 200)  The work comprising this thesis is directed toward developing new techniques for measuring tumor blood flow in human breast lesions using MRI. The first section of this thesis addresses the underlying biological question of whether malignant breast lesions can be distinguished from benign lesions on the basis of microvessel density and flow. Since there are currently no techniques available for measuring flow in these vessels <i>in vivo</i> , histology techniques are used to compare the distribution of blood vessels in malignant lesions to benign breast lesions. A second major focus of this thesis describes the design and construction of a prototype breast gradient coil set to be used as a hardware add-on with the regular clinical MR scanner. This gradient coil design will allow IVIM techniques to be implemented on the clinical MR scanner for patient evaluation. The third section of this thesis involves the application of a new MRI method for measuring blood flow in the microvasculature, Intravoxel Incoherent Motion imaging (IVIM), to an animal model of tumor blood flow. If successful, IVIM imaging will non-invasively measure blood flow in tumor microvessels, and will also provide a direct visualization of the spatial distribution of these microvessels around tumors.					
14. SUBJECT TERMS Breast Cancer				15. NUMBER OF PAGES 70	
				16. PRICE CODE	
17. SECURITY CLASSIFICATION OF REPORT Unclassified	18. SECURITY CLASSIFICATION OF THIS PAGE Unclassified	19. SECURITY CLASSIFICATION OF ABSTRACT Unclassified	20. LIMITATION OF ABSTRACT Unlimited		

## **REPRODUCTION QUALITY NOTICE**

**This document is the best quality available. The copy furnished to DTIC contained pages that may have the following quality problems:**

- **Pages smaller or larger than normal.**
- **Pages with background color or light colored printing.**
- **Pages with small type or poor printing; and or**
- **Pages with continuous tone material or color photographs.**

**Due to various output media available these conditions may or may not cause poor legibility in the microfiche or hardcopy output you receive.**



**If this block is checked, the copy furnished to DTIC contained pages with color printing, that when reproduced in Black and White, may change detail of the original copy.**

FOREWORD

Opinions, interpretations, conclusions and recommendations are those of the author and are not necessarily endorsed by the U.S. Army.

\_\_\_\_ Where copyrighted material is quoted, permission has been obtained to use such material.

\_\_\_\_ Where material from documents designated for limited distribution is quoted, permission has been obtained to use the material.

\_\_\_\_ Citations of commercial organizations and trade names in this report do not constitute an official Department of Army endorsement or approval of the products or services of these organizations.

✓ \_\_\_\_ In conducting research using animals, the investigator(s) adhered to the "Guide for the Care and Use of Laboratory Animals," prepared by the Committee on Care and Use of Laboratory Animals of the Institute of Laboratory Resources, National Research Council (NIH Publication No. 86-23, Revised 1985).

✓ \_\_\_\_ For the protection of human subjects, the investigator(s) adhered to policies of applicable Federal Law 45 CFR 46.

\_\_\_\_ In conducting research utilizing recombinant DNA technology, the investigator(s) adhered to current guidelines promulgated by the National Institutes of Health.

\_\_\_\_ In the conduct of research utilizing recombinant DNA, the investigator(s) adhered to the NIH Guidelines for Research Involving Recombinant DNA Molecules.

\_\_\_\_ In the conduct of research involving hazardous organisms, the investigator(s) adhered to the CDC-NIH Guide for Biosafety in Microbiological and Biomedical Laboratories.

Cynthia F. Wain      July 27 '97  
PI - Signature                      Date

## Table of Contents

Standard Form (SF) 298, Report Documentation Page .....	i
Foreword .....	ii
Table of Contents .....	iii

## 1: Introduction

1.1 Diagnosis of Breast Cancer .....	1
1.2 Patient Prognosis .....	1
1.3 Tumour Angiogenesis .....	2
1.3.1 Implications for Diagnosis .....	3
1.3.2 Implications for Prognosis .....	3
1.4 Magnetic Resonance Imaging .....	4
<b>2: Distribution of Microvessels in Human Breast Lesions .....</b>	<b>6</b>
<b>3: Development of Hardware for Microvessel/Diffusion Breast Imaging ....</b>	<b>6</b>
<b>4: Diffusion Imaging in Implanted Human Breast Tumours .....</b>	<b>8</b>
<b>5: Microvascular Imaging In Implanted Human Breast Tumours .....</b>	<b>8</b>
<b>6: Conclusions .....</b>	<b>11</b>
<b>7: References .....</b>	<b>12</b>
<b>Appendix 1 .....</b>	<b>17</b>
<b>Appendix 2 .....</b>	<b>29</b>
<b>Appendix 3 .....</b>	<b>53</b>
<b>Appendix 4 .....</b>	<b>59</b>

## **1. Introduction**

### **1.1 Diagnosis of Breast Cancer**

X-ray mammography is the current gold standard in breast imaging and, in combination with a physical exam, detects breast cancer with a sensitivity of 85-95%. [1,2] Diagnosis of detected focal abnormalities is based primarily on morphological features such as boundary appearance, presence or absence of spiculations, and distribution and size of calcifications. Some lesions can be characterized specifically as either benign or malignant on the basis of these features alone; however, many are indeterminate, and require further evaluation. [3,4] Recent trials have shown that 70-80% of mammographically indeterminate lesions that progress to surgical biopsy are benign. [4-7] For women with particularly dense breast tissue and/or fibrocystic changes, the false positive rate for x-ray mammography can be as high as 90%. [5,8] For these women, the surgical biopsy serves only to provide a diagnosis since it is not necessary to remove a benign lesion unless it is causing pain.

Recently, less invasive biopsy techniques have been developed which use a large diameter needle fitted with a cutting device to extract cores of tissue from a lesion for histological analysis. In the case of a solid, palpable lesion, core biopsy is sometimes used to provide a definitive diagnosis even in the case of a negative result; however, this application is still very controversial. [9-12] Although the reported accuracy of this core biopsy technique in small studies has improved rapidly since its inception (largely because of improved sampling accuracy using needle guidance by imaging methods), a conservative approach demands more extensive testing in large populations with surgical confirmation before a meaningful evaluation of its reliability can take place. [13]

Development of accurate, non-invasive methods for characterizing mammographically indeterminate lesions represents an active area of current research in medical imaging. Ideally, a new diagnostic test would have reliably low false negative rates and would significantly reduce the number of surgical biopsies for benign lesions currently being performed; however, even if the false-negative rate associated with the test were unacceptably high, a non-invasive test with high positive predictive value for malignancy would have a profound impact on current surgical practice for breast cancer. At present, patients undergo surgical biopsy, then return for a second surgical procedure if the biopsy is positive, allowing time for patients to assess their treatment options in the intervening weeks. A non-invasive predictor of malignancy could eliminate this two-step procedure, reducing the risk of disease progression and the psychological stress of delaying treatment.

### **1.2 Patient Prognosis**

In 1990, Fearon and Vogelstein published their work elucidating the genetic steps to malignancy in colon cancer. [14] It is now widely believed that breast cancer also evolves in a similar way from normal ductal epithelium, to hyperplasia, to atypical hyperplasia, to carcinoma *in situ* and finally to invasive carcinoma. [15] At each stage in this progression away from normal epithelium toward malignancy and invasion, the prognosis for the patient worsens. Following a surgical biopsy, the extent of malignant transformation is determined and the metastatic potential of a tumor evaluated to best determine clinical treatment.

The recent technical improvements in mammography and increase in the number of women who undergo screening have dramatically shifted the stage of cancers seen at pathology. Approximately 66% of patients with newly detected breast cancer will have no detected lymph node involvement, and 20-30% of these newly-detected lesions will be found while still confined within a duct. [4,6] Fifteen to twenty per cent of node-negative patients with invasive carcinoma will relapse in the 10 years following surgery. [16] Currently, there is no proven technique for identifying this high-risk subpopulation within the node-negative group. For these women, standard pathological indicators such as tumour size, histologic differentiation, and hormone receptor status have shown variable correlation with disease recurrence and patient survival. [17] For these localized breast cancers, surgical removal of the tumour supplemented by radiation therapy has replaced mastectomy for many women. [18,19] The development of prognostic indicators to identify patients from this group who are likely to benefit from systemic chemotherapy is also an active and important area of current research. Currently, there are no accepted guidelines for clinical treatment of women with ductal carcinoma *in situ* (DCIS). [20] Clinical care of patients with early-stage breast cancer is controversial, and the development of a test to assess the metastatic potential of these lesions is an important area of research in breast pathology.

A large body of recent work exists concerning the development of new prognostic indicators for early-stage carcinomas. The list of new markers currently being evaluated is long and growing. New markers which show promise are those reflecting cellular characteristics such as DNA content, ploidy (define), cell cycle status, and proliferation indices. In addition, new genetic tests are being created to evaluate the expression of oncogenes. For example, the tumour suppressor p53 gene has been receiving much attention as a prognostic indicator. Overexpression of the p53 mutant form has been found to correlate with high proliferative activity and disease recurrence in some studies. [21] Unfortunately, these relationships have not been found in all cases, [22] and this new area of research is in need of more concrete results before these indicators can be used routinely for clinical decision-making. None of the multitude of currently available prognostic tests are sufficiently reliable for predicting relapse or survival, and decisions about patient care must be made by weighing many prognostic indicators, in addition to assessing individual patients' needs.

### 1.3 Tumour Angiogenesis

Tumour progression is known to be dependent on the ability to stimulate the growth of new blood vessels. [23] This process, known as tumour angiogenesis, is integral to all solid malignant neoplasms, and is required in order to supply nutrients and oxygen to the expanding tumour. In tumour spheroids, transport of nutrients and oxygen by diffusion was shown to limit tumour growth to a size of 1-2 mm diameter. [24-26] In a chick embryo model, however, implanted tumour cells were shown to stimulate the growth of new blood vessels, and to thereby achieve rapid growth beyond this diffusion-limited size constraint. [27] It was therefore believed initially that the switch to an angiogenic phenotype would occur when a tumour reaches its maximum diffusion-limited growth potential. More recent results have indicated that the onset of

angiogenesis can occur much earlier in tumour progression, and may even occur well before the switch to a malignant phenotype. [28] Recent studies evaluating microvessel density around *in situ* breast carcinoma have shown increased vascularity even around these very early stage lesions. [29-31] More strikingly, cells extracted from premalignant lesions have demonstrated the ability to induce new vessel formation in model tissue systems. Using a rabbit cornea assay, cells extracted from atypical hyperplasia and even from histologically normal lobules from cancerous breasts have been shown to stimulate angiogenesis. [32-35] Although these results are preliminary, and mechanisms of angiogenesis are still not fully understood, it is evident that even very early malignancies, and some premalignant lesions undergo marked changes in vasculature.

**1.3.1 Implications for Diagnosis:** It has been hypothesized that the characteristic new vessel growth associated with tumour angiogenesis could allow differentiation between malignancies and benign breast lesions using medical imaging techniques. [36-40] Specifically, it has been speculated that the number of small vessels per unit volume of tissue (microvessel density) would be higher for malignant lesions. Some imaging researchers have even asserted that benign lesions are not expected to be vascularized at all, and that the detection of blood flow around a lesion would therefore strongly indicate malignancy. Although countless attempts premised on this assumption have been made to diagnose breast disease using IR thermography, positron emission tomography, Doppler ultrasound, and magnetic resonance imaging techniques, none of these studies has achieved the highly reliable differentiation between benign and malignant lesions that was expected. This has led some authors to suggest that the absolute number of microvessels in benign and malignant lesions may overlap in some cases. More hopefully, several recent imaging studies have suggested that an increased number of these vessels specifically in the lesion periphery may be a characteristic that is uniquely associated with malignancy. [41,42]

To date, most studies evaluating microvessel density in breast using histological techniques have focussed on invasive breast carcinomas, and the increased number of blood vessels associated with a strong tendency to metastasize. Although comparisons of microvessel density to normal breast tissue have been made, relatively few of these studies have included benign breast lesions, and very little data about vascularity in benign tumours is actually available. The hypothesis of benign lesions being avascular appears to have been based almost solely on what is known about breast cancers, extrapolating through "less invasive" to "benign". If the number of blood vessels or their spatial distribution around malignant lesions is, in fact, characteristic for malignancy, a non-invasive measure of blood flow around an indeterminate lesion would add valuable information to a diagnostic work-up; however, histological studies evaluating distributions of vessels in benign lesions are certainly required to test this hypothesis.

**1.3.2 Implications for Prognosis:** The entry of cancer cells into the bloodstream and subsequent formation of distant metastases is facilitated by the increasing number of small new blood vessels around the tumour as it grows. Studies of patients with invasive breast carcinoma have shown that the number of microvessels in angiogenic "hotspots" in the tumour periphery correlates strongly with the extent of metastatic progression. [43-47] In one study, each 10-fold increase in the number of microvessels per x200 microscope field corresponded to a 1.6-fold



increase in the risk of metastasis. [43] The number of microvessels in these hotspots has also been shown to outperform lymph-node positivity as a predictor for the development of distant metastatic disease. [44-46] Moreover, microvessel density is the only prognostic indicator that is a statistically significant predictor of overall survival for node-negative women. [44,47] A non-invasive diagnostic technique that measures microvessel density in invasive carcinomas would identify node-negative lesions with high metastatic potential and would immediately indicate which patients are most likely to benefit from adjuvant systemic therapy.

A measurement of microvessel density may also have value in prognosis for *in situ* carcinoma and for premalignant disease. It has been proposed that the degree of angiogenic activity around premalignant lesions and early-stage cancers may be an indicator of which lesions will progress to more invasive disease. [48] Preliminary results from a retrospective study by Guinebreiere [49] showed that vessel density around hyperplastic lesions correlated with risk for subsequent development of invasive carcinoma and, further, that vessel density had a higher prognostic value than atypia. A non-invasive method for measuring microvessel density around premalignant lesions and *in situ* cancers may provide early identification of lesions that have the potential to progress to more invasive disease, and require more aggressive therapy, or long-term patient follow-up.

#### 1.4 Magnetic Resonance Imaging (MRI)

Breast imaging using MRI has several advantages over x-ray mammography: (a) image contrast can be based on one or more of several independent tissue parameters (T1, T2 and water content) and can therefore be manipulated to optimize contrast between lesions and normal parenchymal tissue, (b) optimal display of tissue close to the chest wall can be obtained, since no compression of the breast is required, (c) images are obtained either as 2-dimensional slices in any orientation, or as 3-dimensional volumes, eliminating overlap of internal breast structures on the image.

The focus of research in MR imaging of the breast has been on contrast-enhanced studies. It was originally believed that these contrast exams would distinguish malignant lesions from benign tumours with a high degree of reliability, since microvessels associated with malignant lesions were thought to be more numerous and more permeable than in normal tissue. Initially, simple snapshot "before" and "after" images were acquired, and areas of focal enhancement were evaluated for percentage signal increase. These MR studies reported detection of breast cancer with high sensitivity; however, diagnostic specificity was widely variable across different studies (20-85%). [50-53] Most solid malignancies showed marked contrast enhancement, allowing easy differentiation from mammographically similar features such as cysts, old scar tissue, and dense normal breast tissue. Unfortunately, some benign diseases such as atypical hyperplasia and fibroadenomas showed similar absolute enhancement to malignancies, and some malignancies demonstrated benign-type enhancement.

Despite widespread efforts to refine MR techniques and analysis of these contrast-enhanced studies, little improvement in specificity resulted. [39,42,54-56] Extremely high sensitivity to cancer using this method is reported (94-100%); unfortunately, a large number of false positives has also been reported, where the majority of enhancing benign lesions are fibroadenomas or fibrocystic change.

Recently, new MR hardware has become commercially available that allows higher spatial resolution imaging (300-700  $\mu\text{m}$  in-plane resolution with 2-3 mm slice thickness). This improved resolution allows more detailed evaluation of lesion borders, and internal structure. In an initial study of patients with a palpable or mammographically visible mass, a high spatial resolution image was obtained before contrast agent injection, a series of lower spatial resolution images was acquired rapidly during the first 4-7 minutes post-injection to obtain high temporal resolution enhancement curves, and a second high spatial resolution image was then acquired using identical parameters to the first image. [41] These preliminary high spatial resolution contrast imaging results have indicated that the additional information about architectural features combined with initial slope calculations may result in increased specificity for breast cancer. Specifically, it was found that malignancies tended to demonstrate higher contrast enhancement around the lesion periphery and also tended to have spiculated borders, whereas benign lesions such as fibroadenomas exhibited a more diffuse, uniform enhancement with smooth borders. In a further study looking specifically at patients with DCIS, this technique detected ten of thirteen DCIS lesions, where three of the ten identified lesions were not visible on mammography. [57] These results have demonstrated considerable promise for combining information about tumour blood flow with high-resolution imaging techniques.

Although initial high-spatial resolution contrast-enhanced imaging results are promising, a fundamental problem with contrast-enhanced methods is that the signal enhancement seen reflects two inseparable aspects of tumour blood vessels: total vessel surface area within a voxel, and vessel permeability. Moreover, contrast exams are expensive and contrast agents are not well-tolerated by all patients. A non-invasive technique that is sensitive to only one aspect of the vasculature e.g. blood flow rate provides simpler interpretation.

The goal of this thesis was to test the feasibility of using the Intravoxel Incoherent Motion Imaging technique (IVIM) to measure microvessel blood flow around human breast lesions. IVIM is essentially a modification of an established protocol used for over thirty years to measure small water motions due to diffusion. In IVIM imaging, the same motion-sensitive protocols are used, where the protocols are tuned for sensitivity to the motion of the water component of blood flowing in small vessels. The IVIM technique has been demonstrated to be sensitive to blood flow in microvessels in the brain [58], and provides two quantitative measures: 1) absolute determination of the average blood flow velocity in these vessels within each tissue voxel, and 2) a relative measure of the total amount of blood flowing in these vessels at the time the image was acquired. It is possible that the measurement of these parameters in breast tissue may provide valuable information about microvessel densities and distributions around breast lesions.

The thesis outline is as follows: 1) The hypothesis that spatial distributions of blood vessels around a solid breast lesion is specific for malignancy was tested in a study of archival biopsy tissue stained for blood vessels; 2) Hardware necessary for the application of the IVIM technique to human breast cancer in a clinical setting was designed, constructed and tested for feasibility; 3) The IVIM method will be evaluated using a mouse tumour model, and blood-flow modifying agents to uniquely identify the small signal (5-10% of total signal) arising from the microvasculature.

## **2. Distributions of Microvessels in Breast Lesions**

A comparison study of spatial distributions of microvessels in human breast carcinomas and in fibroadenomas was carried out. Fibroadenomas were selected from other forms of benign breast disease for comparison to carcinomas because MR contrast enhancement patterns can often mimic those seen in invasive cancers. Moreover, fibroadenomas are the most commonly occurring benign solid lesion, and constitute 30-50% of benign lesions seen at surgical biopsy. [59]

Cases were selected from the files of the Department of Pathology at the London Health Sciences Centre, and were stained using Factor VIII-related antigen to identify endothelial cells. Microvessels were counted on x200 magnification in 10 fields in the lesion periphery, and 10 fields in the lesion centre. Where normal tissue was present, microvessels were also counted in 5 fields. The lesion periphery was easily identified on fibroadenomas as an enclosing fibrous capsule, and was defined as the leading edge of invading cells for the invasive carcinomas. Vessels were identified according to the criteria of Weidner et al. [43] where even a single stained endothelial cell was counted as a vessel.

A number of interesting results were obtained from this work. Many of the fibroadenomas in our sample contained, on average, more microvessels than some of the invasive carcinomas we looked at. This finding directly contradicts the assertion by imaging researchers that benign breast lesions are not vascularized, and also explains, to some extent, the overlap in imaging characteristics seen for fibroadenomas and breast cancers. On a more optimistic note, our findings revealed that the numbers of small vessels were higher around the boundaries of invasive carcinomas, whereas these small vessels were more uniformly distributed in fibroadenomas. This characteristic spatial distribution of blood vessels may allow differentiation between fibroadenomas and carcinomas using non-invasive imaging methods sensitized to flow in microvessels. A secondary, but interesting observation was that for the three women aged forty or older who had fibroadenomas, microvessel density in the surrounding normal breast tissue was extremely high compared with all other women in the fibroadenoma group (for the women with breast cancer, no "normal" tissue was present).

A manuscript describing this work is currently in preparation (included as Appendix 1). Portions of this work have been presented at the Annual Meeting of the United States and Canadian Academy of Pathology, Orlando, FL, March 1997; and have been accepted for presentation at this year's Annual Meeting of the Radiological Society of North America (RSNA) in November.

## **3: Development of Hardware for Microvessel/Diffusion Breast Imaging**

An ultra-high-strength 3-axis local gradient coil set was constructed for magnetic resonance imaging of the breast. This coil design will allow diffusion imaging and high-velocity-resolution blood flow imaging around human breast tumours in clinically acceptable exam times. These are the first specialized gradient coils for breast imaging to ever be presented (2nd Meeting of the Society of Magnetic Resonance, San Francisco, CA, August 1994), and are the first ultra-high-strength gradient coils (>200mT/m) designed for human imaging applications (for body parts

larger than fingers). The coils were tested using a grid phantom, and a diffusion phantom, and demonstrated excellent gradient uniformity and accurate diffusion measurement in the region of interest that we defined for breast imaging (based on common bra sizes).

The high gradient efficiencies of these coils will allow much higher spatial-resolution imaging than can currently be achieved in a clinical setting, and additionally, will provide very large amplitude motion-sensitizing gradients, thus facilitating diffusion imaging or flow imaging in small blood vessels while maintaining short echo times. T2 has been measured for human breast tissue, with reported values ranging between 60-150 ms. [60,61] Recently, we reported T2 ~ 70 ms for human breast tumour (MCF7 human breast carcinoma) growing in a mouse mammary fat pad. (Appendix 3) More fibrous tumours can have significantly shorter T2s. For this reason, initial signal loss at  $b=0$  s/mm<sup>2</sup> due to T2-weighting of the image can severely limit the range of b-factors for which images can be obtained, which has the result of limiting the precision of the ADC measurement. Our approach is to shorten TE while maintaining diffusion weighting by increasing diffusion gradient amplitudes. This gives a substantial increase in initial signal intensity for  $b=0$  s/mm<sup>2</sup>, allowing high quality images to be obtained for much higher b-factors. Even in cases where signal loss from T2-weighting is not so severe as to limit ADC precision, the ability to obtain high diffusion weighting with short TE reduces dramatically the T2 contrast in an image. This will allow acquisition of a diffusion-weighted image where the contrast is determined mainly by tissue ADC, rather than by a mix of ADC and T2.

#### Suggestions for Improvements:

Imaging results with these coils demonstrated excellent gradient uniformity for two of three axes in a large region near the top of the coils, and acceptable gradient uniformity for the third (Y) axis in a smaller region. Initially, the feasibility for using this coil design to measure diffusion and microvessel flow in breast lesions will be evaluated clinically by selecting women who have breast lesions that can be positioned inside our defined volume of interest; however, improvements on the electrical design of the Y gradient coil to provide more uniform gradients over a larger volume would allow scanning with a wider range of breast sizes.

The coils are not torque-balanced, and the horizontal return-wire plates experience strong forces in the upward/downward direction. It is possible to constrain the motion of the coils by an appropriately designed mounting system, but the design of such a system for human imaging is beyond the scope of this thesis, and will not be undertaken immediately. It was therefore decided that no human images would be obtained with the initial prototype coils built for this paper, and that subsequent prototypes would require extensive testing before an attempt to obtain images of a human breast would be made.

This paper (included as Appendix 2) has been submitted for publication as: **C.F. Maier**, H.N. Nikolov, K.C. Chu, B.A. Chronik, B.K. Rutt, "Practical Design of a High-Strength Gradient Coil for Diffusion and Microvascular Imaging of Breast Tumours", by *Magnetic Resonance in Medicine*. Portions of this work have been presented at: the 2nd Meeting of the Society of Magnetic Resonance, San Francisco, CA, August 1994 and the 3rd Meeting of the Society of Magnetic Resonance, Nice, France, August 1995. This work received the University of Western Ontario's Dean's Award for Excellence in Research (1995), and was an invited presentation at the Society of Magnetic Resonance Breast Imaging Workshop, Washington D.C., June 24-25, 1995.

#### **4: Diffusion Imaging in Implanted Human Breast Tumours**

Quantitative diffusion measurements were performed in tumours arising from inoculation of nude mice with human breast cancer cells to determine values for the Apparent Diffusion Coefficient for various components of solid tumours. Diffusion maps were compared to histology, and correlated well with gross tumour morphology. These diffusion measurements were carried out to provide a foundation for the implementation of IVIM experiments in these tumours, by characterizing the behavior of the signal arising from the static spins within the tissue. While these experiments were undertaken as a stepping-stone to IVIM imaging, the results are significant for researchers in cancer therapy, and show that the degree of necrosis resulting from a particular therapy can be monitored non-invasively using MRI.

These experiments were carried out under the supervision of Dr. Degani, Dr. Rutt, and Dr. Bendel. All experiments were performed at the Weizmann Institute of Science in Rehovot, Israel in the lab of Dr. Degani, and this work was completed prior to funding by the U.S. Army Predoctoral Fellowship award. In addition to providing details related to water diffusion in tumours necessary for planning the IVIM experiments, this work was highly valuable as a learning experience. By performing these experiments in Dr. Degani's lab, I was able to benefit from her years of experience working with this tumour cell line in nude mice, and also from Dr. Bendel's MR imaging expertise.

Ideally, IVIM experiments would have also been undertaken in Dr. Degani's lab; unfortunately, the limited length of my stay there (4 1/2 months) did not allow for the extensive software and hardware testing that is required for such sensitive work. Diffusion imaging alone is highly demanding on MR system performance, and the ability to reliably extract information about 5-10% of the collected signal requires thorough and meticulous system evaluation. We have chosen to continue this work here in London, Ontario, on our newly acquired 4 Tesla whole-body imager.

A paper describing this work (included as Appendix 3) has been published as: **C.F. Maier**, Y. Paran, P. Bendel, B.K. Rutt, H. Degani, "Quantitative Diffusion Imaging in Implanted Human Breast Tumours". *Magnetic Resonance in Medicine*, **37**, pp.576-581, 1997. This work was also presented at the 4th Meeting of the International Society for Magnetic Resonance in Medicine, New York City, NY, April 1996.

#### **5: Microvascular Imaging in Implanted Human Breast Tumours**

In 1986, LeBihan recognized that under certain conditions, blood flow in randomly oriented capillaries could be considered as a "pseudo-diffusion" process and proposed using the PGSE method to visualize this microcirculatory flow (See Figure 1 in Appendix 3). [58] This application of the PGSE sequence to imaging flow in capillaries was called Intravoxel Incoherent Motion Imaging, since the condition for this flow to mimic a diffusion process is that the flow within a voxel be "incoherent" with respect to the imaging time.

For voxel-sizes that can be obtained clinically ( $1\text{mm}^3$ - $10\text{mm}^3$ ), we expect to find thousands of capillaries, with a more or less random distribution of orientations. Flow in these

vessels therefore resembles a random-walk or pseudo-diffusive motion which can be characterized by an ADC. The relationship of this ADC to the vascular geometry is governed by the flow velocity of water molecules inside the vasculature. If the length of time between diffusion-encoding pulses,  $\Delta$ , is small, the average velocity can be derived directly from the ADC and is not dependent on the capillary network geometry. To ensure that this requirement is met, it is important to use high gradient strengths for large values of  $b$  (rather than increasing  $b$  by extending  $\Delta$ ). Additionally, the use of large, short  $g$  pulses allows imaging with short TE, so that little signal loss occurs from T2 decay during the imaging sequence.

The total signal arising from a voxel consists of a contribution from spins flowing in the microcirculation (5-10% of total signal) and from spins undergoing Brownian diffusion in the tissue (90-95% of total signal). This signal will exhibit a biexponential decay when plotted against increasing values of  $b$ . The fraction of all MR-visible spins within a voxel which are moving in the microcirculation can be determined experimentally from this curve by comparing the amount of signal attenuation due to fast decay (area under the exponential characterized by  $D^*$ ) to the amount of signal attenuation from the "static component" (area under the exponential characterized by  $D$ , the ADC describing tissue water diffusion). Although this  $D^*$  decay is due to the spins that are *moving* within the microcirculation, and does not contain a contribution from static spins inside the vasculature, it is expected that the fraction of moving spins determined will be related to the density of capillaries within the tissue voxel.

Initial experiments to characterize the performance of our 4 Tesla MRI system for diffusion imaging are now underway. Accurate and reproducible diffusion measurements in a water phantom have been obtained on our system using a PGSE sequence with timing shown in Figure 1. These results are shown in Table I. ADCs determined for the three slice orientations were within 3% of each other; this small variation indicates that eddy currents from the imaging gradients are negligible for our system and the deviations from calculated  $b$ -values due to this effect are small.

**Table I.**

Slice Orientation	ADC
sag	$2.05 \pm .01$
cor	$2.13 \pm .01$
trans	$2.11 \pm .02$

An animal protocol has been approved by the University of Western Ontario Council on Animal Care (See Appendix 4). This protocol describes a first experiment which will be undertaken to test the validity of the IVIM method for measuring tumour blood flow. In this experiment, nicotinamide will be used to increase blood flow in a well-characterized, highly vascularized mouse melanoma model. During the administration of the nicotinamide, a series of MR images with identical IVIM-weighting ( $b < 100 \text{ s/mm}^2$ ) will be acquired, alternated with

highly diffusion-weighted images ( $b > 500$  s/mm<sup>2</sup>). If the IVIM hypothesis is correct, the IVIM-weighted image should show a decrease in signal intensity for well-vascularized areas of the tumour following the administration of nicotinamide. Ideally, the diffusion-weighted images will not show a corresponding change in signal intensity; this would mean that a blood-flow modulator could be used to isolate the IVIM signal without the requirement of performing an intermediate calculation to remove the signal arising from diffusing spins in the tissue. If these experiments are successful, further experiments using an animal model of human breast tumours (MCF7 cells implanted in nude mice) will be undertaken to fully characterize the IVIM characteristics of these tumours.

## **6. Conclusions:**

1. The fibroadenomas in our histological study of lesion vascularity contained, on average, more microvessels than some of the invasive carcinomas. This finding directly contradicts the assertion by imaging researchers that benign breast lesions are not vascularized.
2. The numbers of small vessels were higher around the boundaries of invasive carcinomas compared to the lesion centers, whereas small vessels were more uniformly distributed in fibroadenomas. This characteristic spatial distribution of blood vessels may allow differentiation between fibroadenomas and carcinomas using non-invasive imaging methods sensitized to flow in microvessels.
3. An ultra-high-strength 3-axis local gradient coil set was constructed for magnetic resonance imaging of the breast. This coil design will allow diffusion imaging and high-velocity-resolution blood flow imaging around human breast tumours in clinically acceptable exam times. Initial imaging and diffusion measurements using phantoms are promising and prove our design concept; however, construction of further prototypes and more extensive testing is required before human scanning may be safely undertaken.
4. Quantitative diffusion measurements were performed in MCF7 human breast tumours implanted in nude mice. Apparent Diffusion Coefficients were specific for various components of solid tumours (viable tumour, necrosis, fibrous tissue). Diffusion maps were compared to histology, and correlated well with gross tumour morphology. These measurements provide a foundation for the IVIM experiments that will be undertaken.



## 7. References

1. Schmitt, E. L. and Threatt, B. Characteristics of breast cancer in an incident cancer population. *Am.J.Roentgenol.* 143:402-406, 1984.
2. Xenophon, L. Imaging techniques for breast disease. *Clin.Obstet.Gynaecol.* 37 no.4:933-943, 1994.
3. Verbeek, A. L., Hendriks, J. H., Holland, R., Mravunac, M., Sturmans, F. and Day, N. E. Reduction of breast cancer mortality through mass screening with modern mammography: First results of the Nijmegen project, 1975-1981. *Lancet* 1(1):1222-1224, 1984.
4. Baker, L. H. Breast cancer detection demonstration project: Five-year summary report. *CA - A Cancer Journal for Clinicians* 32:194-225, 1982.
5. Williams, S. M., Kaplan, P. A., Petersen, J. C. and Lieberman, R. P. Mammography in women under age 30: Is there clinical benefit? *Radiology* 161:49-51, 1986.
6. Ciatto, S., Cataliotti, L. and Distante, V. Nonpalpable lesions detected with mammography: Review of 512 consecutive cases. *Radiology* 165:99-102, 1987.
7. Dershaw, D. D., Shank, B. and Reisinger, S. Mammographic findings after breast cancer treatment with local excision and definitive irradiation. *Radiology* 164:455-461, 1987.
8. Harris, V. J. and Jackson, V. P. Indications for breast imaging in women under age 35 years. *Radiology* 172:445-448, 1989.
9. Logan-Young, W. W., Janus, J. A., Destounis, S. V. and Yanes Hoffman, N. Appropriate role of core breast biopsy in the management of probably benign lesions. *Radiology* 190:313-314, 1994.
10. Jackman, R. J., Nowels, K. W., Shepard, M. J., Finkelstein, S. I. and Marzoni, F. A. Stereotaxic large-core needle biopsy of 450 nonpalpable breast lesion with surgical correlation in lesions with cancer or atypical hyperplasia. *Radiology* 193:91-95, 1994.
11. Liberman, L., Dershaw, D. D., Rosen, P. P., Giess, C. S., Cohen, M. A., Abramson, A. F. and Hann, L. E. Stereotaxic core biopsy of breast carcinoma: Accuracy at predicting invasion. *Radiology* 194:379-381, 1995.
12. Sullivan, D. C. Needle core biopsy of mammographic lesions. *Am.J.Roentgenol.* 162:601-608, 1994.
13. Kopans, D. B. Caution on core. *Radiology* 193:325-328, 1994.
14. Fearon, E. R. and Vogelstein, B. A genetic model for colorectal tumorigenesis. *Cell* 61:759-767, 1990.
15. Sato, T., Akiyama, F., Sakamoto, G., Kasumi, F. and Nakamura, Y. Accumulation of genetic alterations and progression of primary breast cancer. *Cancer Res.* 51:5794-5799, 1991.
16. Rosner, B. The role of adjuvant chemotherapy in early node-negative breast cancer. In: *Treatment of pre-cancerous lesions and early breast cancer*, edited by Arian, I.M. and Cahan, A.C. Baltimore: Williams and Wilkins, 1993,
17. McGuire, W. L., Tandon, A. K., Allred, D. C., Chamness, G. C. and Clark, G. M. How to use prognostic factors in axillary node-negative breast cancer patients. *J.Natl.Cancer Inst.* 82:1006-1015, 1990.
18. Bader, J., Lippman, M., Swain, S., Danforth, D., MacDonald, H., Gerber, L., Steinber, S.,

- D'Angelo, T. and Campbell, L. Preliminary report on the NCI early breast cancer study: A prospective randomized comparison of lumpectomy and radiation therapy to mastectomy for Stage I and II breast cancer. *Int.J.Radiat.Oncol.Biol.Phys.* 13 (Suppl):160, 1987.
19. Fisher, B., Redmond, C., Poisson, R., Margolese, R., Wolmark, N., Wickerham, L., Fisher, E., Deutsch, M., Caplan, R., Pilch, Y., Glass, A., Shibata, H., Lerner, H., Terz, J. and Sidorovich, L. Eight-year results of a randomized clinical trial comparing total mastectomy and lumpectomy with or without irradiation in the treatment of breast cancer. *New Engl.J.Med.* 320:822-828, 1989.
  20. Rosen, P.P. "Intraductal carcinoma" In: Rosen's breast pathology, Philadelphia: Lippincott-Raven, 1997, p. 227-273.
  21. Gasparini, G., Weidner, N. and Bevilacqua, P. Tumor microvessel density, p53 expression, tumor size, and peritumoral lymphatic vessel invasion are relevant prognostic markers in node-negative breast carcinoma. *J.Clin.Oncol.* 12:454-466, 1994.
  22. Mansour, E. G., Ravdin, P. M. and Dressler, L. Prognostic factors in early breast carcinoma. *Cancer Suppl.* 74 no.1:381-400, 1994.
  23. Folkman, J. What is the evidence that tumors are angiogenesis dependent? *J.Natl.Cancer Inst.* 82 no.1:4-6, 1990.
  24. Sutherland, R. M., McCredie, J. A. and Inch, W. R. Growth of multicell spheroids in tissue culture as a model of nodular carcinomas. *J.Natl.Cancer Inst.* 46:113-120, 1971.
  25. Folkman, J. and Hochberg, M. Self-regulation of growth in three dimensions. *J.Exp.Med.* 138:745-753, 1973.
  26. Sutherland, R. M. Cell and environment interactions in tumour microregions: The multicell spheroid model. *Science* 240:177-184, 1988.
  27. Knighton, D., Ausprunk, D., Tapper, D. and Folkman, J. Avascular and vascular phases of tumour growth in the chick embryo. *Br.J.Cancer* 35:347-356, 1977.
  28. Folkman, J., Watson, K., Ingber, D. and Hanahan, D. Induction of angiogenesis during transition from hyperplasia to neoplasia. *Nature* 339:58-61, 1989.
  29. Folkman, J. Angiogenesis and breast cancer. *J.Clin.Oncol.* 12 no.3:441-443, 1994.
  30. Guidi, A. J., Fischer, L., Harris, J. R. and Schnitt, S. J. Microvessel density and distribution in ductal carcinoma in situ of the breast. *J.Natl.Cancer Inst.* 86 no.8:614-619, 1994.
  31. Bose, S., Lesser, M. L., Norton, L. and Rosen, P. P. Immunophenotype of intraductal carcinoma. *Arch.Pathol.Lab.Med.* 120:81-85, 1996.
  32. Brem, S. S., Jensen, H. M. and Gullino, P. M. Angiogenesis as a marker of preneoplastic lesions of the human breast. *Cancer* 41:239-244, 1978.
  33. Chodak, G. W., Haudenschild, C., Gittes, R. F. and Folkman, J. Angiogenic activity as a marker of neoplastic and preneoplastic lesions of the human bladder. *Ann.Surg.* 192 no.6:762-771, 1980.
  34. Jensen, H. M., Chen, I., DeVault, M. R. and Lewis, A. E. Angiogenesis induced by "normal" human breast tissue: A probable marker for precancer. *Science* 218 no.15:293-295, 1982.
  35. Ziche, M. and Gullino, P. M. Angiogenesis and neoplastic progression in vitro. *J.Natl.Cancer Inst.* 69 no.2:483-487, 1982.
  36. Lawson, R. Implications of surface temperatures in the diagnosis of breast cancer. *Can.Med.Assoc.J.* 75:309-310, 1956.

37. Sterns, E. E., Curtis, A. C., Miller, S. and Hancock, J. R. Thermography in breast diagnosis. *Cancer* 50:323-325, 1982.
38. Revel, D., Brasch, R. C., Paajenen, H., Rosenau, W., Grodd, W., Engelstad, B., Fox, P. and Winkelhake, J. Gd-DTPA contrast enhancement and tissue differentiation in MRI of experimental breast carcinoma. *Radiology* 158:319-323, 1986.
39. Heywang, S. H., Wolf, A., Pruss, E., Hilbertz, T., Eiermann, W. and Permanetter, W. MRI of the breast with Gd-DTPA: Use and limitations. *Radiology* 171:95-103, 1989.
40. Burns, P. N., Halliwell, M., Wells, P. N. and Webb, A. J. Ultrasonic Doppler studies of the breast. *Ultrasound Med.Biol.* 8:127-143, 1982.
41. Nunes, L. W., Schnall, M. D., Orel, S. G., Hochman, M. G., Langlotz, C. P., Reynolds, C. A. and Torosian, M. H. Breast MR imaging: Interpretation model. *Radiology* 202:833-841, 1997.
42. Gilles, R., Guinebretiere, J. M. and Lucidarme, O. Nonpalpable breast tumours: Diagnosis with contrast-enhanced subtraction dynamic MR imaging. *Radiology* 191:625-631, 1994.
43. Weidner, N., Semple, J. P., Welch, W. R. and Folkman, J. Tumor angiogenesis and metastasis: Correlation in invasive breast carcinoma. *New Engl.J.Med.* 324 no.1:1-7, 1991.
44. Weidner, N., Folkman, J., Pozza, F., Beliacqua, P., Allred, E. N., Moore, D. H., Meli, A. and Gasparini, G. Tumour angiogenesis: A new significant and independent prognostic indicator in early-stage breast carcinoma. *J.Natl.Cancer Inst.* 84 no.24:1875-1887, 1992.
45. Bosari, S., Lee, A. K. C., DeLellis, R. A., Wiley, B. D., Heatley, G. J. and Silverman, M. L. Microvessel quantitation and prognosis in invasive breast carcinoma. *Hum.Pathol.* 23:755-761, 1992.
46. Gasparini, G. and Harris, A. L. Clinical importance of the determination of tumor angiogenesis in breast carcinoma: Much more than a new prognostic tool. *J.Clin.Oncol.* 13 no.3:765-782, 1995.
47. Fox, S. B., Leek, R. D., Smith, K., Hollyer, J., Greenall, M. and Harris, A. L. Tumor angiogenesis in node-negative breast carcinomas: Relationship with epidermal growth factor receptor, estrogen receptor, and survival. *Breast Cancer Res.Treat.* 29:109-116, 1994.
48. Visscher, D. W., Lawrence, W. D. and Boman, S. Angiogenesis in breast carcinoma -clinicopathologic relevance and potential use as a quantifiable surrogate endpoint biomarker. *J.Cell.Biochem.Suppl.* 19:146-152, 1994.
49. Guinebretiere, J. M., Le Monique, G., Gavaille, A., Bahi, J. and Weidner, N. Angiogenesis and risk of breast cancer in women with fibrocystic disease. *J.Natl.CancerInst.* 86 no.8:635-636, 1994.
50. Heywang, S. H., Hahn, D., Schmidt, H., Krischke, I., Eiermann, W., Bassermann, R. and Lissner, J. MRI of the breast using Gadolinium-DTPA. *J.Comput.Assist.Tomogr.* 10(2):199-204, 1986.
51. Kaiser, W. A. and Zeitler, E. MRI of the breast: fast imaging sequences with and without Gd-DTPA: preliminary observations. *Radiology* 170:681-686, 1989.
52. Pierce, W. B., Harms, S. E., Flamig, D. P., Griffey, R. H., Evans, W. P. and Hagans, J. E. Three-dimensional gadolinium-enhanced MRI of the breast: Pulse sequence with fat suppression and magnetization transfer contrast. *Radiology* 181:757-763, 1991.

53. Heywang-Kobrunner, S. H. Contrast-enhanced MRI of the breast. *Inv.Radiol.* 29(1):94-104, 1994.
54. Flickinger, F. W., Allison, J. D., Sherry, R. M. and Wright, J. C. Differentiation of benign from malignant breast masses by time-intensity evaluation of contrast enhanced MRI. *Magn.Reson.Imaging* 11:617-620, 1993.
55. Gribbestad, I. S., Neilson, G., Fjosne, H., Fougner, R., Haugen, O. A., Petersen, S. B., Rinck, P. A. and Kvinnsland, S. Contrast-enhanced magnetic resonance imaging of the breast. *Acta Oncol.* 31 no.8:833-842, 1992.
56. Stack, J. P., Redmond, O. M., Codd, M. B., Dervan, P. A. and Ennis, J. T. Breast disease: tissue characterization with Gd-DTPA enhancement profiles. *Radiology* 174:491-494, 1990.
57. Greenstein-Orel, S., Mendonca, M. H., Reynolds, C., Schnall, M. C., Solin, L. J. and Sullivan, D. C. MR imaging of ductal carcinoma in situ. *Radiology* 202:413-420, 1997.
58. Le Bihan, D., Breton, E., Lallemand, D., Grenier, P., Cabanis, E. A. and Laval-Jeantet, M. MR imaging of intravoxel incoherent motions: Application to diffusion and perfusion in neurologic disorders. *Radiology* 161:401-407, 1986.
59. Dent, D. M. and Cant, P. J. Fibroadenoma. *World J.Surg.* 13:706-710, 1989.
60. Chu, D. Z., Yamanashi, W. S., Frazer, J., Hazlewood, c. F., Gallager, H. S., Boddie, A. W. and Martin, R. G. Proton NMR of human breast tumors: correlation with prognostic parameters. *J. of Surg.Onc.* 36:1-4, 1987.
61. Graham, S. J., Bronskill, M. J., Byng, J. W., Yaffe, M. J. and Boyd, N. F. Quantitative correlation of breast tissue parameters using MR and X-ray mammography. *Br.J.Cancer* 73:162-168, 1996.

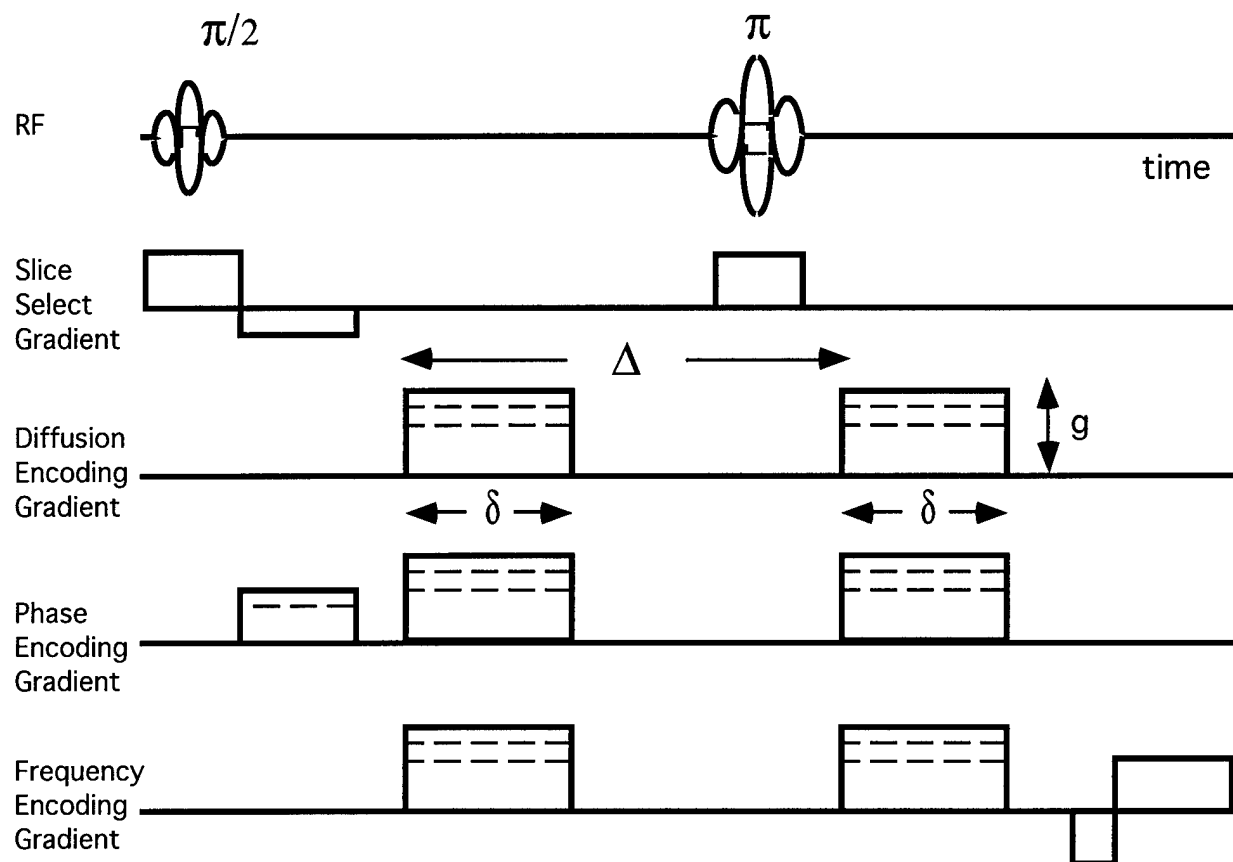


**Figure 1.** PGSE pulse sequence for diffusion/IVIM measurements with  $TE=75\text{ms}$ ,  $\delta=10\text{ms}$  and  $\Delta=50\text{ms}$ . b-factors for this TE range between 0 and  $485\text{ s/mm}^2$ .

## **Appendix 1: Comparison of Microvessel Distributions in Invasive Carcinomas and Fibroadenomas of the Breast** (Manuscript in Preparation)

Kirsten Weind, B.Sc., Cynthia F. Maier, M.Sc., Brian K. Rutt, Ph.D., Madeleine Moussa, M.D.

### **Introduction**

Breast disease affects millions of women worldwide. In North America, it has been estimated that one in nine women will develop mammary carcinoma [1]. Presently, the primary method of detection and diagnosis of breast disease is x-ray mammography which has a proven sensitivity of 85-95% [2,3]; however, specificity is substantially lower [4,5]. Additional diagnostic procedures must be carried out to determine whether a lesion is malignant or benign. Currently, 70-80% of mammographically indeterminate lesions progressing to surgical biopsy are found to be benign [5-8]. This false positive rate can be as high as 90% for women who have dense breast tissue and/or fibrocystic changes [8,9]. For this group of women, surgical biopsy has served only to provide a diagnosis since it is not necessary to remove a benign lesion unless it is causing pain.

The numerous biopsies that are being carried out solely for the purpose of diagnosis has led to the investigation of new imaging methods such as Magnetic Resonance Imaging (MRI), Positron Emission Tomography (PET) and Doppler Ultrasound (US) to serve as adjunctive non-invasive diagnostic procedures. These new medical imaging techniques rely on the principle that increased numbers of vessels and/or increased vascular permeability around malignancies resulting from tumour angiogenesis create characteristic, identifiable patterns that can be differentiated from those associated with benign lesions [10-13]. Unfortunately, specificity using these techniques has not been as high as was originally hoped. In particular, some fibroadenomas have been shown to mimic malignancies on these exams, and are often indistinguishable from solid carcinomas on mammography and in clinical presentation [14,15]. This is a particularly significant flaw for a potential adjunctive technique because, in a recent study, fibroadenomas accounted for between 30-50% of benign lesions removed by surgical biopsy [16].

Numerous histological studies have shown that there is a significant increase in the number of small, new blood vessels associated with highly invasive cancers [17-20]. It has also been found by several MRI groups that initial enhancement patterns following injection of a contrast agent correlated with microvessel density (Buadu, Frouge, Hulka). This seems to give quite convincing evidence in support of the basis of these diagnostic tests but the basic problem still exists: specificity is low and some benign lesions are still indistinguishable from malignancies. This has led some researchers to suggest that some fibroadenomas may actually be hyper-vascularized in a way previously thought to be characteristic for malignancies. Supporting this hypothesis is a recent study using ultrasound in which researchers detected elevated levels of blood flow in some fibroadenomas [21]. Unfortunately, we have found no histology-based studies evaluating vascularity in fibroadenomas, and very little data about blood flow in these lesions is actually available.

Recently, a handful of MR groups have seen a pattern of rim enhancement in a certain percentage of malignancies [22,23] and it is thought that this characteristic could aid in separating malignancies from benign lesions. The hypothesis is that outer edges of a malignant tumour should be particularly vascular since these are presumably the more actively growing areas and should therefore contain more numerous vessels. Although this seems promising, we have found no study to date which has quantitatively compared the vascular distribution within invasive carcinomas to that found at their invading boundaries.

In order to utilize imaging modalities such as MRI, PET and/or US as adjunctive imaging techniques effectively, we must first evaluate the vascular patterns of both malignant and benign lesions of the breast histologically in an attempt to find a difference prominent enough to identify and separate the various classes of lesions. In addition, the study of the differences and/or similarities between vascular distributions in malignant and benign breast lesions could serve to illuminate the unique mechanisms contributing to the formation of a microcirculatory network in a malignant tumour, and its subsequent role in tumour metastasis. With these objectives in mind, we have evaluated spatial patterns of vessel distribution and vascular density at the boundary and within invasive carcinomas and fibroadenomas.

### Materials and Methods

Routinely processed, formalin-fixed, paraffin-embedded tissue from 39 lumpectomies (19 invasive carcinomas and 20 fibroadenomas) was retrieved from the files of the Department of Pathology at London Health Sciences Centre, London, Ontario, Canada. Immuno-histochemical studies for factor VIII-related antigen (rabbit polyclonal antibody; Dimension Labs, Mississauga, ON; 1:100 dilution) were performed on 4 mm-thick recut sections using the avidin-biotin peroxidase technique. All tissues were counter stained with haematoxylin.

Microvessels were counted using light microscopy on x200 fields (x20 objective lens, x10 ocular lens) by one of the investigators (MM). 10 fields were chosen at random in both the central and peripheral regions of each tumour (provided there was sufficient tissue). The tumour periphery was defined as a field inside the tumour boundary (defined as the leading edge of invading cells in the case of invasive carcinomas), with the microscope field circumference touching the boundary. The tumour centre was defined as a microscope field inside the tumour at least 1 field diameter away from the boundary. Within the centre of the tumour, fields were not defined in sclerosed, avascular regions of the carcinomas. Vessel identification was carried out according to the criteria used by Weidner et al [17]. Any brown-staining, free-standing endothelial cell or group of endothelial cells was counted as a vessel. Vessels larger than 40µm in diameter were not included in our study; the group of microvessels studied contained only capillaries and smaller arterioles and venules (presumed to result from tumour angiogenesis [24]).

## Results

<b>A) Invasive Carcinomas</b>										
<b>Case Number</b>	<b>Patient Age (years)</b>	<b>Tumor Diameter (cm)</b>	<b>Tumor Grade</b>	<b>Lymph Node Status</b>		<b>Mean Vessel Count (per field <math>\pm</math> SD)</b>	<b>Vessel Count Range (per field)</b>	<b>Ratio of Means Periphery/Center</b>	<b>P value</b>	<b>Power of the test (1 - <math>\beta</math>)</b>
1	44	1.5	2	negative	periphery center	13 $\pm$ 2.2 8.0 $\pm$ 2.2	9 to 16 5 to 12	1.63	<0.0001*	0.9989
2	66	0.7	2	negative	periphery center	20.8 $\pm$ 4.4 11.4 $\pm$ 2.1	16 to 26 9 to 14	1.82	0.0013*	0.9786
3	74	2	1	not known	periphery center	25.1 $\pm$ 6.8 17.3 $\pm$ 3.7	17 to 38 13 to 23	1.45	0.0042*	0.8542
4	47	1.7	2	positive	periphery center	32.0 $\pm$ 10.5 15.6 $\pm$ 5.5	20 to 53 8 to 25	2.05	0.0004*	0.9882
5	75	3	2	not known	periphery center	19.8 $\pm$ 3.2 10.8 $\pm$ 2.4	16 to 24 7 to 15	1.83	0.0002*	0.9992
6	70	2.5	3	positive	periphery center	19.8 $\pm$ 2.4 7.7 $\pm$ 1.8	16 to 22 5 to 10	2.57	<0.0001*	1.0000
7	54	2.5	2	positive	periphery center	24.5 $\pm$ 4.4 10.8 $\pm$ 4.7	17 to 30 4 to 17	2.27	<0.0001*	0.9998
8	55	1.5	2	negative	periphery center	29.1 $\pm$ 10.3 28.8 $\pm$ 4.3	14 to 49 23 to 35	1.01	0.9297	0.05
9	49	2.2	3	positive	periphery center	29.0 $\pm$ 3.3 21.1 $\pm$ 7.0	25 to 32 14 to 32	1.37	0.0439*	0.4595
10	30	1.8	3	positive	periphery center	71 $\pm$ 18.1 33.9 $\pm$ 10.8	54 to 105 24 to 57	2.09	<0.0001*	0.9998
11	80	2.5	3	not known	periphery center	30.2 $\pm$ 6.6 16.6 $\pm$ 3.2	22 to 43 13 to 23	1.82	<0.0001*	0.9999
12	31	2	3	positive	periphery center	23.4 $\pm$ 4.6 18.0 $\pm$ 4.9	16 to 30 10 to 27	1.30	0.0205*	0.5972
13	52	1.3	2	negative	periphery center	35.4 $\pm$ 13.0 17.2 $\pm$ 3.9	17 to 55 9 to 22	2.06	0.0005*	0.9822
14	57	1	1	negative	periphery center	21.6 $\pm$ 5.6 22.8 $\pm$ 4.3	16 to 31 18 to 29	0.95	0.615	0.05
15	79	2	1	not known	periphery center	41.6 $\pm$ 7.5 35.6 $\pm$ 9.5	28 to 54 24 to 51	1.17	0.135	0.1953
16	46	5	2	positive	periphery center	23.6 $\pm$ 3.0 19.7 $\pm$ 2.6	17 to 27 16 to 24	1.20	0.0059*	0.8109
17	49	2.5	2	negative	periphery center	30.1 $\pm$ 7.6 18.2 $\pm$ 3.3	20 to 45 13 to 22	1.65	0.0003*	0.992
18	47	1.5	1	negative	periphery center	52.5 $\pm$ 14.9 42.5 $\pm$ 6.3	39 to 88 36 to 57	1.24	0.0667	0.3412
19	61	0.4	2	not known	periphery center	55.1 $\pm$ 12.8 25.9 $\pm$ 6.4	35 to 72 18-40	2.13	<0.0001*	1.0000



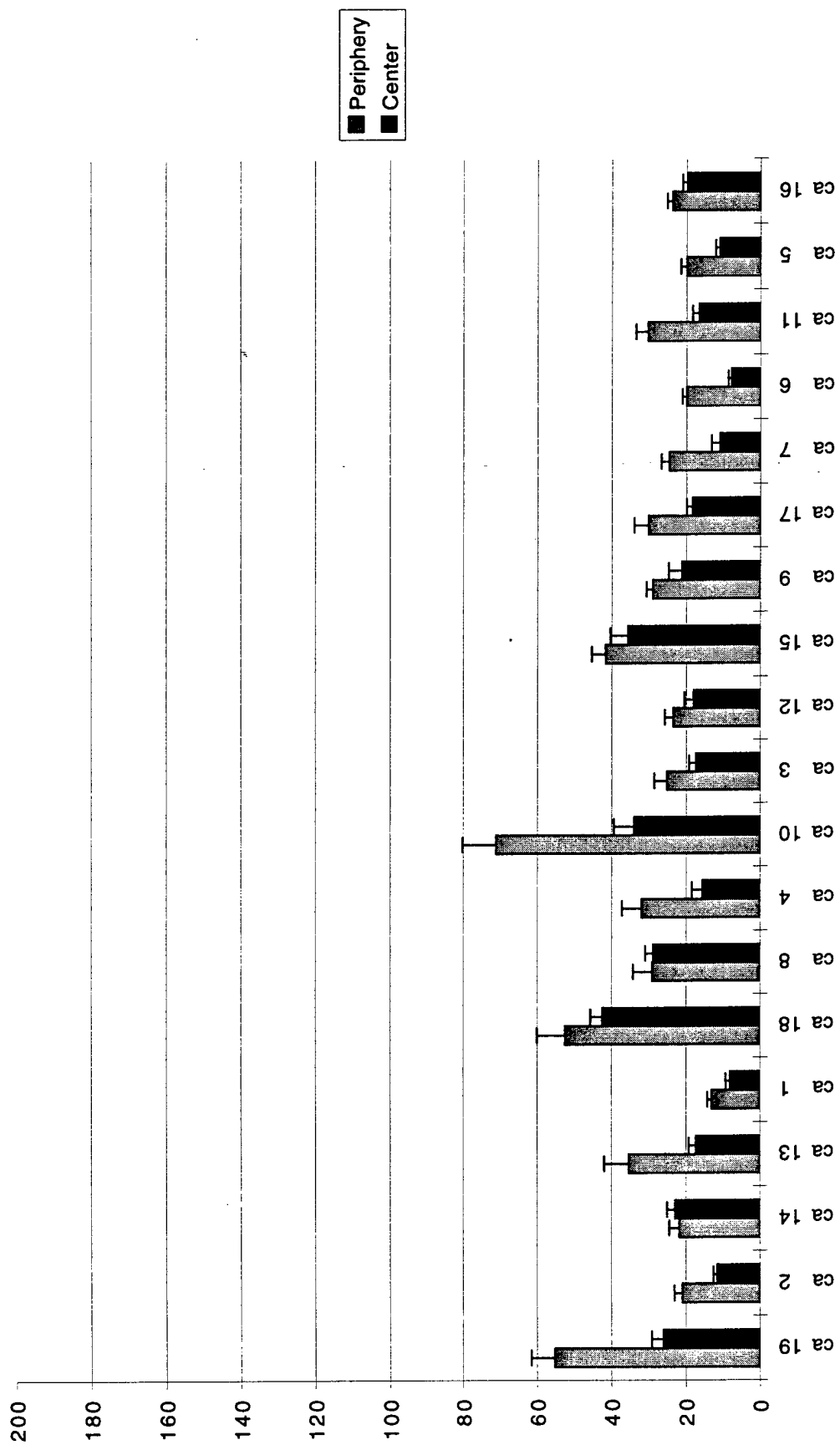
**B) Fibroadenomas**

Case Number	Patient Age (years)	Tumor Diameter (cm)	Tumor Classification		Mean Vessel Count ( $\pm$ SD)	Vessel Count Range (per field)	Ratio of Means Periphery/Center	P value	Power of the test (1 - $\beta$ )
1	41	1	Fibromyxoid	periphery center normal	34.9 $\pm$ 13.2 25.3 $\pm$ 5.68 43.6 $\pm$ 9.02	57 to 15 35 to 17 55 to 32	1.42	0.0491*	0.4086
2	47	1.4	Fibromyxoid	periphery center normal	33.1 $\pm$ 7.34 36.7 $\pm$ 10 79.6 $\pm$ 16.5	44 to 24 58 to 19 92 to 54	0.9	0.3719	0.05
3	43	1	Cellular	periphery center normal	112 $\pm$ 29.8 95.6 $\pm$ 24.4 133 $\pm$ 58.2	157 to 54 137 to 76 200 to 74	1.17	0.3004*	0.0635
4	19	3.5	Cellular	periphery center normal	35.2 $\pm$ 11.9 17 $\pm$ 4.81 55 $\pm$ 6.82	57 to 20 25 to 7 60 to 43	2.07	0.0003*	0.9909
5	44	1		periphery center normal	48.5 $\pm$ 13 53.4 $\pm$ 10.4 75.6 $\pm$ 13.3	68 to 29 67 to 40 96 to 60	0.91	0.3651*	0.05
6	27	0.6	Fibrosed	periphery center normal	47.9 $\pm$ 9.75 40.8 $\pm$ 5.26 46.8 $\pm$ 5.93	65 to 31 46 to 32 52 to 37	1.17	0.1565	0.1708
7	38	0.6	Myxoid	periphery center center	51.7 $\pm$ 9.04 68 $\pm$ 19.8 98.2 $\pm$ 32.1	70 to 41 82 to 54 151 to 65	0.76	0.0757	0.3292
8	43	2	Cellular	periphery center normal	39.3 $\pm$ 13.1 45.7 $\pm$ 12.6 110 $\pm$ 26.2	60 to 20 71 to 25 144 to 85	0.86	0.2972	0.0632
9	31	1.5	Sclerosed	periphery center normal	39.1 $\pm$ 7.23 27.3 $\pm$ 8.96 75.7 $\pm$ 16.6	47 to 26 39 to 14 89 to 57	1.43	0.0045*	0.8443
10	39	2.5	Mixed	periphery center normal	29.1 $\pm$ 11 18 $\pm$ 6.02 39.6 $\pm$ 8.85	50 to 15 27 to 7 51 to 28	1.62	0.0117*	0.7032
11	49	1	Cellular	periphery center normal	40.4 $\pm$ 11 24 $\pm$ 9.9 99.2 $\pm$ 58.5	58 to 27 31 to 17 167 to 39	1.68		
12	22	2.7	Mixed	periphery center normal	24.7 $\pm$ 6.93 15 $\pm$ 0 53.2 $\pm$ 37.2	34 to 14 15 to 15 113 to 21	1.64		
13	34	1.7	Sclerosed	periphery center normal	30.7 $\pm$ 15.8 34.4 $\pm$ 12.3 59.2 $\pm$ 12	59 to 14 51 to 11 71 to 45	0.89	0.5651*	0.05
14	35	2	Fibromyxoid	periphery center normal	37.4 $\pm$ 8.28 30.6 $\pm$ 14.1 0	50 to 22 58 to 15 0	1.22	0.2043	0.1208
15	21	1.1		periphery center normal	64.9 $\pm$ 12 64.6 $\pm$ 12.2 0	78 to 47 88 to 46 0	1	0.9512	0.05

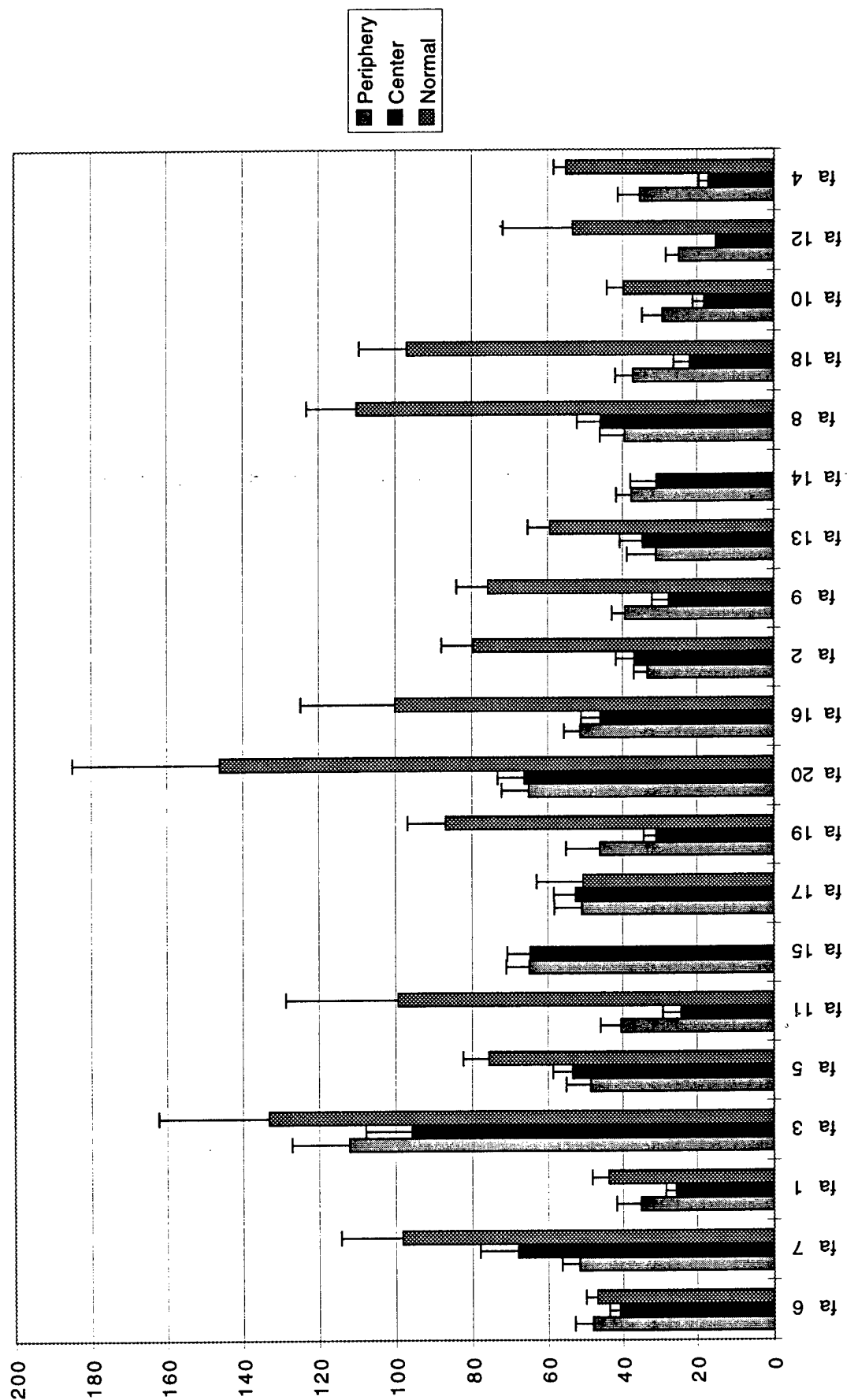
**B) Fibroadenomas**

Case Number	Patient Age (years)	Tumor Diameter (cm)	Tumor Classification		Mean Vessel Count ( $\pm$ SD)	Vessel Count Range (per field)	Ratio of Means Periphery/Center	P value	Power of the test (1 - $\beta$ )
16	27	1.4	Myxoid	periphery center normal	51.2 $\pm$ 8.89 45.8 $\pm$ 10.4 100 $\pm$ 49.2	65 to 41 63 to 29 152 to 54	1.12	0.2294	0.1019
17	37	1.2	Fibromyxoid	periphery center normal	50.8 $\pm$ 14.9 52.6 $\pm$ 11.5 50.5 $\pm$ 24.8	77 to 33 71 to 34 68 to 33	0.97	0.7954	0.05
18	20	2.5	Myxoid	periphery center normal	37 $\pm$ 9.57 21.8 $\pm$ 8.47 96.8 $\pm$ 25	55 to 23 40 to 11 130 to 66	1.7	0.0014*	0.943
19	37	1.2		periphery center normal	46 $\pm$ 18 30.8 $\pm$ 6.58 86.8 $\pm$ 19.8	75 to 23 38 to 19 38 to 19	1.49	0.0217*	0.5853
20	47	1.2		periphery center normal	65 $\pm$ 14.4 66.2 $\pm$ 13.9 146 $\pm$ 77.9	90 to 48 81 to 48 229 to 66	0.98	0.8799	0.05

# Invasive Carcinoma Mean Count



Fibroadenoma Mean Count



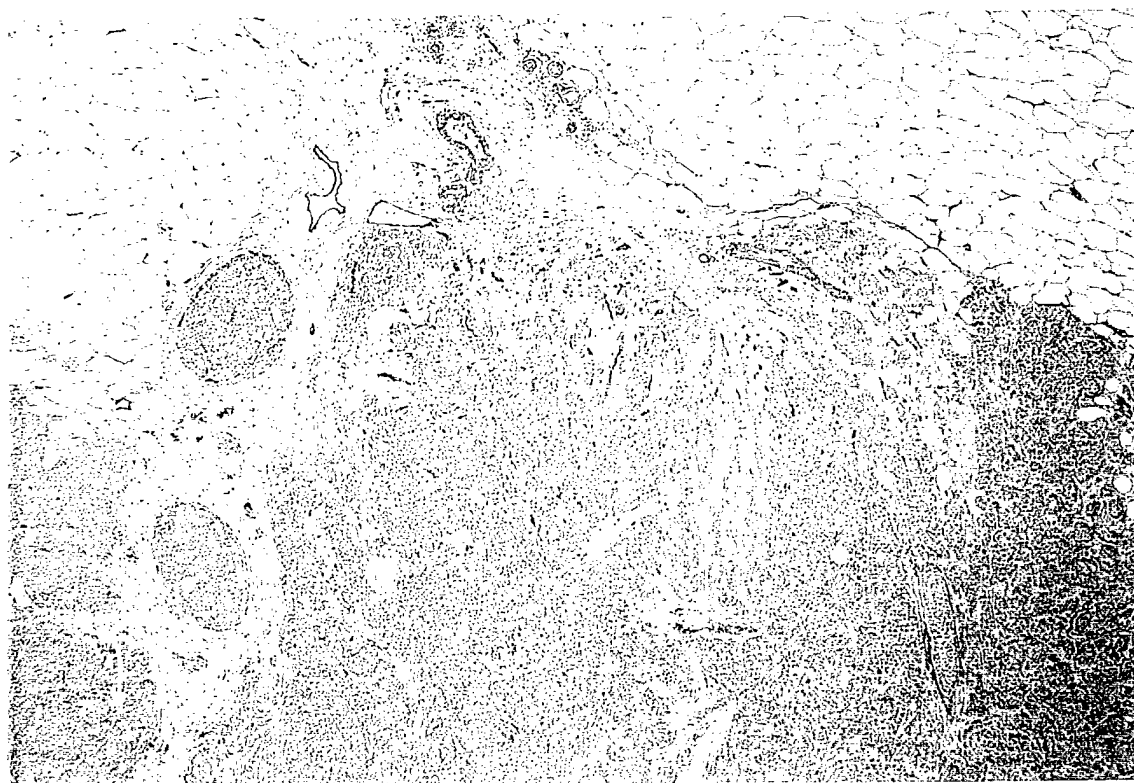


**Figure 1:** Periphery of invasive carcinoma at low magnification (x80), Factor VIII stain, showing higher microvessel density compared to center

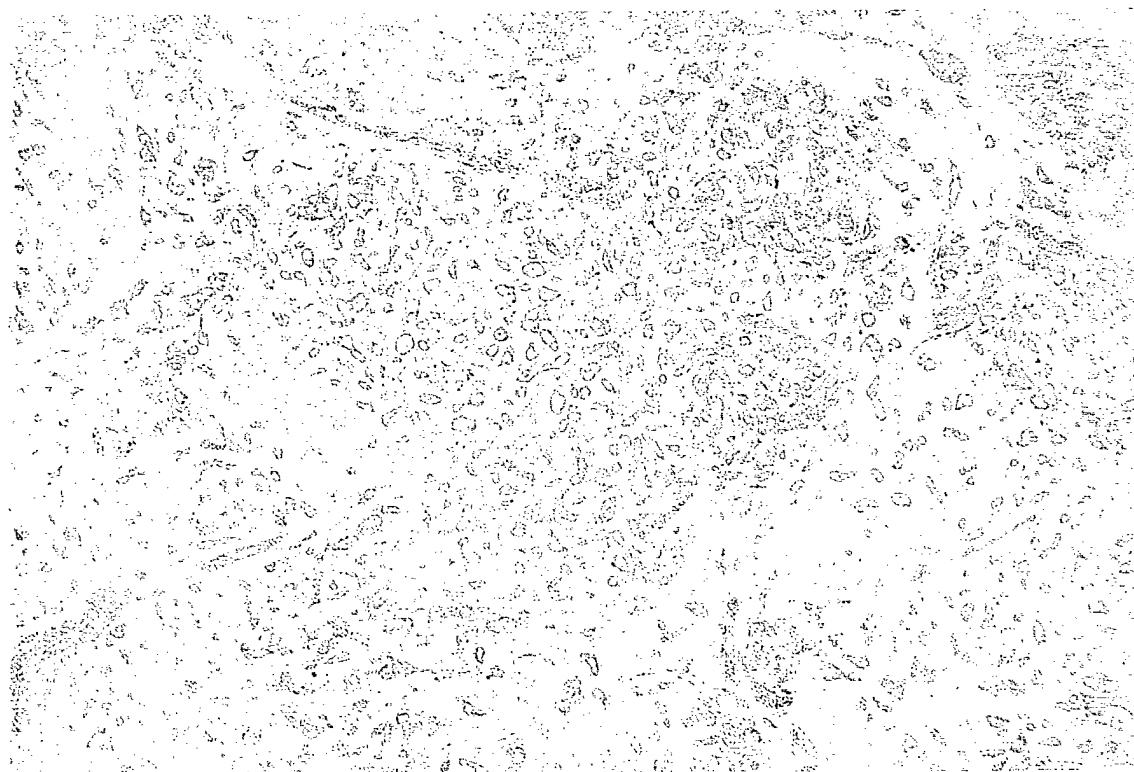


**Figure 2:** Center of invasive carcinoma at low magnification (x80), Factor VIII stain, showing lower microvessel density compared to periphery

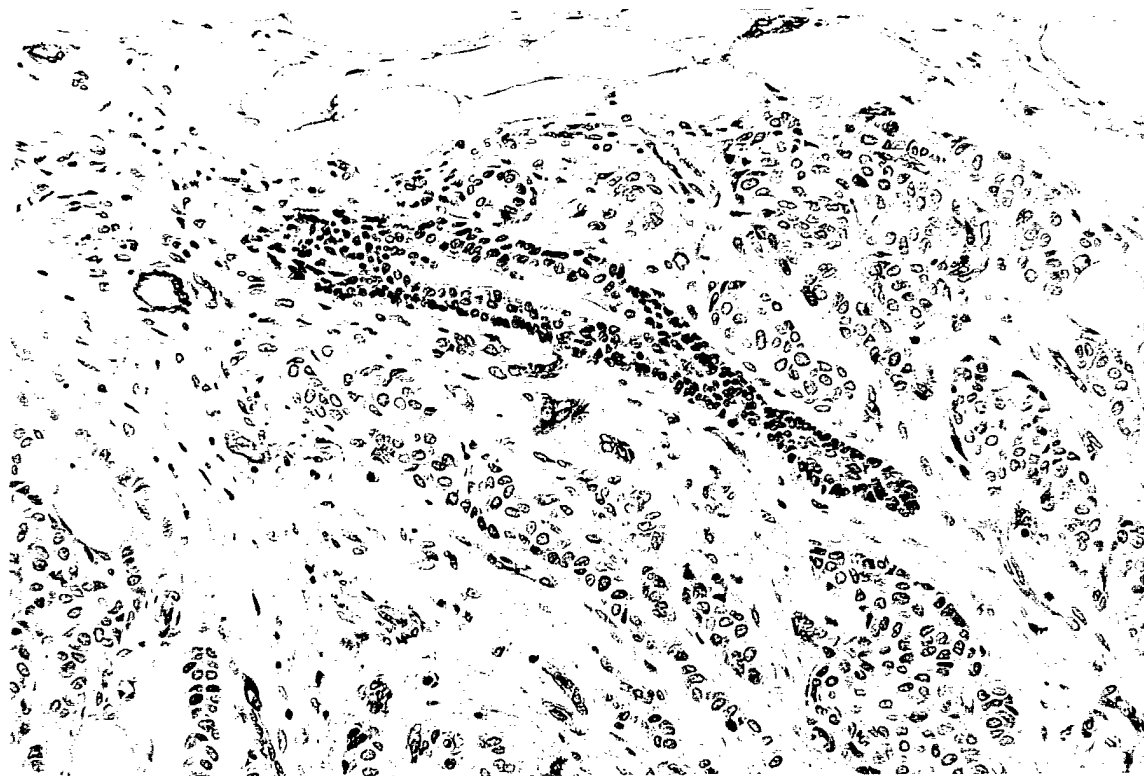


**Figure 3:** Periphery of invasive carcinoma at high magnification (x400), Factor VIII stain, showing higher microvessel density compared to center

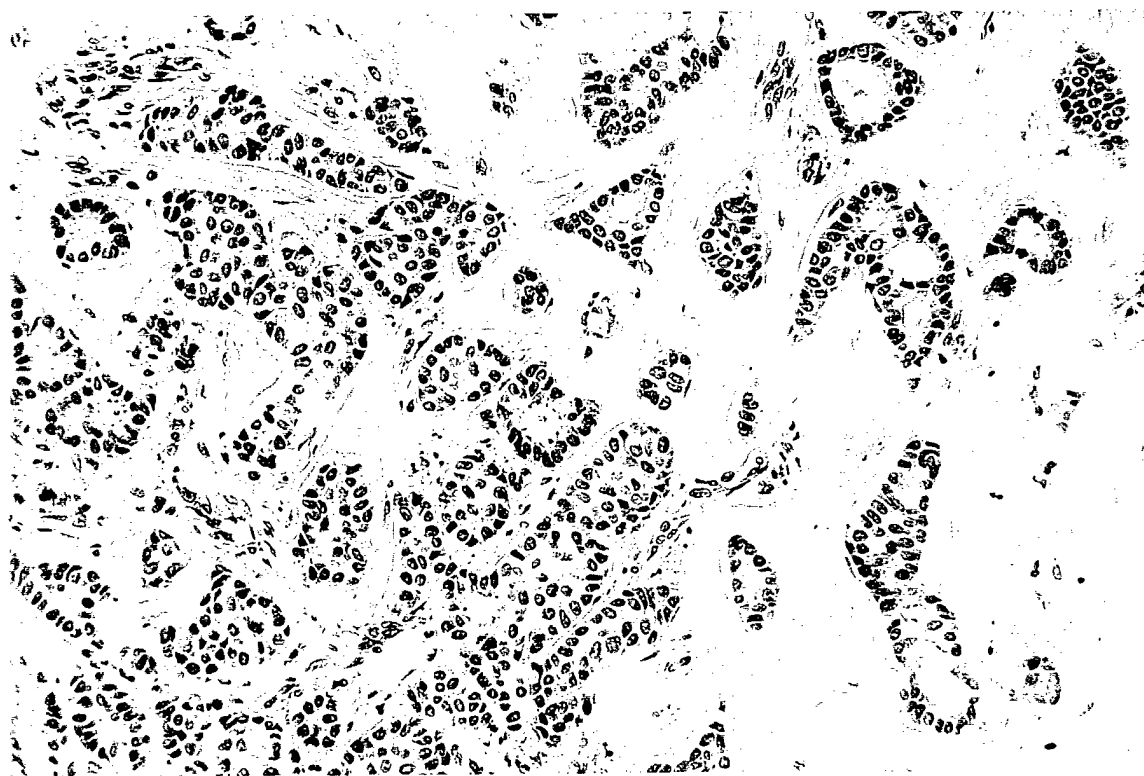


**Figure 4:** Center of invasive carcinoma at high magnification (x400), Factor VIII stain, showing lower microvessel density compared to periphery

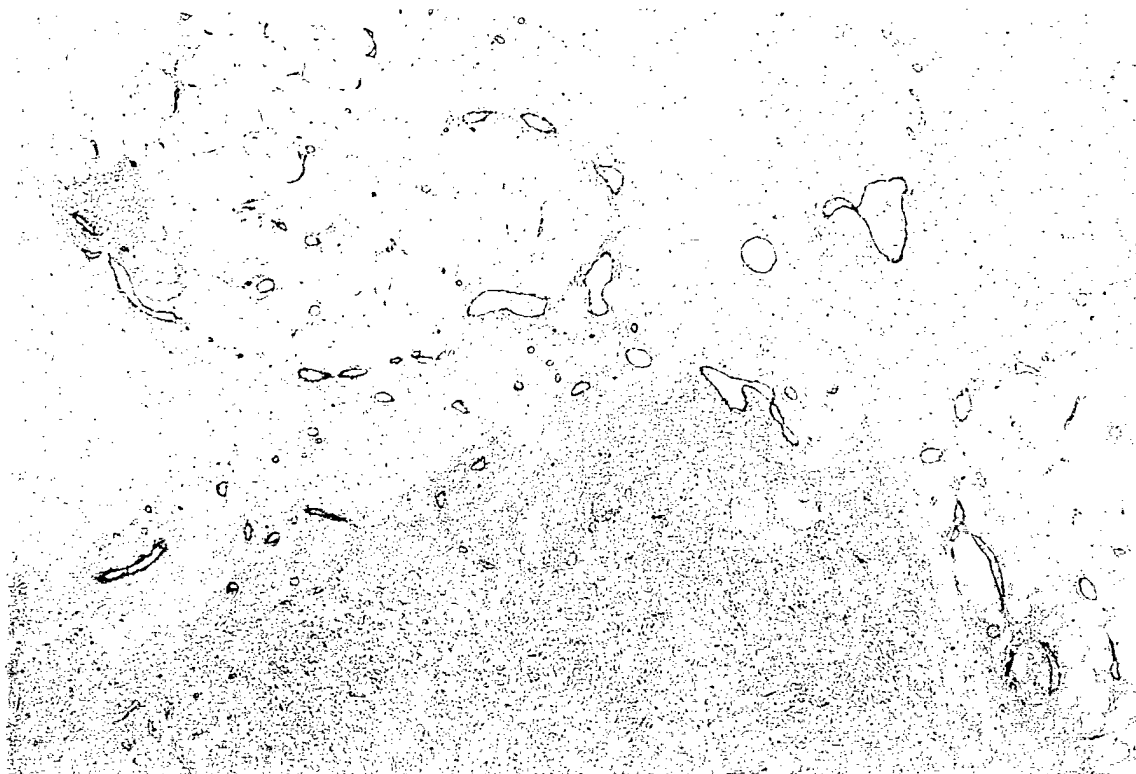


**Figure 5:** Leading edge of invasive carcinoma, showing high number of large ( $>40\mu\text{m}$ ) vessels just outside periphery

## Discussion

Our results support the hypothesis that in general, microvessel density is higher in the active tumor periphery of invasive carcinomas compared to the tumour centre. While most central fields within the carcinomas were characterized by desmoplasia and low vessel counts, some central cellular areas existed and were associated with higher vessel counts. On the other hand, microvessel counts in the fibroadenoma were more uniformly distributed throughout the lesion.

In 6 of the 19 cases, high numbers of larger vessels ( $>40\mu\text{m}$  in diameter) were present just outside the leading edge of the tumour. These larger vessels were not included in our study, but were easily observed on low magnification. In two additional cases, larger vessels were observed immediately inside the tumour boundary. Further evaluation of these larger vessels may prove important for the development of adjunctive imaging techniques for breast cancer diagnosis.

## References

1. National Cancer Institute of Canada: Canadian Cancer Statistics 1997, Toronto:1997.
2. Schmitt, E. L. and Threatt, B. Characteristics of breast cancer in an incident cancer population. *Am.J.Roentgenol.* 143:402-406, 1984.
3. Xenophon, L. Imaging techniques for breast disease. *Clin.Obstet.Gynaecol.* 37 no.4:933-943, 1994.
4. Verbeek, A. L., Hendriks, J. H., Holland, R., Mravunac, M., Sturmans, F. and Day, N. E. Reduction of breast cancer mortality through mass screening with modern mammography: First results of the Nijmegen project, 1975-1981. *Lancet* 1(1):1222-1224, 1984.
5. Baker, L. H. Breast cancer detection demonstration project: Five-year summary report. *CA - A Cancer Journal for Clinicians* 32:194-225, 1982.
6. Williams, S. M., Kaplan, P. A., Petersen, J. C. and Lieberman, R. P. Mammography in women under age 30: Is there clinical benefit? *Radiology* 161:49-51, 1986.
7. Ciatto, S., Cataliotti, L. and Distante, V. Nonpalpable lesions detected with mammography: Review of 512 consecutive cases. *Radiology* 165:99-102, 1987.
8. Dershaw, D. D., Shank, B. and Reisinger, S. Mammographic findings after breast cancer treatment with local excision and definitive irradiation. *Radiology* 164:455-461, 1987.
9. Harris, V. J. and Jackson, V. P. Indications for breast imaging in women under age 35 years. *Radiology* 172:445-448, 1989.
10. Lawson, R. Implications of surface temperatures in the diagnosis of breast cancer. *Can.Med.Assoc.J.* 75:309-310, 1956.
11. Sterns, E. E., Curtis, A. C., Miller, S. and Hancock, J. R. Thermography in breast diagnosis. *Cancer* 50:323-325, 1982.
12. Heywang, S. H., Wolf, A., Pruss, E., Hilbertz, T., Eiermann, W. and Permanetter, W. MRI of the breast with Gd-DTPA: Use and limitations. *Radiology* 171:95-103, 1989.
13. Burns, P. N., Halliwell, M., Wells, P. N. and Webb, A. J. Ultrasonic Doppler studies of the breast. *Ultrasound Med.Biol.* 8:127-143, 1982.



14. Brinck, U., Fischer, U., Korabiowska, M., Jutrowski, M., Schauer, A. and Grabbe, E. The variability of fibroadenoma in contrast-enhanced dynamic MR mammography. *AJR* 168:1331-1334, 1997.
15. Knopp, M. V., Sinn, P., Junkermann, H. J., Dikic, S., Hawighorst, H., Himmelhan, N., Brix, G. and van Kaick, G. Fibroadenomas in MR mammography -Is there a correlation between enhancement pattern and histology? *Proc SMR and ESMRMB* 3:1604, 1995.
16. Dent, D. M. and Cant, P. J. Fibroadenoma. *World J.Surg.* 13:706-710, 1989.
17. Weidner, N., Folkman, J., Pozza, F., Beliacqua, P., Allred, E. N., Moore, D. H., Meli, A. and Gasparini, G. Tumour angiogenesis: A new significant and independent prognostic indicator in early-stage breast carcinoma. *J.Natl.Cancer Inst.* 84 no.24:1875-1887, 1992.
18. Visscher, D. W., Lawrence, W. D. and Bowman, S. Angiogenesis in Breast Carcinoma -Clinicopathologic relevance and potential use as a quantifiable surrogate endpoint biomarker. *Journal of Cellular Biochemistry, Supplement* 19:146-152, 1994.
19. Fox, S. B., Leek, R. D., Smith, K., Hollyer, J., Greenall, M. and Harris, A. L. Tumor angiogenesis in node-negative breast carcinomas: Relationship with epidermal growth factor receptor, estrogen receptor, and survival. *Breast Cancer Res.Treat.* 29:109-116, 1994.
20. Weidner, N. Tumor angiogenesis: Review of current applications in tumor prognostication. *Sem.Diag.Path.* 10 no.4:302-313, 1993.
21. Holcombe, C., Pugh, N., Lyons, K., Douglas-Jones, A., Mansel, R. E. and Horgan, K. Blood flow in breast cancer and fibroadenoma estimated by colour doppler ultrasonography. *British Journal of Surgery* 82:787-788, 1995.
22. Nunes, L. W., Schnall, M. D., Orel, S. G., Hochman, M. G., Langlotz, C. P., Reynolds, C. A. and Torosian, M. H. Breast MR imaging: Interpretation model. *Radiology* 202:833-841, 1997.
23. Orel, S. G., Schnall, M. D., LiVolsi, V. A. and Troupin, R. H. Suspicious breast lesions: MRI with radiologic-pathologic correlation. *Radiology* 190:485-493, 1994.
24. Less, J. R., Skalak, T. C., Sevic, E. M. and Jain, R. K. Microvascular architecture in a mammary carcinoma: Branching patterns and vessel dimensions. *Research* 51:263-273, 1991.

## Appendix 2

**Practical Design of a High-Strength Gradient Coil for  
Diffusion/Microvascular Imaging of Breast Tumours**

Cynthia F. Maier, Hristo N. Nikolov, Kenneth C. Chu, Blaine A. Chronik, Brian K. Rutt

*Departments of Medical Biophysics and Diagnostic Radiology,  
University of Western Ontario  
London, Ontario, Canada*

*and*

*Tom Lawson Family Imaging Research Laboratories,  
John P. Robarts Research Institute  
London, Ontario, Canada N6A 5K8*

Correspondence to:

B. K. Rutt, Ph.D.,  
Department of Diagnostic Radiology,  
University Hospital,  
London, Ontario  
CANADA N6A 5A5

Tel: (519) 663-3000  
Fax: (519) 663-3789

Short Running Head: Breast Gradient Coils

Revised manuscript prepared for Magnetic Resonance in Medicine  
Date: June 8, 1997

## INTRODUCTION

In this paper, we present a specialized gradient coil design for breast imaging and demonstrate the utility of this coil for performing MR diffusion imaging with short duration, high-strength gradient pulses. Sensitization of an MR pulse sequence to motion can be achieved using conventionally available gradient hardware; however, measurement of water diffusion or slow flow in microvessels with this hardware requires long echo times to achieve large gradient moments, therefore suffers from significant signal loss due to T2 relaxation and system non-idealities. Additionally, increasing the time between motion-sensitizing gradient pulses allows more macroscopic motion to occur in this interval, resulting in pixel misregistration, motion-induced ghost artifacts and diffusion/flow measurement artifacts. Higher strength gradients would allow adequate sensitization to small motions (i.e. large gradient moments) with very short, high-amplitude gradient pulses and minimal time delay between these pulses. Diffusion and high-velocity-resolution flow imaging can therefore best be accomplished with specialized hardware to generate these high-strength gradients.

## METHODS

The gradient coil assembly was designed in a cylindrical geometry, with each gradient coil built onto a separate cylindrical former. The three-axis coil set was comprised of concentrically nested coils, oriented vertically such that their common axis was transverse to the main field as shown in Figure 1. Space restrictions within the magnet bore required that the coils be as short as possible in the vertical direction to allow a patient to lie comfortably above the top edge of the cylinders. Unfortunately, decreasing the height of the coils (relative to their diameters) makes the creation of uniform gradients within the coils much more difficult. To satisfy the competing demands of good gradient uniformity and size restrictions, we used an aspect ratio of approximately 1:1 for our cylindrical coils. The height of the complete coil assembly was 16 cm (leaving 34 cm clearance in the vertical direction in our GE Signa Horizon scanner), where the largest coil diameter was 21.6 cm.

To generate the winding densities required for high gradient strengths, relatively small diameter wire (AWG#20) was used to construct the coils. The resistivity of this wire is high, requiring an active cooling system to remove heat and maintain temperatures inside the coils within a range comfortable for the patient. Water-cooling jackets with very thin walls were sandwiched between the gradient coils, so that resistive heat could be removed efficiently while maintaining the compact construction of the coil assembly. A dedicated RF coil and shield were mounted inside the innermost gradient coil with approximately 1.3 cm space between the RF coil and closest gradient coil. The entire assembly is depicted in cross-section in Figure 2.

### Electrical Design

The highly efficient quadrupolar current distribution (1-3) was used to provide gradients in  $B_z$  along both the x- and z- directions ( $G_x$  and  $G_z$ ). This current density varies azimuthally as  $\cos(2\theta)$  and is entirely directed along the axial direction on the surface of the cylindrical former. Discrete wire positions approximating the continuous quadrupolar current density were calculated by sampling the current density  $\cos(2\theta)$  at  $\theta_i$  such that  $\cos(2\theta_{i+1}) - \cos(2\theta_i)$  was constant. A schematic diagram showing this ideal wire distribution is given in Figure 3(a). The current pattern in Figure 3(a) is non-physical in that the current is discontinuous at the ends of the coil, and therefore, connecting paths between the wires ("return wires") must be provided. In most imaging applications where local gradient coils have been used previously, the volume to be imaged has been located at the center of the coil, and placing return paths near the ends of the cylinder had a minimal effect on the desired field within the object. For breast imaging applications, the required location for the region of good gradient uniformity is near the top edge of the coils and a

conventional return wire arrangement would corrupt the gradient field uniformity within this volume. We chose to place the return wire components instead on horizontal plates at the tops and bottoms of the coils. Close to the cylinders on the plates, the return paths were extended along the  $z$ -direction for at least five centimeters (no  $B_z$  is generated by current in the  $z$ -direction). The bottom set of return wires for the  $G_z$  coil were strung across the bottom of the cylinder in the  $z$  direction. The quadrupole current distribution for  $G_x$  is rotated  $45^\circ$  with respect to  $G_z$ , and the return wires for  $G_x$  could not be strung in the  $z$ -direction; therefore, these wires were located on a horizontal plate.

The design of the  $G_y$  gradient makes use of the fact that  $\nabla \times \mathbf{B} = 0$  throughout any region in which the current density is zero. This means that a transverse gradient coil with its axis along  $z$  (the conventional orientation) can be turned  $90^\circ$  about the  $x$ -axis so that its axis is now along the  $y$  direction, and used to produce a gradient in  $B_z$  along the  $y$  direction. We designed a transverse gradient coil in the conventional orientation using the target field method (4-5), and then rotated the coil to produce  $G_y$ . Although a wide range of breast sizes exists, we defined an average Volume of Interest (VOI) for breast imaging (by comparison with commercially available breast RF coils) as a cylindrical volume with length equal to 60% of the coil height (11.5cm), a diameter equal to 90% of the RF coil diameter (13.5cm) and located flush with the top surface of the gradient coil assembly. The target field coil was designed to have its region of good gradient uniformity centered on this VOI. This design consisted of only two sets of closed current loops (Figure 3(b)). For the target-field coil in its conventional orientation with its axis along  $z$ , the desired gradient is created almost entirely by the current in half of the wire loops only (the "primary" component of the loop as indicated in Figure 3(b)), and return wires are an intrinsic part of the design (labelled "return" in Figure 3(b)). For this coil, only one set of "return paths" is required for current continuity, and in the vertical orientation, these wires are located at the bottom of the cylinder. In our coil design, such a large number of loops was required to generate the desired gradient efficiency that these return wires would have occupied a large fraction of the space available on the surface of the cylinder. Due to the strict limitations on coil height, we felt that this space could be more efficiently used if only the primary component of the coil design was present on the cylinder itself, and the return paths located on a horizontal plate as for the quadrupole coils. A complication that arises from truncating the wire pattern in the vertical dimension in this way is that the reciprocity relations from Maxwell's equations no longer hold for a non-physical current distribution (i.e.  $\nabla \times \mathbf{B} \neq 0$  for a current distribution with non-zero divergence). This means that the gradient field calculated for the truncated design is not identical in the conventional and transverse orientations unless the return wires are included in the calculation. We shall see in the Results section that the truncated coil in the transverse orientation has both an increased gradient efficiency compared to the full design for the same coil height, and additionally, the region of acceptable gradient uniformity (<20% deviation from uniformity) is significantly larger for the truncated coil. A schematic of the 3-coil gradient assembly with horizontal return wire plates is shown in Figure 4.

One undesirable side-effect that arises from locating the return wires on horizontal surfaces is that the torque on the coils from interaction with the main static field is greatly increased. This effect is significant. For our 1.5T magnet, current is only supplied when the coils are positioned near the central, highly homogeneous region of the magnet (typical clinical imaging systems have a 50 cm diameter spherical volume of better than 10 ppm  $B_0$  uniformity), and the upward (downward) force on the  $+z$  ( $-z$ ) half of the horizontal plate for the  $G_z$  coil is approximately 15 N/A (3.5 lb/A) increasing linearly with applied current. As the gradients are switched, the effect of this force is to create an alternating torque of approximate size 3 Nm/A. For many pulse sequences, the direction of the current is switched rapidly, resulting in a torque that alternates direction rapidly, and causes significant vibrational stress on the coils. For our preliminary experiments, a temporary coil support was constructed from wood and glass-reinforced phenolic. The horizontal plates were rigidly attached to the support, and the support structure itself served to

mount the coil assembly inside the bore of the imager, thereby preventing any bulk coil motions that could arise from the magnetic forces on the wires. The wires themselves were potted securely in the milled grooves using epoxy and were prevented from vibrating loose from these grooves by the next adjacent layer of cooling channels, since all layers were tightly sandwiched together.

### Coil Construction

To produce high gradient efficiencies, it is advantageous to use the maximum number of wires possible. This number is constrained in an obvious way by the wire diameter, minimum spacing between wires, and circumference of the cylindrical former. To obtain the desired gradient efficiencies for these coils, it was necessary to use relatively small wires (AWG#20) having a diameter of  $\sim 1$  mm and an interwire spacing of 0.5 mm. The Gx (outermost) coil was wound with a single length of wire such that 216 axially directed segments generated the required current density, and for the innermost coil (Gz), 200 axially directed segments were wound. For the middle coil (Gy), constraining the closest separation of the wires to be 0.5 mm allowed 48 loops per side. For all three coils, the wire paths were milled (numerically controlled) into the surface of polycarbonate/acrylic formers. Wire was then wound into these grooves and epoxied in place. Figure 5(a) shows the constructed Gx coil complete with horizontal plates after winding with (dielectric) insulated copper wire. The upper plates were curved downward at the superior and inferior ends to provide a more comfortable structure for patient support. Figure 5(b) shows the middle coil (Gy) prior to assembly of the complete gradient coil unit.

The resistivity of the small diameter wire used to construct the coils is relatively high, increasing from  $33.3 \text{ m}\Omega/\text{m}$  at room temperature to  $40.5 \text{ m}\Omega/\text{m}$  at  $75^\circ\text{C}$  (our specified upper limit on temperature at the wire). The additional length of wire required to extend the return paths away from the main cylinders also contributed to high coil total resistances. Since high RMS currents are required for the desired imaging applications, the power dissipated by the coils is significant ( $\sim 1250\text{W}$  for one coil @  $25\text{A RMS}$ ). In a mock-up of one quadrant of a coil, when a  $25\text{A RMS}$  current was applied with no cooling, the temperature of the quadrant rose from  $10^\circ\text{C}$  to  $100^\circ\text{C}$  in 2.5 min. With air-cooling only, a temperature rise from  $10^\circ\text{C}$  to  $35^\circ\text{C}$  in 4 min was observed. A more efficient cooling system was therefore required to ensure patient safety.

Water is one of the most efficient and economical cooling fluids available. Its heat capacity ( $C_p=4.18\text{J/g}^\circ\text{C}$ ) is approximately two times higher than other commonly available cooling fluids such as hydrocarbon oils (e.g. ethylene glycol). Assuming that all heat generated is transferred to the cooling water, and the maximum allowable temperature rise of the water is  $5^\circ\text{C}$ , a water flow of  $3.6 \text{ L/min}$  is required to remove  $1250\text{W}$  heat. Conventionally, water cooling channels for gradient coils are often constructed from copper tubing. For a compact gradient coil set, the competing demands of space limitations and the requirement of large cooling channel cross-section to ensure adequate volume flow rates necessitated the design of a novel cooling system. We designed this cooling system in separate modules, each module corresponding to a quadrant of a single gradient coil. Each module consisted of a skeleton of cooling channel spacers which were NC-milled from a  $3.0\text{mm}$ -thick polycarbonate sheet. This was covered on both sides with a very thin ( $0.25\text{mm}$  thickness) polycarbonate film (GE Plastics, General Electric Company, Pittsfield, MA, U.S.A.) to allow close thermal contact of the wires with the cooling water, while ensuring electrical insulation. Figure 6 shows one layer of cooling channels consisting of four modules. The film was bonded to the skeleton using UV-curing PVC-based bonding adhesive (Loctite 3311, Loctite Corporation, Mississauga, Canada). The tensile strength (to break) of the polycarbonate film was rated at  $9,000 \text{ PSI}$  according to ASTM D882 (American Standards of Testing Materials), and the burst strength was  $200\text{PSI}$  (ASTM D774). The modules were tested for flow uniformity and resistance to leaks by flowing water at  $13\text{L/min}$  for  $>5$  hours prior to permanent incorporation into the gradient coil structure. After incorporation into the gradient coil set, the modules were connected in parallel to lower the fluid resistance of the network of cooling channels, and thereby allow increased water flow rates.

This design allowed very close thermal contact between the wires and water in the cooling channels (while maintaining electrical isolation) and also provided a large surface area over which heat could be transferred to the water. The ability to test the cooling channel integrity separate from the gradient coil structure was vital in ensuring no electrical shorting due to water leakage. An additional benefit of constructing the cooling system from polycarbonate is that no electrical currents can be created in this material, and it is therefore not susceptible to eddy current generation like some copper systems. Since the thickness of the cooling channel module was only 3.5 mm, the maximum total wall thickness of the gradient coil structure was less than 3 cm. The assembled gradient coil structure including RF coil and water connections is shown in Figure 7.

### RF Coil

Several cylindrical RF coil designs exist that can be used in a transverse geometry for imaging the breast (i.e. with the coil axis perpendicular to the main magnetic field  $B_0$ ). These coils when oriented vertically produce  $B_1$  fields directed along either the horizontal  $x$  direction (e.g. saddle coils (6)) or along the vertical direction (e.g. solenoidal coils (7-8)).

The construction of an RF coil for operation inside our breast gradient coils is a difficult problem, in that the proximity of the RF coil to the gradient coils results in very strong inductive coupling and detuning of the RF coil (given that the gradient coil radius is constrained to be as small as possible for maximum efficiency). To determine the best RF coil design for our gradient coil set, two different RF coils were constructed and tested. The first coil constructed was a quadrature RF coil with two separate coils providing the perpendicular  $B_1$  components. In this arrangement, a simple 3-loop solenoidal coil provided the vertical mode, and a saddle coil built onto the same former provided the horizontal mode. The second coil constructed was a 16-rung high-pass birdcage RF coil designed for operation in a linear mode (recall that a birdcage coil cannot be used in quadrature mode in the vertical orientation because one of the modes would be parallel to  $B_0$ ). We chose this design over a saddle-coil arrangement because of the superior uniformity of  $B_1$  produced by the birdcage coil over the volume enclosed by the coil. A split cylindrical RF shield was constructed from fine copper screen and located immediately inside the smallest diameter gradient coil. The coils were tested for coupling to the gradient coils, the quality factors,  $Q$ , were measured, and coil performances compared.

### Diffusion Imaging

Preliminary diffusion measurements were made using a short- $T_2$  phantom consisting of  $\text{NiSO}_4$ -doped agarose gel ( $T_2 = 60\text{ms}$  at 1.89T), with a diffusion-sensitized spin echo sequence (Pulsed Gradient Spin Echo sequence (9)). Apparent Diffusion Coefficient (ADC) maps were calculated from a series of ten diffusion-weighted images with diffusion  $b$ -factors between 0 and 1000  $\text{s/mm}^2$ . Each of these images was the geometrical average of two images with equal diffusion-weighting but with opposite diffusion gradient polarity (10). This was done to remove the effects of diffusion-weighting cross-terms from interaction between the diffusion and imaging gradients. The ADC maps were obtained under three conditions: (1) using the standard whole-body manufacturer-supplied gradient coils for all imaging and diffusion-weighting gradients, (2) using our custom coils for all imaging and diffusion-weighting gradients, with the gradient strengths matched to those of the whole-body coils by applying an appropriately scaled current to the coils, and (3) using our custom coils for all imaging and diffusion-weighting gradients, with the imaging gradient strengths matched to those of the whole-body coils, but taking advantage of the increased gradient efficiency to apply higher strength, shorter diffusion-weighting gradients, thereby shortening the scan TE. In the first two experiments, the minimum TE required for diffusion weighting of  $b = 995 \text{ s/mm}^2$  was  $\text{TE} = 80\text{ms}$  (with diffusion gradient strength of 22  $\text{mT/m}$ ). TR was set to 600ms, the matrix size for the scan was 256 x 128, the image size was 8 x 8 cm, for a total scan time of 2.5 min for each image (5 min for each  $b$ -factor). Diffusion gradients were applied along the readout axis,  $x$ , for all experiments. For the third experiment, the TE was

decreased to  $TE = 46\text{ms}$  by increasing the strength of the diffusion-weighting gradient pulses by a factor of four ( $88\text{ mT/m}$ ) to obtain much larger b-factors with shorter diffusion pulses. All other parameters (including slice thickness) were matched to the first two experiments.

## RESULTS

### Coil Performance

The field produced by each of the three coils was calculated by direct numerical solution of the Biot-Savart Law for the wire paths, including return wire contributions. Calculated gradient efficiency for all three coils, together with the measured resistance and inductance are summarized in Table I below. Contour plots of calculated gradient uniformity for the Gz quadrupole coil are shown in Figure 8. Figure 8(a) shows the percentage deviation from gradient uniformity for a y-x plane through the center of the coils. A similar plot is shown in Figure 8(b) for a x-z plane, transverse to the coil axis, at a height equal to the center of the VOI, (i.e. located 5.9 cm below the top surface of the coils). These plots show the excellent gradient uniformity within the VOI that is predicted for the Gz coil. The gradient strength decreases near the ends of the coil, since the finite length of the coil causes a decrease in field strength. Similar results were obtained for the Gx gradient coil, with appropriate scaling for the number of wires and the coil radius. The performance of the modified target field Gy coil is shown in Figures 8(c) and 8(d). A larger deviation from gradient uniformity is present for this coil, compared to the Gx and Gz coils. This problem is inherent to any design for a Gy coil in the transverse orientation, since there is an additional gradient in the y-direction due to the natural field fall-off that occurs as the ends of the coil are approached. To create a Gy coil with optimum gradient efficiency, we would like to maximize  $|B_z|$  at both ends of the coil, with  $B_z$  a maximum in the +z direction at one end of the coil, and a maximum in the -z direction at the opposite coil end. The field fall-off inherent in this coil orientation works against the gradient we desire to create, since it necessarily results in a decrease in the magnitude of  $B_z$  as the coil ends are approached. Instead of working against the natural field fall-off toward the ends of the coil, we have designed a coil to produce  $B_z=0$  at the upper end of the coil, and a maximum in  $B_z$  toward the bottom end, similar to the asymmetric head coil design by Roemer (11). We used the target field approach to optimize the rate at which the field falls off toward the upper end of the coil to produce a linear variation in  $B_z$ . Although the region of acceptable gradient uniformity for our truncated target field coil is not as large as for the quadrupole coils, it compares favorably to the performance of the full target field design. We show in Figure 8(e) and 8(f) the corresponding plots from a complete 40 loop per side target field coil with the same dimensions as our modified coil (i.e. with return wire paths at the bottom of the cylinder as in Figure 3(b)). The region of acceptable gradient uniformity for our truncated target field coil is much larger than for the complete target field coil. In addition, the gradient efficiency is better for our truncated coil by a factor of 1.7, due to the larger number of windings that could be placed on the cylinder for our coil.

To verify the field simulations, gradient uniformity was tested by acquiring images of grid phantoms. Deviations from gradient uniformity are manifested in the images as geometric distortions. The phantoms consisted of acrylic cylinders filled with square plastic gridding and  $\text{CuSO}_4$ -doped 0.9% saline solution. The grid spacing was  $1.7\text{ cm} \times 1.7\text{ cm}$ , while the phantoms had an outer diameter of 12.5 cm and a height of 15 cm (extending 3cm higher than the top surface when placed inside the coils). The coil performance was tested on a clinical GE Signa imager, using our coils for all imaging gradients (with gradient strengths matched to the whole-body coils) in a standard spin echo pulse sequence. In general, local gradient coils often require modification of the compensation network for the gradient coil amplifiers since the coil inductances are quite different from the whole-body coils. Because the inductances of our breast coils were very similar to the whole-body coils, no modification of the network was necessary. Images of a grid phantom are shown in Figure 9 for planes corresponding approximately to the theoretical field plots shown

in Figures 8(a) and 8(b), and are evidence of the good gradient uniformity achieved over most of the VOI. These images were acquired using a Spin Echo sequence with TE = 20ms, TR = 500ms, matrix size = 256 x 256, and 2 NEX. The image size is 16 x 16 cm, and the VOI vertical extent is marked with arrows.

The first RF coil we constructed was a quadrature coil consisting of a solenoidal coil to provide the vertical mode, and a saddle coil to provide the horizontal coil. Unfortunately, the vertical mode was inductively coupled to both the y-gradient coil and to the RF shield and could not be tuned to the proton resonant frequency at 1.5T. We therefore chose to construct a coil that would operate in linear mode, with only a horizontal B<sub>1</sub> component present. We constructed a birdcage coil which creates a horizontal mode B<sub>1</sub> field with a high degree of homogeneity over a large volume. The unloaded Q of this coil (when located inside the gradient coil structure) was 80, whereas the Q for loading with a 0.9% saline phantom was 29.

Although the gradient strengths required for conventional imaging (10 mT/m) can be generated at less than 6A using these coils, higher currents are required for more demanding applications such as flow imaging and diffusion imaging. To test the effectiveness of the water cooling system, a DC current was applied to the coil with the highest total resistance, Gy, and the temperature rise was measured for different water flow rates by monitoring a thermocouple located on the surface of the wires. The temperature was monitored until equilibrium was achieved. Measured temperature rises are shown in Figure 10 for DC currents between 0 and 22A, and a cooling water flow rate of 8 L/min. Similar results were obtained for other flow rates, where the equilibrium temperature increased with decreasing flow rates, but did not change significantly from the results shown in Figure 10 for higher flow rates. This behavior has also been demonstrated in purely cylindrical gradient coils, and was modelled by Chu and Rutt (12) using an analysis based on fundamental heat transfer theory.

### Diffusion Imaging

ADC maps for a T<sub>2</sub>=60 ms NiSO<sub>4</sub>-doped agar phantom are shown in Figure 11, where Figure 11(a) shows the results obtained using the GE gradient coils and Figure 11(b) shows the results obtained using our gradient coils with diffusion gradient strengths four times higher than that of the GE coils. The mean ADC for all three experiments was the same within experimental error:  $(1.8 \pm 0.3) \times 10^{-3}$  mm<sup>2</sup>/s for the GE coils ( $\pm 30\%$  peak-to-peak),  $(1.8 \pm 0.3) \times 10^{-3}$  mm<sup>2</sup>/s for our gradient coils with diffusion gradient strengths matched to the GE coils,  $(1.9 \pm 0.2) \times 10^{-3}$  mm<sup>2</sup>/s for our gradient coils with diffusion gradient strengths four times higher than that of the GE coils, and TE=46ms. As expected, the observed S/N was increased by nearly a factor of 2 for the TE=46ms images compared to the corresponding b-factor images at TE=80ms.

### DISCUSSION

The performance and homogeneity of the gradient coils were in excellent agreement with theoretical predictions. The volume of acceptable gradient uniformity (<20% deviation) extended over most of our defined Volume of Interest for all three gradient coils. For this region, the theoretical plots of B<sub>z</sub> can be used to generate a gradient-warping algorithm for the coils (13) to correct spatial distortions in the images. Additionally, the known deviations from gradient uniformity can be used to correct calculations of diffusion-weighting b-factors (which will vary spatially across the VOI for our coils). Unfortunately, greater deviations from uniformity could not be avoided for the top 1 cm of the VOI near the upper edges of the coils for our coil designs. Deviations from uniformity of over 20% lead to large image distortions and likely cannot be satisfactorily corrected using conventional schemes. Many breast lesions occur close to the chest wall; to be clinically useful it is important to image accurately as close to the chest wall as possible. Several new gradient coils with improved gradient uniformity at the top edge of the coil have been reported recently (14-15). Future improvements on our coil design will focus on extending the



region of useable gradient beyond the top edge of the coil (16) as far as possible. For our preliminary clinical work with these coils, we will limit our study to patients with known lesions occurring in a region of the breast that falls within the 20% uniformity region of our gradient coils. This approach will allow us to implement diffusion- and flow-weighted imaging sequences under ideal conditions, in order to determine (a) the best imaging and motion-sensitizing parameters for visualizing breast lesions, (b) minimum required gradient strengths and uniformities and (c) to make an initial assessment of the clinical utility of this approach.

In future coil designs, it may be possible to extend the region of useable gradient farther into the cylinder in the -y direction by recessing the coils in the patient table, or by constructing a dedicated breast imaging table, thereby allowing higher aspect ratio coils. In this design, the coil assembly would be constructed to allow positioning on either side of the table, depending on which breast was being imaged. A fiberglass or Kevlar sheath covering the coil assembly and running the length of the patient table would serve the dual functions of isolating the patient from the electrical and cooling circuits, and providing an additional form of mechanical fixation to secure the coils on the table. Because the coils are not torque-balanced, it will be necessary to anchor the structure firmly, both from the point of view of vibration-induced imaging artifacts, and of patient safety.

The high gradient efficiencies of these coils will allow much higher spatial-resolution imaging than can currently be achieved in a clinical setting, and additionally, will provide very large amplitude motion-sensitizing gradients, thus facilitating diffusion imaging or flow imaging in small blood vessels with short echo times. T2 has been measured for human breast tissue, with reported values ranging between 60-150 ms (17-18). Recently, we reported T2 approximately 70 ms for human breast tumor (MCF7 human breast carcinoma) growing in a mouse mammary fat pad (19). More fibrous tumors can have significantly shorter T2s. For this reason, initial signal loss at  $b=0$  s/mm<sup>2</sup> due to T2-weighting of the image can severely limit the range of b-factors for which images can be obtained, which has the result of limiting the precision of the ADC measurement. Our approach is to shorten TE while maintaining diffusion weighting by increasing diffusion gradient amplitudes. This gives a substantial increase in initial signal intensity for  $b=0$  s/mm<sup>2</sup>, allowing high quality images to be obtained for much higher b-factors. Even in cases where signal loss from T2-weighting is not so severe as to limit ADC precision, the ability to obtain high diffusion weighting with short TE reduces dramatically the T2 contrast in an image. This will allow acquisition of a diffusion-weighted image where the contrast is determined mainly by tissue ADC, rather than by a mix of ADC and T2.

For velocity imaging, sensitization to coherent flows as slow as a few mm/s can be achieved using very high-amplitude, short duration bipolar pulses. The advantage of using short duration pulses for flow encoding is that diffusion-weighting of the pulse sequence is dramatically decreased. For a gradient strength of 250 mT/m, a rectangular bipolar gradient pulse of full period only 5 ms can be used to sensitize a pulse sequence to peak velocities (VENC) of 7.5 mm/s with minimal sensitization to higher orders of motions. The accompanying diffusion-weighting of this sequence is only 70 s/mm<sup>2</sup>, small enough to result in only minimal signal loss from diffusion (water flowing in the vasculature has two components to its motion - coherent motion due to flow, and incoherent motion due to diffusion inside the vessels).

A secondary important benefit that can be gained using high-efficiency gradient coils is that the ramp time required to attain imaging gradient strengths (10-25 mT/m) is decreased from that required by whole body coils by a factor of the efficiency (since the current slew rate is similar to whole body coils, and the required peak current is decreased). This will enable echo-planar imaging (and other fast imaging techniques) using conventional gradient amplifiers. Echo-planar imaging techniques have been proven much less susceptible to motion artifacts than conventional imaging sequences (20), and have recently been applied to diffusion imaging *in vivo* (21) with good results.

For rapid imaging pulse sequences, and for high-amplitude bipolar pulses, very rapid

changes in gradient polarity are required. Although the magnetic field amplitudes drop off quickly in the region above the coils, magnetic fields are also generated by the return wires on the horizontal plate, and excitation thresholds for cardiac stimulation must be considered. As an upper limit for one coil,  $|B|$  was calculated for the  $G_z$  coil at various distances above the return wires at the location of the highest wire density. The maximum  $dI/dt$  from our gradient coil amplifiers is 200A in 184  $\mu$ s. This produces  $dB/dt = 156$  T/s at 1 cm above the coil return wire plate, and  $dB/dt = 50$  T/s at 10 cm, compared to a recommended upper limit of 400 T/s for cardiac stimulation (22). The magnitude of these fields is relatively small at regions of concern with respect to magnetic stimulation such as the heart; however, peripheral nerve stimulation has been reported at  $dB/dt$  as low as 40 T/s in some patients (22). Theoretical field calculations will allow prediction of  $|B|$  and  $dB/dt$  for all pulse sequences before implementation, and pulse sequences will be tailored to adhere to maximum  $dB/dt$  and Peak  $|B|$  guidelines. Additionally, if peripheral nerve stimulation is reported for individual patients,  $dB/dt$  will be reduced below the stimulation threshold by increasing gradient switching times.

## SUMMARY

We have constructed a three-axis gradient coil set for imaging human breast tumours with diffusion and high-resolution velocity encoding. These coils create gradient efficiencies of up to 3.3mT/m/A with relatively low inductance ( $\leq 1000\mu$ H), and good gradient uniformity over most of the volume required for breast imaging. Preliminary diffusion results were obtained in a water phantom for b-factors as high as  $\sim 1000$  s/mm<sup>2</sup> for TE=46 ms. A compact, efficient water-cooling system was presented, which maintained coil temperatures at or below room temperature, even for RMS currents as high as 20A. This gradient/cooling module will allow for the first time clinical breast imaging using diffusion and microvascular flow-weighted protocols with high spatial resolution.

## ACKNOWLEDGEMENTS

This work was funded by the Breast Cancer Society of Canada and the Canadian Breast Cancer Research Initiative, National Cancer Institute of Canada. C. Maier was supported by a W.T. McEachern Scholarship, and by a U.S. Army Breast Cancer Predoctoral Fellowship.

## REFERENCES

1. D.S. Webster, K.H. Marsden, Improved apparatus for the NMR measurement of self-diffusion coefficients using pulsed field gradients. *Rev. Sci. Instrum.* **45**, 1232-1234 (1974).
2. K.C. Chu, B.K. Rutt, Quadrupole gradient coil design and optimization: a printed circuit board approach. *Magn. Reson. Med.* **31**, 652-659 (1994).
3. W.G. O'Dell, J.S. Schoeniger, S.J. Blackband, E.R. McVeigh, A modified quadrupole gradient set for use in high resolution MRI tagging. *Magn. Reson. Med.* **32**, 246-250 (1994).
4. R. Turner, A target field approach to optimal coil design. *J. Phys. D: Appl. Phys.* **19**:L147-151 (1986).
5. R. Turner, Gradient coil design: a review of methods. *Magn. Reson. Med.* **11**, 903-920 (1993).
6. P.W. McOwan, T.W. Redpath, A specialised receiver coil for NMR imaging of female breasts. *Phys. in Med. and Biol.* **32**, 259-263 (1987).
7. J.P. Hornak, J. Szumowski, R.G. Bryant, Elementary single turn solenoids used as the transmitter and receiver in MRI. *Magn. Reson. Imaging* **5**, 233-237 (1987).
8. L. Sun, L.O. Olsen, P.L. Robitaille, Design and optimization of a breast coil for magnetic resonance imaging. *Magn. Reson. Imaging* **11**, 73-80 (1993).
9. E.O. Stejskal, J.E. Tanner, Spin Diffusion Measurements: spin echoes in the presenche of a time-dependent field gradient. *J. Chem. Physics* **42**: 288-292 (1965).
10. M. Neeman, J.P. Freyer, L.O. Sillerud, A simple method for obtaining cross-term-free images for diffusion anisotropy studies in NMR microimaging. *Magn. Reson. Med.* **21**, 138-143 (1991).
11. P.B. Roemer, Transverse gradient coils for imaging the head. United States Patent No. 5177442, Jan.5, 1993.
12. K.C. Chu, B.K. Rutt, MR gradient coil heat dissipation. *Magn. Reson. Med.* **34**, 125-132 (1995).
13. M. O'Donnell, W.A. Edelstein, NMR imaging in the presence of magnetic field inhomogeneities and gradient field nonlinearities. *Medical Physics* **12**, 20-26 (1985).
14. A. Ersahin, H.K. Lee, O. Nalcioğlu, Asymmetric gradient coil design for high resolution breast imaging, in "Proc. SMR and ESMRMB, 3rd Meeting, Nice, 1995", p.954.
15. H.K. Lee, R. Raman, R. Slates, A. Ersahin, O. Nalcioğlu, An optimized gradient coil for breast imaging, in "Proc. SMR and ESMRMB, 3rd Meeting, Nice, 1995", p.955.
16. B.A. Chronik, B.K. Rutt, Constrained length minimum inductance gradient coil design, in "Proc. ISMRM, 5th Meeting, Vancouver, B.C., Canada, 1997".
17. D.Z.J. Chu, W.S. Yamanashi, J. Frazer, C.F. Hazlewood, H.S. Gallager, A.W. Boddie, R.G. Martin, Proton NMR of human breast tumors: correlation with clinical prognostic parameters. *J. Surgical Oncology* **36**, 1-4 (1987).
18. S.J. Graham, M.J. Bronskill, J.W. Byng, M.J. Yaffe, N.F. Boyd, Quantitative correlation of breast tissue parameters using MR and X-ray mammography. *British J. of Cancer* **73**, 162-168 (1996).
19. C.F. Maier, Y. Paran, P. Bendel, B.K. Rutt, H. Degani, Quantitative diffusion imaging in implanted human breast tumors. *Magn. Reson. Med.* **37**, 576-581 (1997).
20. R. Turner, D. LeBihan, Single-shot diffusion imaging at 2.0 Tesla. *J. Magn. Reson.* **86**, 445-452 (1990).
21. R. Turner, D. LeBihan, A.S. Chesnick, Echo-planar imaging of diffusion and perfusion. *Magn. Reson. Med.* **19**, 247-253 (1991).
22. J.P. Reilly, Principles of nerve and heart excitation by time-varying magnetic fields in "Biological effects and safety aspects of NMRI and spectroscopy", Ann. N.Y. Acad. Sci. **649**, 96-107 (1993).

Table I. Coil Performance Characteristics

	Mean Diameter (cm)	Efficiency (mT/m/A)	Inductance ( $\mu$ H)	Resistance ( $\Omega$ )
Gx (quadrupole)	21.1	2.9	754	2.3
Gy (fingerprint)	19.5	1.7	829	2.6
Gz (quadrupole)	18.1	3.3	1024	1.9

## FIGURE CAPTIONS

**Figure 1.** Schematic showing orientation of local breast gradient coil in magnet.

**Figure 2.** Cross-section of complete gradient coil assembly showing location of RF coil and water cooling modules.

**Figure 3.** (a) Quadrupolar current density with 56 windings (b) Target-field design transverse coil. The "primary wire" component is almost entirely responsible for generation of the transverse gradient for the conventional coil orientation with its axis along  $z$ .

**Figure 4.** Schematic showing assembly of all three gradient coils. While two horizontal return wire plates were required for the  $G_x$  coil, only one plate each was necessary for construction of the  $G_y$  and  $G_z$  coils, allowing the coils to be wound with wire separately, then assembled as shown.

**Figure 5.** (a)  $G_x$  quadrupole coil with 216 windings. (b)  $G_y$  coil showing placement of the "return wires" on a horizontal plate.

**Figure 6.** Cooling channels for one gradient coil showing quadrant construction.

**Figure 7.** Assembled gradient coil module showing RF coil and cooling channels.

**Figure 8.** (a)-(b) Contour plots showing percentage deviations from gradient uniformity for the  $G_z$  coil over (a) an axial plane ( $x$ - $y$ ) showing the entire VOI with the top edge of the plot corresponding to the top surface of the coils. The outer circumference of the VOI is at 6.75cm as indicated by dashed lines. (b) a coronal plane ( $x$ - $z$ ) located at the center of the defined VOI, i.e. at  $\sim 3$  cm above the geometric coil center. In Figure 8.(a), the contours are symmetric around  $y=0$ cm with some small deviations due to return-wire contributions. (c)-(d) The corresponding plots for the constructed  $G_y$  coil shown in Fig. 5(b). (e)-(f) The corresponding plots for a conventional transverse coil with return wires on the cylinder, as in Fig. 3(b).

**Figure 9.** Spin-echo images of a grid phantom acquired (a) for an axial plane ( $x$ - $y$ ) and (b) for a coronal plane ( $x$ - $z$ ) with the specialized breast quadrupole gradient coils. The input current strength required for the least efficient ( $G_y$ ) coil was approximately fourteen times less than that required for the corresponding GE coil.

**Figure 10.** Temperature response of assembled gradient coils to a DC current applied to the coil with the highest resistance ( $G_y$ ) monitored at the surface of the  $G_y$  coil where the winding density was greatest.

**Figure 11.** ADC maps of a  $T_2=60$  ms agar phantom obtained (a) using the GE coils to provide all diffusion and imaging gradients,  $TE=80$  ms, and (b) using the breast gradient coils to provide all gradients, where the diffusion gradient strengths were four times the GE gradient strengths, and  $TE=46$  ms. In all cases, the ADC maps were constructed from ten images with  $b=0$  to  $1000$  s/mm<sup>2</sup>.

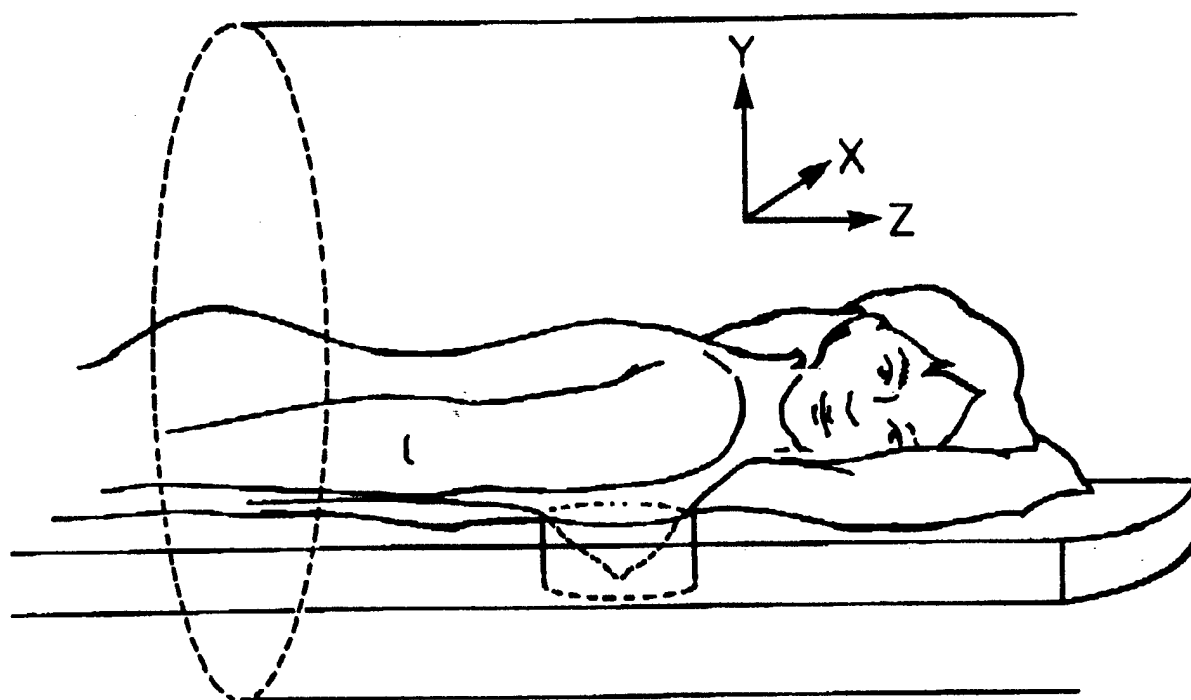


Figure 1.

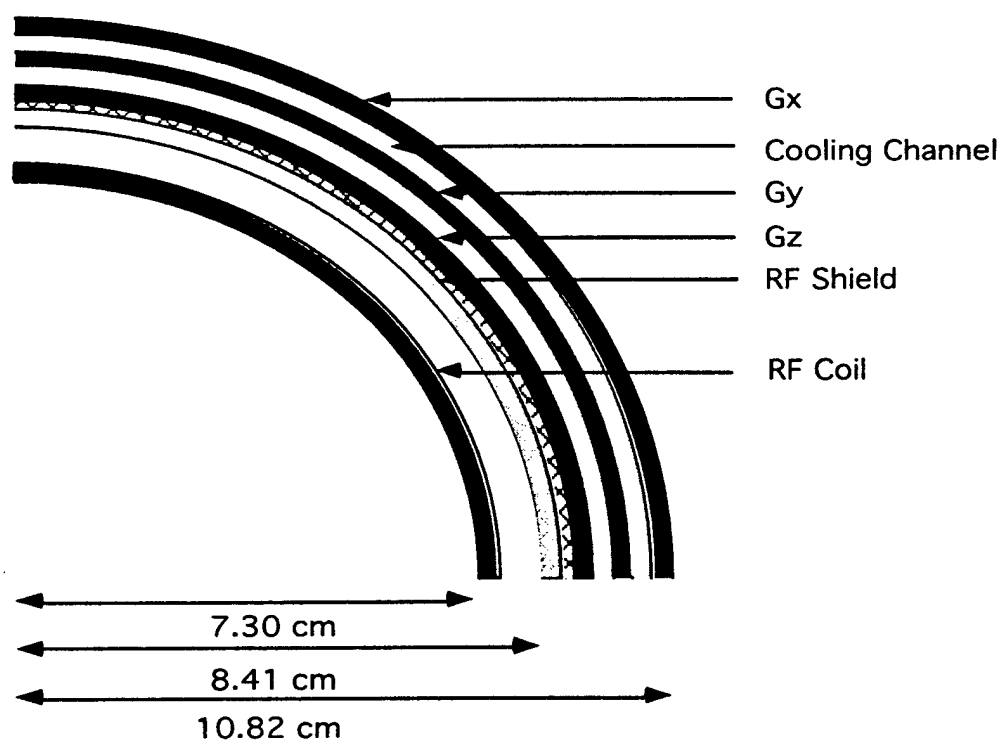


Figure 2.

Figure 3(a).

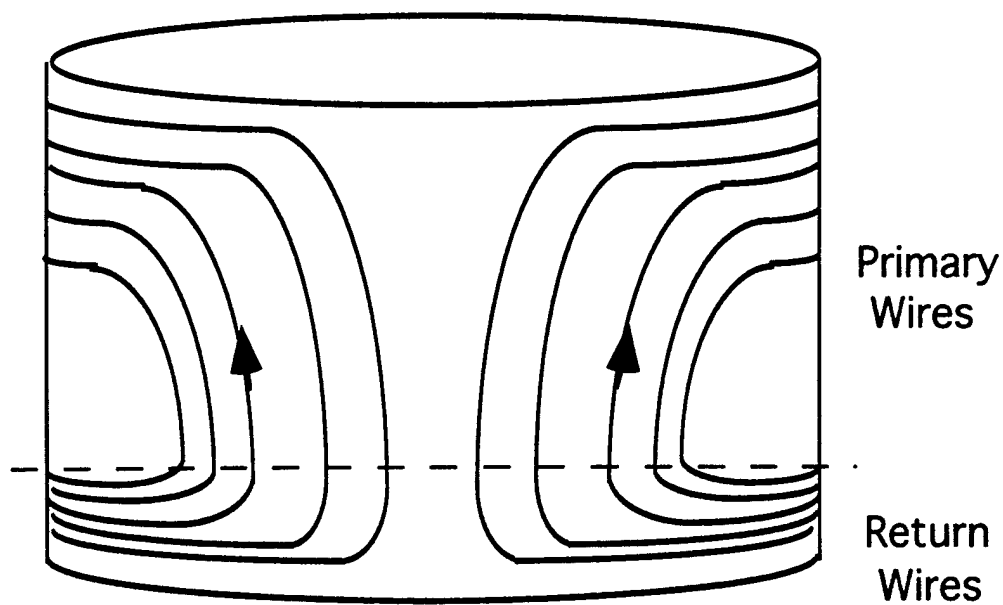
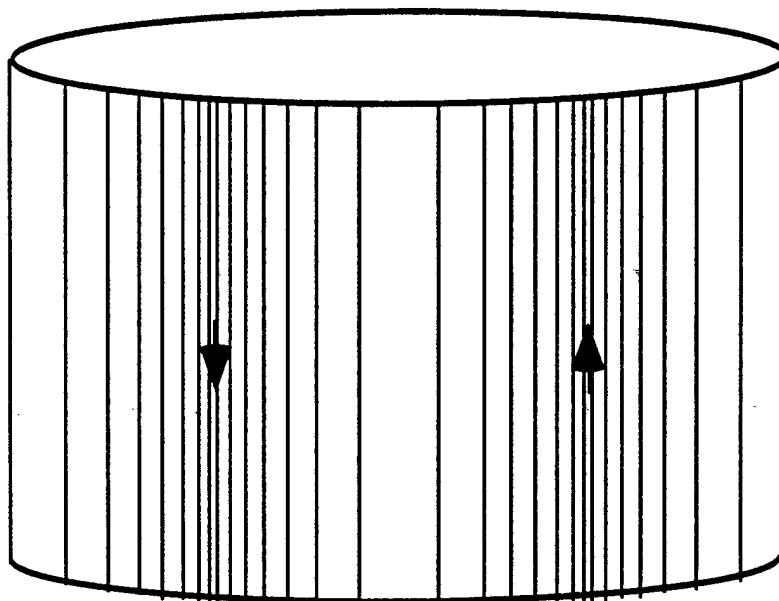


Figure 3(b).

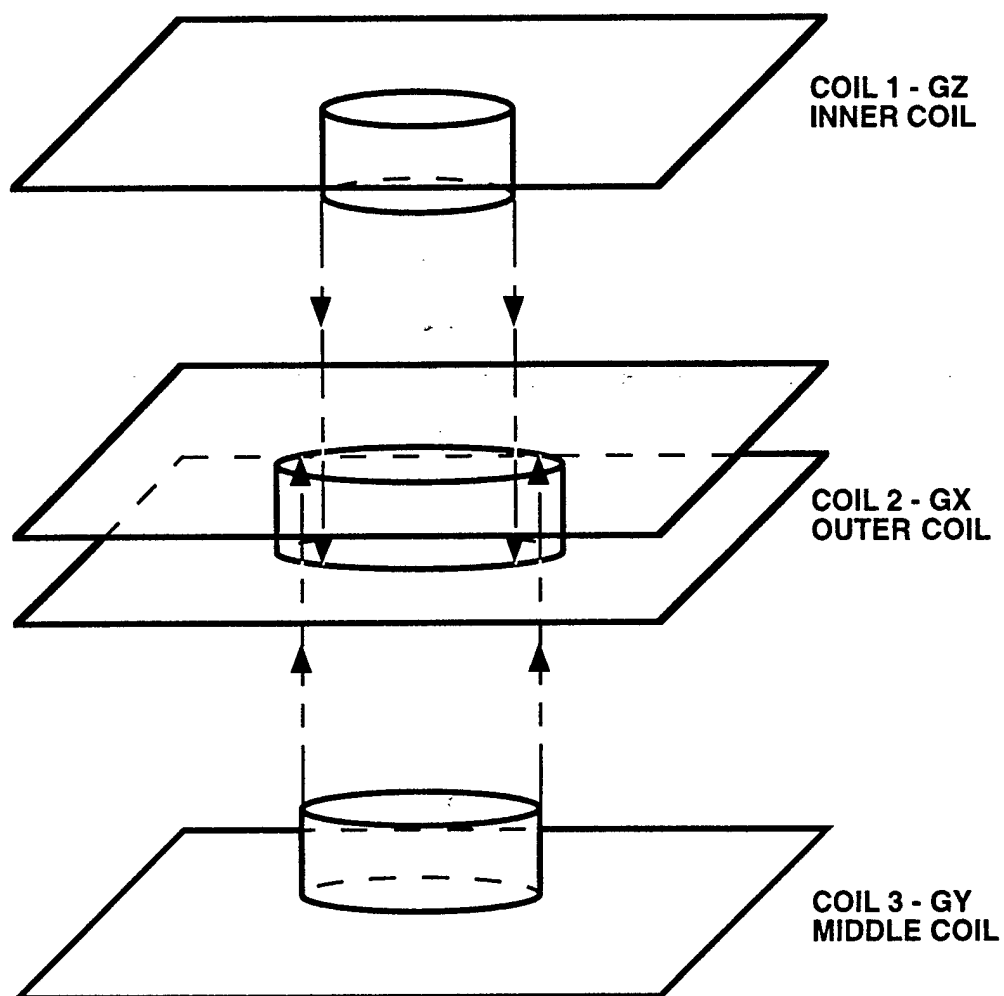


Figure 4.



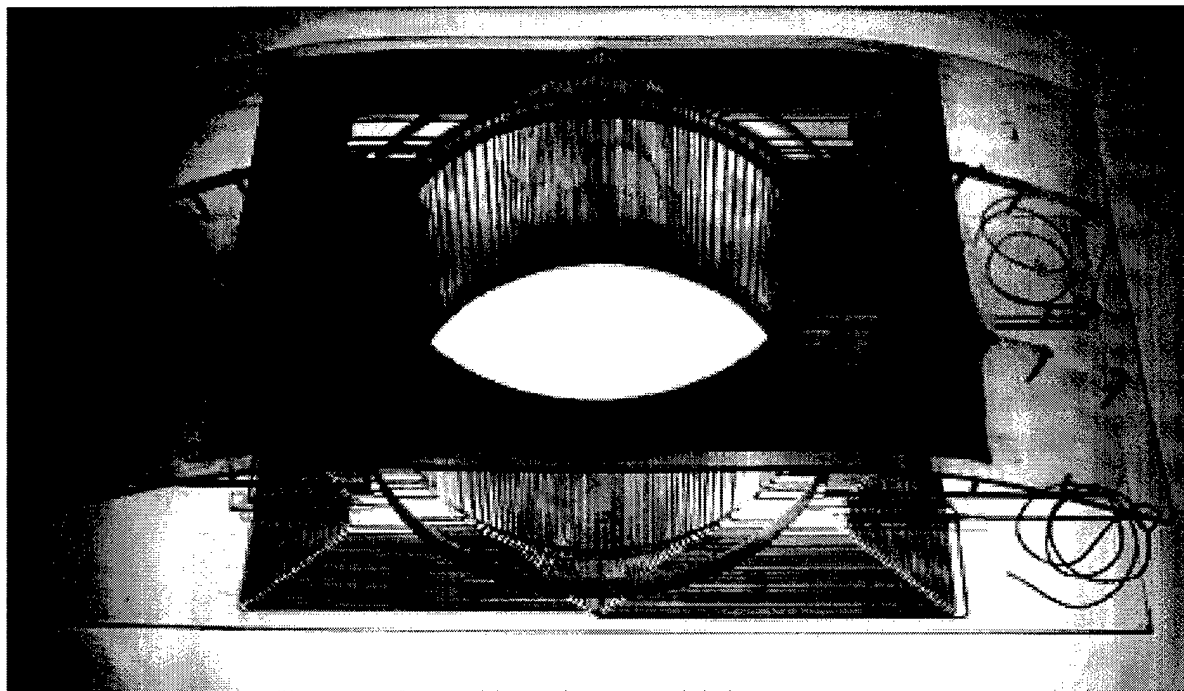
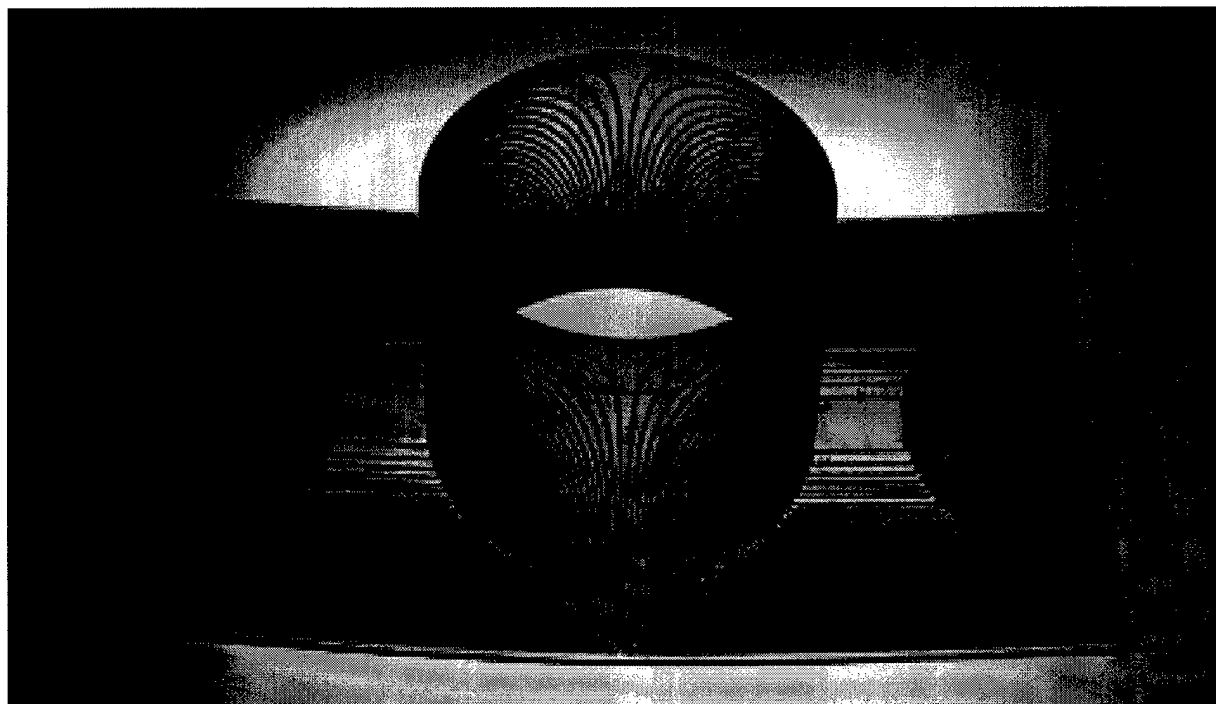


Figure 5(a).



Fiaure 5(b).

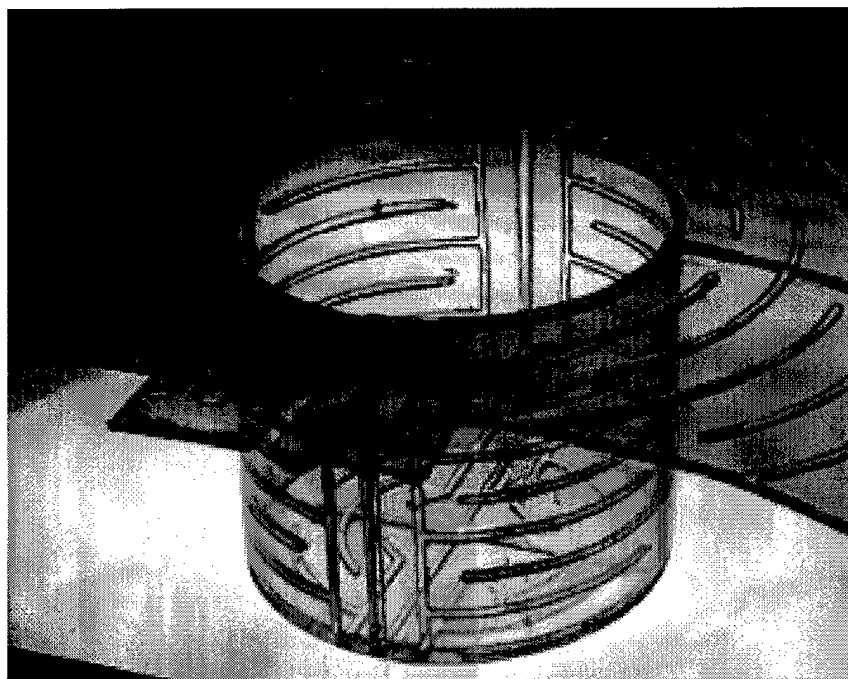


Figure 6.

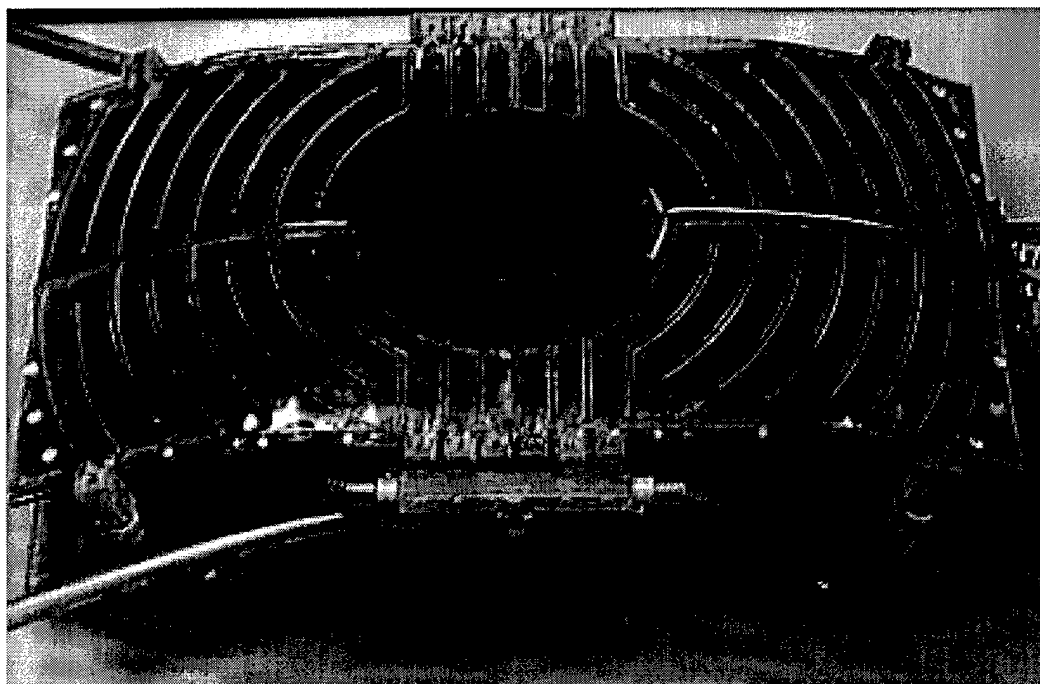


Figure 7.

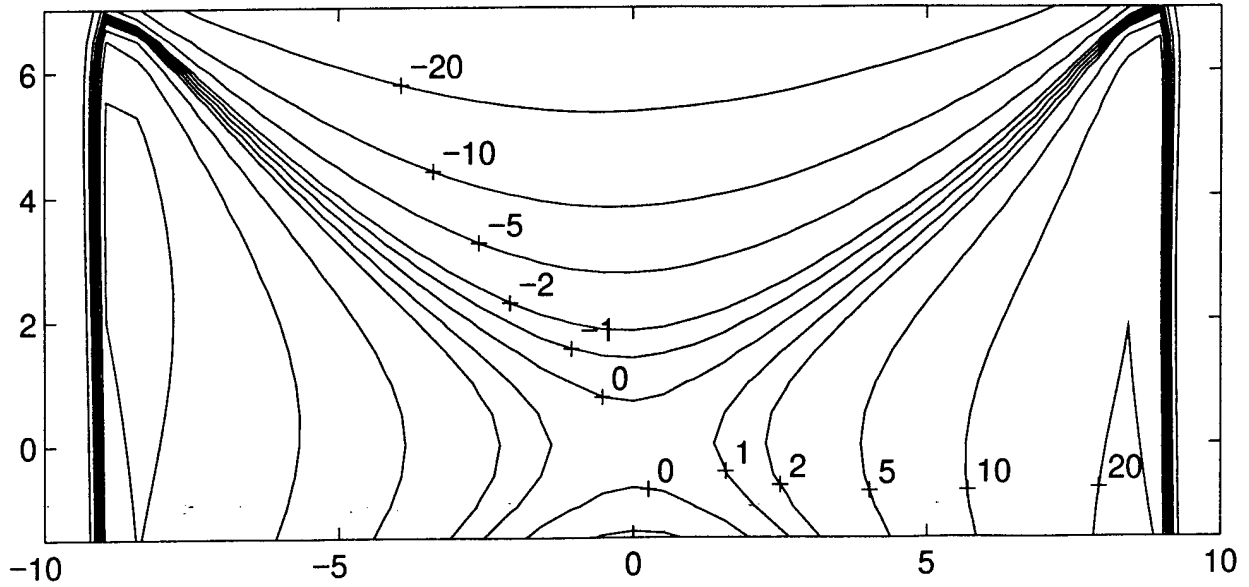


Figure 8a.

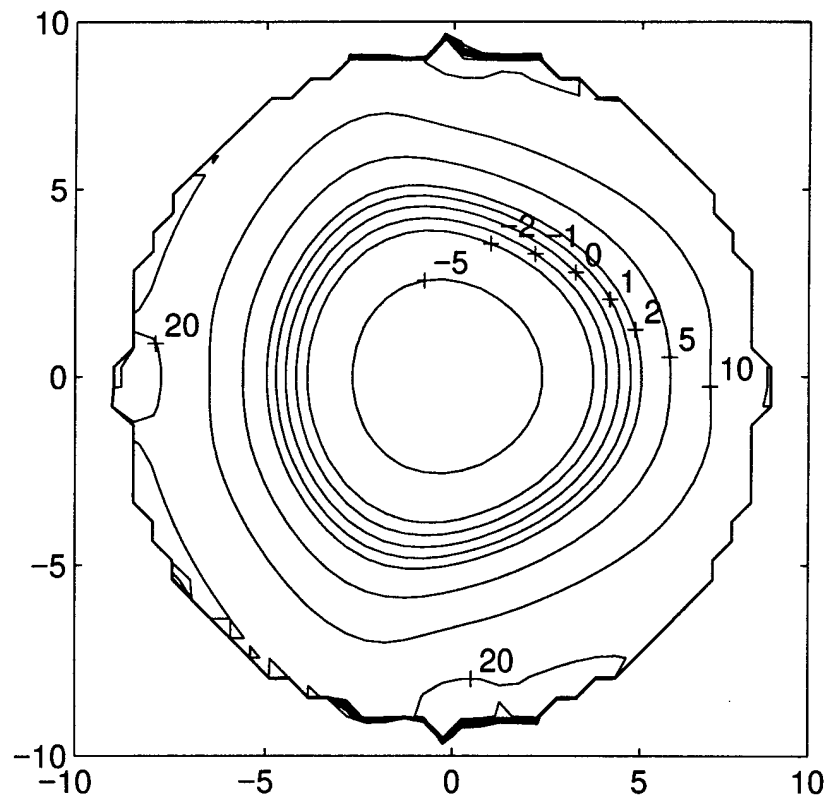


Figure 8b.

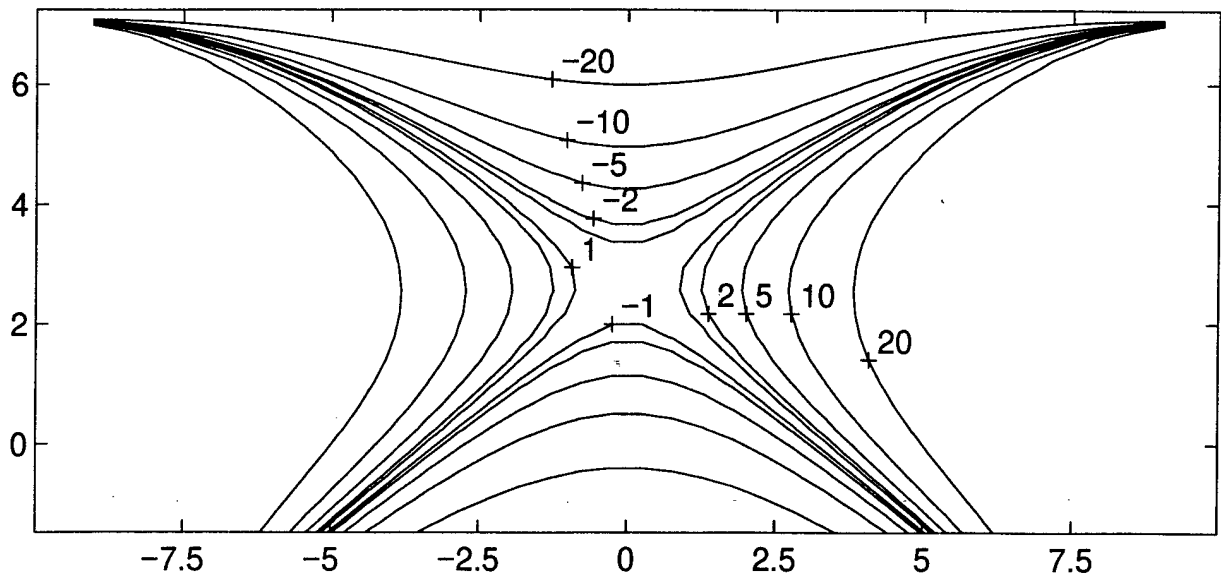


Figure 8c.

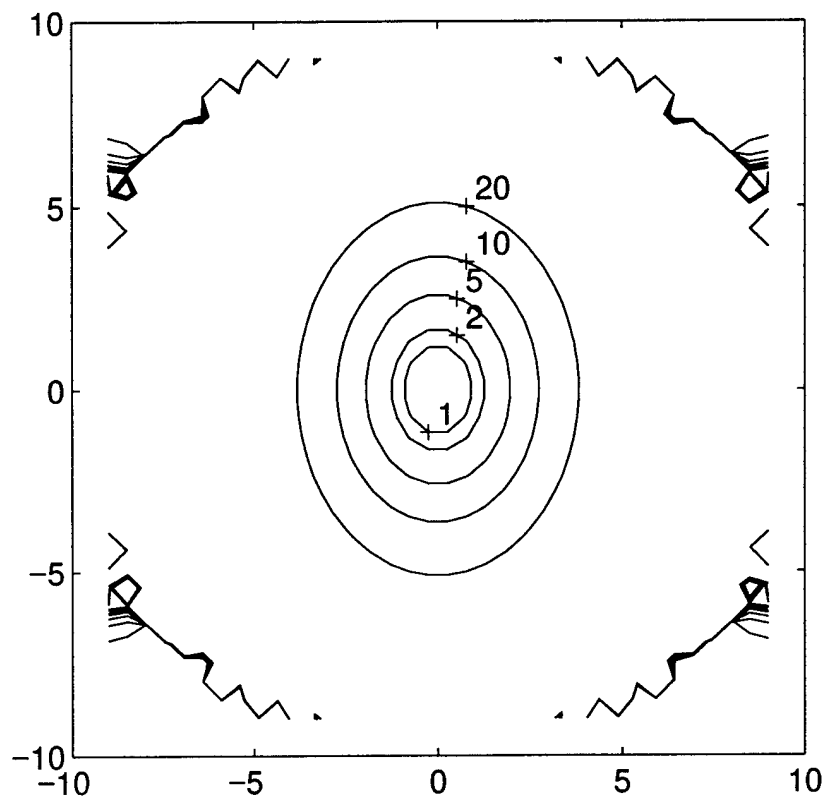


Figure 8d.

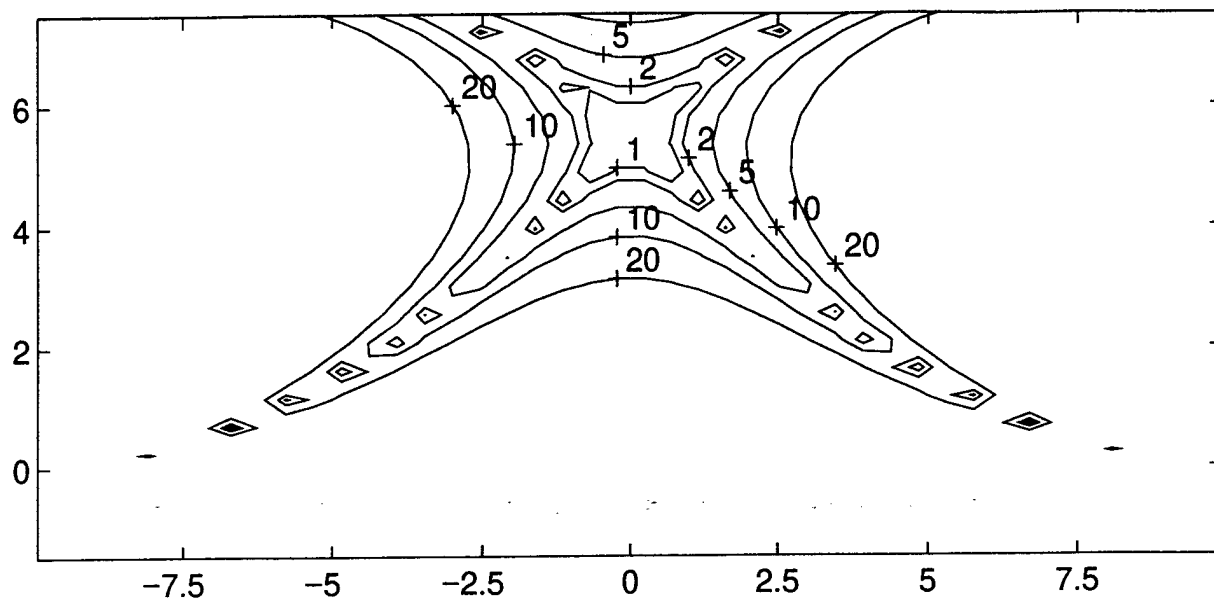


Figure 8e.

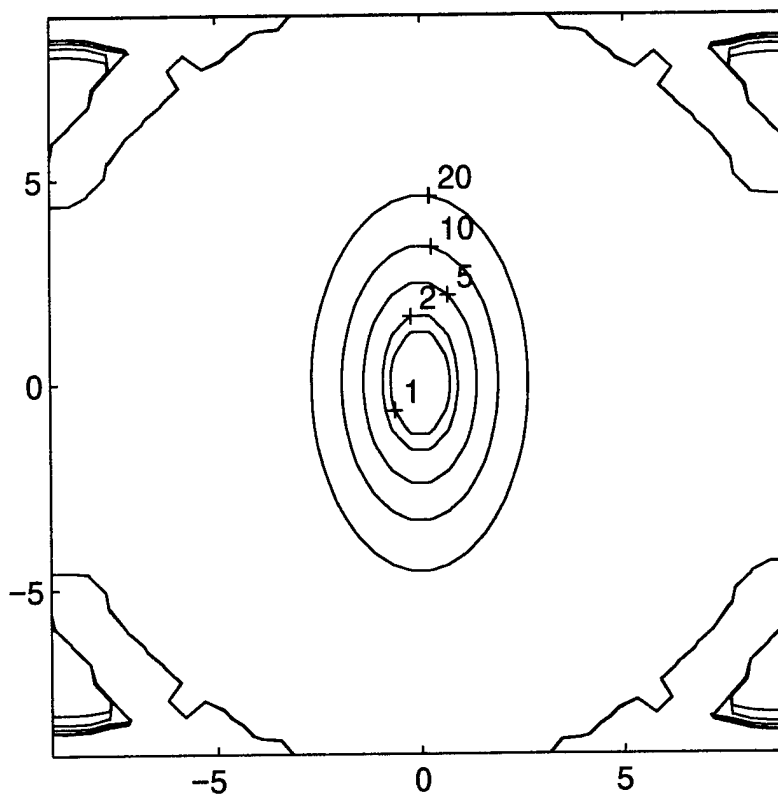
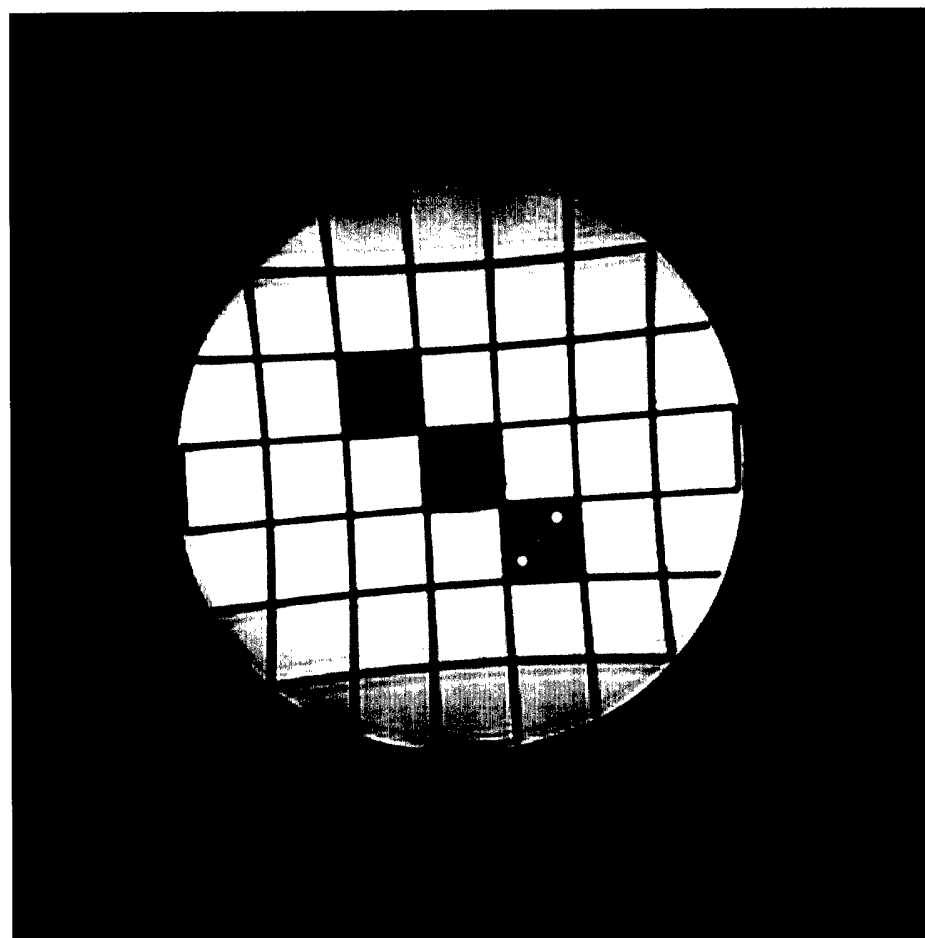
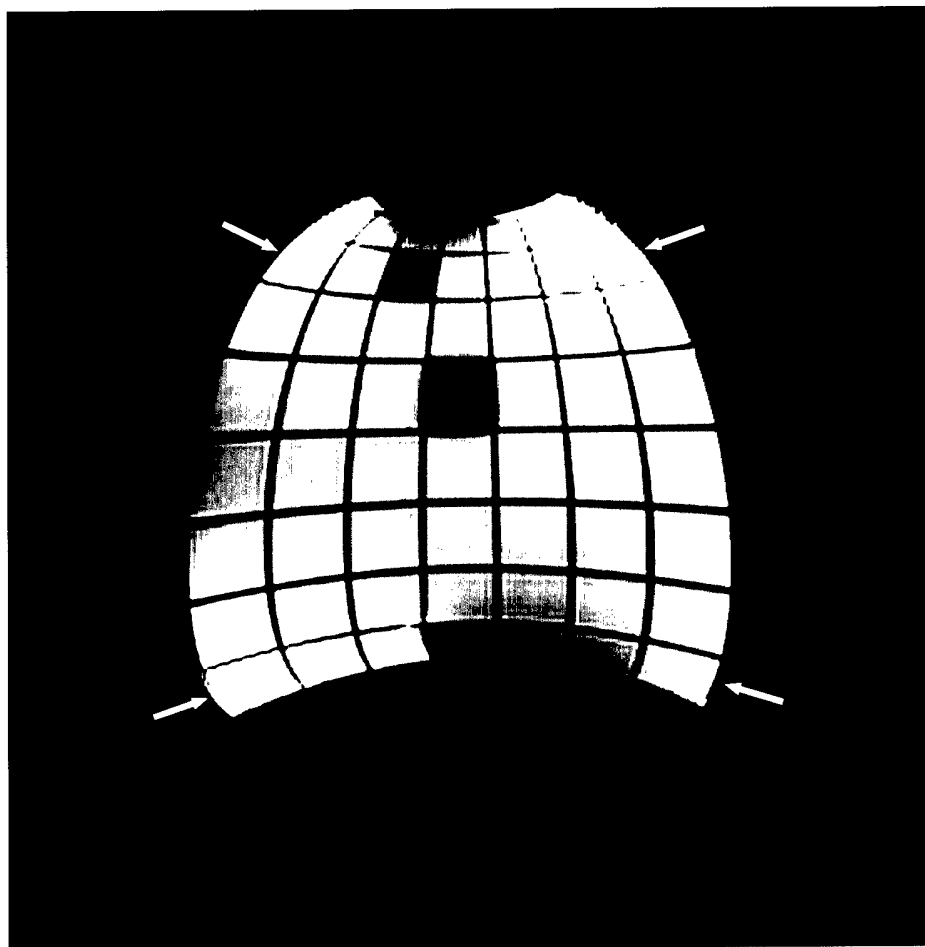


Figure 8f.



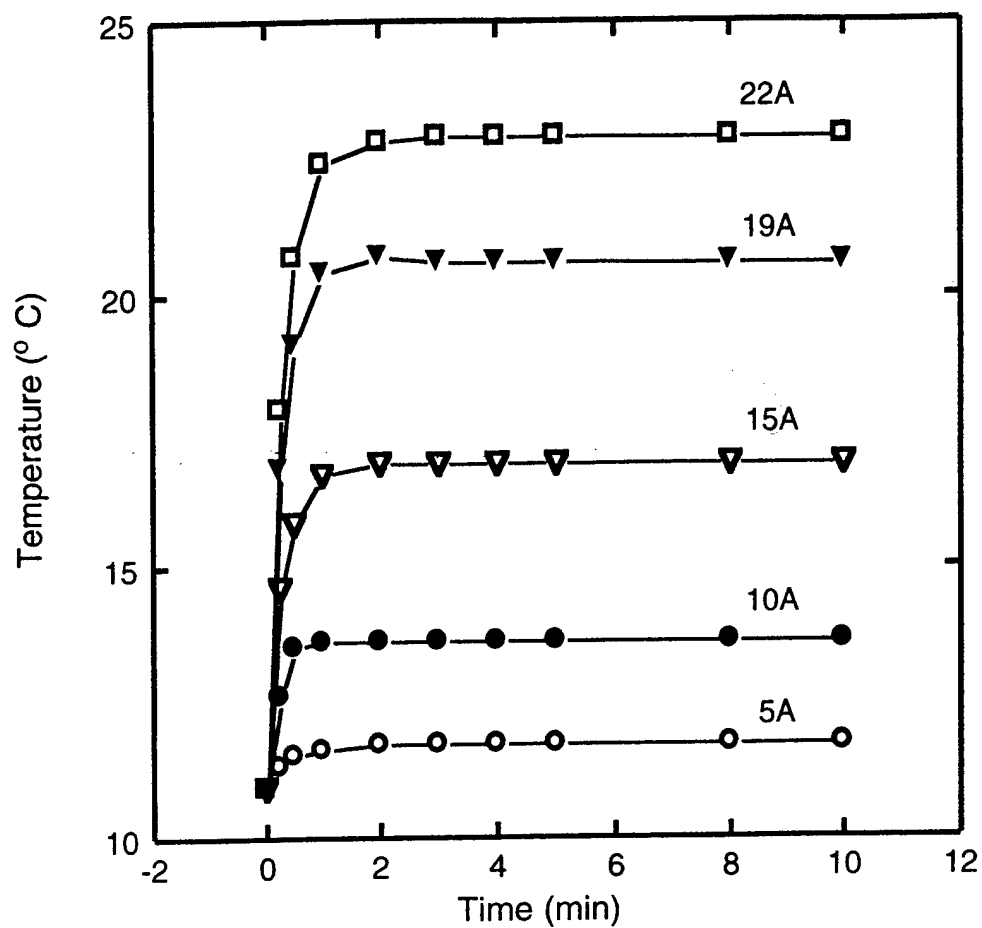
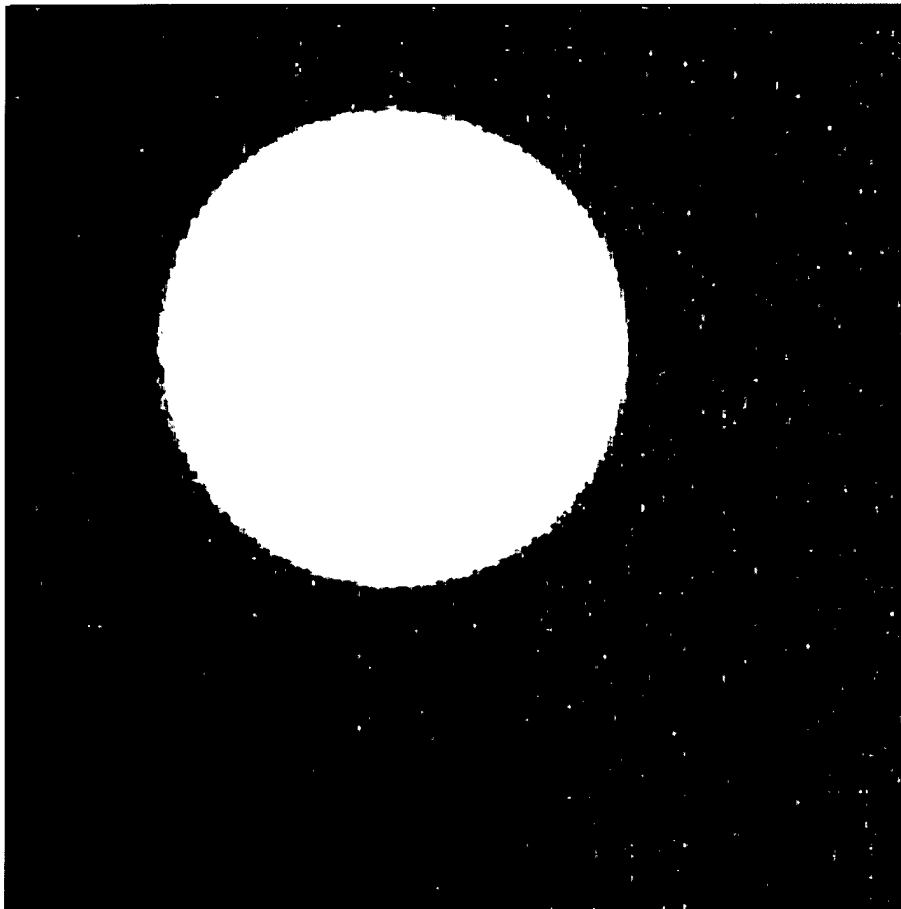
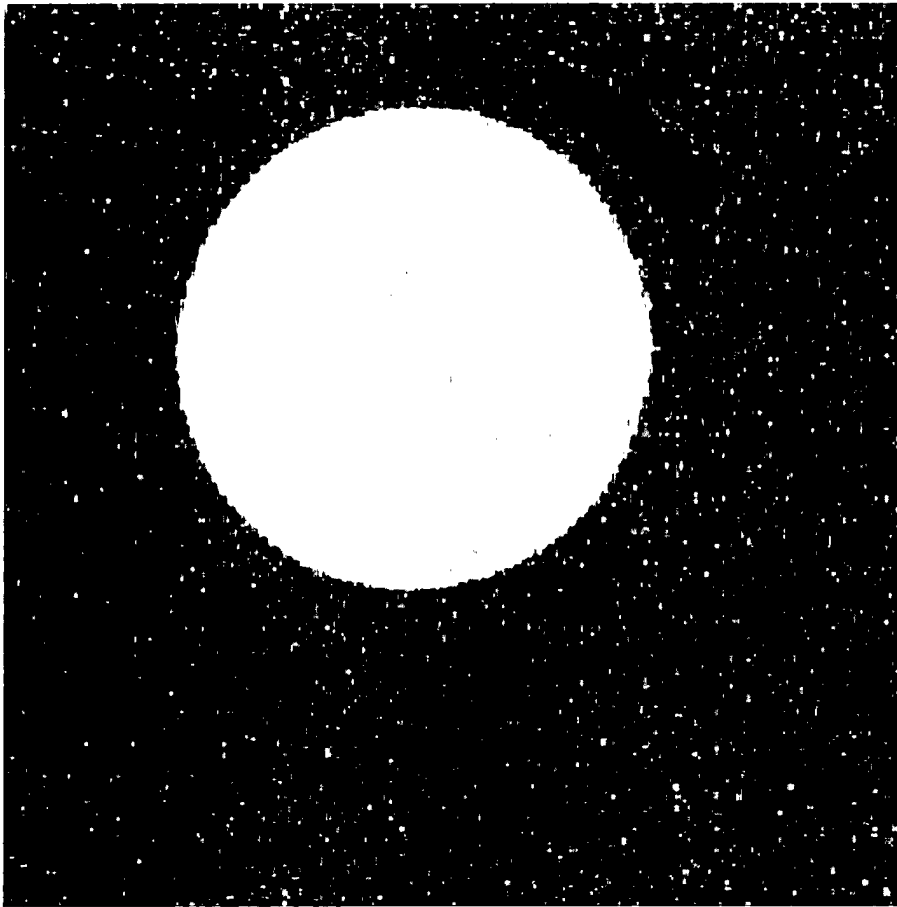


Figure 10.





# Quantitative Diffusion Imaging in Implanted Human Breast Tumors

Cynthia F. Maier, Yael Paran, Peter Bendel, Brian K. Rutt, Hadassa Degani

Quantitative diffusion measurements were performed in tumors arising from inoculation of nude mice with two human breast cancer cell lines (MCF7 and T47D) to evaluate the specificity of this technique for characterizing solid tumors. ADC maps were compared to histology and correlated well with gross tumor morphology. Measured ADCs were highly specific for viable and necrotic tumor in the five T47D tumors included in this study ( $P < 0.02$ ), while only two of the five MCF7 tumors studied developed distinguishable areas of necrosis. No statistically significant difference was observed in ADCs from viable tumor between the different cell lines ( $P > 0.05$ ).

**Key words:** magnetic resonance imaging; diffusion; breast cancer; necrosis.

## INTRODUCTION

Magnetic resonance diffusion imaging is a technique that has recently been applied to imaging human tissues *in vivo*. The rate of water diffusion in tissue directly reflects intrinsic tissue parameters such as tissue microstructure and the degree of water compartmentalization, and the concentration of proteins and macromolecules in the water's environment. In tumors, water diffusion is an important process that has implications for nutrient delivery and clearance.

Preliminary diffusion measurements in animal tumor models using MRI have demonstrated potential for providing information about gross tumor morphology and for detecting tumor necrosis (1–3). It has been suggested that tumor response to chemotherapy or radiation therapy could be monitored non-invasively using an MR-imaging technique based on diffusion (3). To date, however, most spatially resolved, *in vivo* studies of water diffusion have been based on a single diffusion-weighted image, which provides only qualitative information. A more quantitative approach is necessary, where apparent diffusion coefficients (ADCs) are measured with high

spatial resolution for the tumor and the specificity of these ADCs for characterizing tumors is assessed. In recent work by Eis *et al.* (4), quantitative analysis of the ADC in rat brain tumors demonstrated potential for differentiating tumors from normal brain tissue. However, the low spatial resolution of images in this study did not allow differentiation of morphologically distinct features (e.g., areas of necrosis or fibrosis) within the tumors.

The purpose of this work was to demonstrate the potential for diffusion imaging as a method for characterizing solid tumors, and for providing information about tumor morphology on a cellular level. We evaluated water diffusion by using MRI in two different mouse tumor models of human breast cancer (MCF7 and T47D cell lines). A range of tumor sizes were studied, where some of the tumors were allowed to grow to large sizes, resulting in cell death and necrosis in the interior of the tumor. ADC maps were calculated for the tumors, and average ADCs measured for regions of viable neoplastic tissue and for necrosis. These quantitative diffusion measurements were compared to histopathology and the specificity of the ADC for identifying different tumor components was evaluated.

## MATERIALS AND METHODS

### Tumor Model

MCF7 and T47D human breast cancer cells were cultured and prepared for inoculation as described previously (5, 6). Ten female CD1-NU athymic mice (8 weeks old), were subcutaneously inoculated in the mammary fat pad with approximately  $10^7$  cells in a volume of 0.4 ml (five mice for each tumor model). Before injection of the cancer cells, a pellet of  $17\beta$  estradiol was implanted under the skin of the back (0.72 mg/pellet, 60 day release, Innovative Research of America, Sarasota, FL) to facilitate tumor growth. The tumors were allowed to develop for 4–12 weeks, to sizes ranging between 0.5 and 2.0 cm in diameter. In larger tumors, regions of necrosis developed mainly in the centers of the tumors, presumably as a result of inadequate nutrient and oxygen delivery to these areas.

### MRI Measurements

Mice were anesthetized before imaging by using Pentil diluted in PBS solution (Pentobarbitone sodium, CTS Chemical Industries, Tel-Aviv, Israel) by an intraperitoneal (IP) injection (0.06 mg/g). Follow-up injections (0.03 mg/g) were administered IP on an hourly basis after the initial injection, via an infusion line that extended outside the imager. To prevent motion during the examination, the mice were immobilized for the course of the MR experiments by laying them in prone position on a home-

### MRM 37:576–581 (1997)

From the Tom Lawson Family Imaging Research Laboratories, John P. Roberts Research Institute, and the Departments of Medical Biophysics and Diagnostic Radiology, University of Western Ontario, London, Ontario, Canada (C.F.M., B.K.R.); and the Department of Biological Regulation, Weizmann Institute of Science (Y.P., H.D.), and the Department of Chemical Services, Weizmann Institute of Science (P.B.), Rehovot, Israel.

Address correspondence to: Cynthia Maier, Ph.D., University of Western Ontario, John P. Roberts Research Institute, 100 Perth Drive, N6A 5K8 London, Ontario, Canada.

Received March 15, 1996; revised September 30, 1996; accepted October 2, 1996.

This work was supported by the the Canadian Women for the Weizmann Institute. C.M. was supported by a W. McEachern Fellowship, the Canadian Breast Cancer Research Initiative, and the Breast Cancer Society of Canada.

0740-3194/97 \$3.00

Copyright © 1997 by Williams & Wilkins

All rights of reproduction in any form reserved.

made mouse tray and taping the lower half of the body securely to the tray. The upper abdomen and chest were not constrained so that respiration would not be impaired. A water standard was placed near the tumor for each of the experiments. The room temperature was maintained during the examination at 25–30°C.

$^1\text{H}$  MR images of the tumors were collected at 4.7 Tesla by using a horizontal bore Biospec 4.7/30 animal imager (Bruker, Karlsruhe, Germany), and a custom-built 7.5-cm diameter radiofrequency (RF) coil. Gradient hardware consisted of unshielded gradient coils with a maximum gradient strength of 48 mT/m at a rise time of 500  $\mu\text{s}$ , using standard gradient pre-emphasis provided by the manufacturer. A transverse pilot scan was used to define coronal slices covering the whole tumor. A standard multislice PGSE sequence was used with  $TE/TR = 48\text{ ms}/2400\text{ ms}$ ,  $\Delta = 22.4\text{ ms}$ ,  $\delta = 16.2\text{ ms}$  ( $\Delta$  and  $\delta$  are defined as in Fig. 1).  $TE$  was kept as short as possible to minimize signal loss due to  $T_2$  relaxation (our previous measurements of  $T_2$  in these tumors gave an average value of approximately 68 ms). A series of 13 diffusion-weighted images was obtained, with diffusion  $b$  values ranging from  $b = 0\text{ s/mm}^2$  to  $b = 754\text{ s/mm}^2$  ( $b = \gamma^2 g^2 \delta^2 (\Delta - \delta/3)$ , where  $\gamma$  is the magnetogyric ratio and  $g$  is the diffusion-encoding gradient strength as defined in Fig. 1). Nine of these 13 images were sensitized to incoherent blood flow with  $b$  values less than  $220\text{ s/mm}^2$  (7–10). Diffusion-weighting was varied by changing the amplitude of the diffusion gradients while keeping all timing parameters constant. Phase-cycling was performed to cancel the effects of RF inhomogeneities on the  $180^\circ$  refocusing pulse. Images were obtained with 3 cm field of view, slice thickness of 1 mm, a matrix size of  $64 \times 256$  pixels (in-plane resolution of  $472 \times 118\text{ }\mu\text{m}$ ) and two averages for an acquisition time of 5 min. and 10 s. The raw data were zero-filled and Fourier transformed to give images with  $256 \times 256$  pixels.

For the imaging gradient strengths required at this spatial resolution, significant systematic errors are introduced into the determination of diffusion coefficients by the interaction of the imaging gradients with the diffusion gradients (11, 12). We employed a method for eliminating this contribution to the  $b$  weighting that was first proposed by Neeman *et al.* (13), where images are acquired by using both positive and negative diffusion gradients for each  $b$  value and the geometric average of these images is calculated. This method also allows the elimination of unwanted contributions to the  $b$  value from the interaction of the diffusion gradients with background gradients arising from susceptibility variations within the sample.

Following the diffusion imaging sequence, high-resolution  $T_2$ -weighted spin echo images were acquired for the same slice locations to provide a reference for the diffusion data. Such  $T_2$ -weighted images have previously been correlated with histology (5) and allow identification of necrotic regions, viable tumor, and fibrous tissue. The images were acquired using  $TE/TR = 68\text{ ms}/2400\text{ ms}$ , matrix size =  $128 \times 256$  pixels (in-plane resolution of  $236 \times 118\text{ }\mu\text{m}$ ) and four averages. The other parameters were as for the diffusion images. The acquisition time for the  $T_2$ -weighted images was 20 min. The total

length of time required for the MR examination including setup and localizers was approximately 3 h per animal.

### Image Analysis

Images were transferred to a DEC 3000 workstation for analysis where image analysis was performed by using MATLAB software Version 4.2 (The Mathworks, Inc. Natick, MA). One image for each  $b$  value was obtained by geometrically averaging positive-gradient and negative-gradient images according to the method proposed by Neeman (13).

Average ADCs were calculated for regions of interest (ROIs) in areas that were identified as viable or as necrotic by comparison to the high-resolution  $T_2$ -weighted scans. These regions were selected on the  $T_2$ -weighted scan based on their relative signal intensities, and morphological appearance. The regions were selected as being “clearly” identifiable as either necrotic or viable. Where possible, one ROI for each of viable and necrotic tissue were chosen per slice. For these calculations, the standard deviation of signal intensities within the ROI was taken as the uncertainty in the mean signal intensity. Fits having  $r < 0.97$  (14) were rejected. The ADC of the water standard was obtained as a reference for each tumor.

Maps of the apparent diffusion coefficient were calculated for each slice on a pixel-by-pixel basis from the slope of a linear least-mean-squares fit of the natural logarithm of signal intensity to the  $b$  factor. The noise in signal intensity for each pixel was estimated by the standard deviation of signal intensities in a ROI in the background.

### Histology

Immediately after the MR imaging experiments, two mice with MCF7 tumors and two mice with T47D tumors were sacrificed to provide a comparison to histology. The tumors were surgically removed, fixed in 10% formaldehyde solution, imbedded in paraffin, and sectioned to correspond to the MR imaging planes. Representative

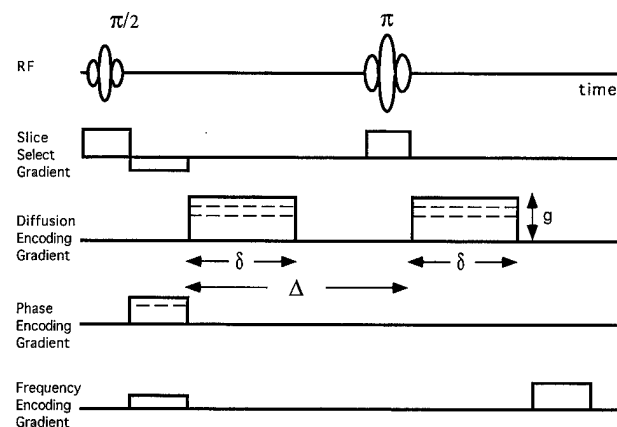


FIG. 1. Multislice PGSE sequence used for diffusion measurements.  $TE/TR$  for the sequence =  $48\text{ ms}/2400\text{ ms}$ ,  $\Delta = 22.4\text{ ms}$ ,  $\delta = 16.2\text{ ms}$ . Diffusion-encoding gradients were on the slice-select axis.

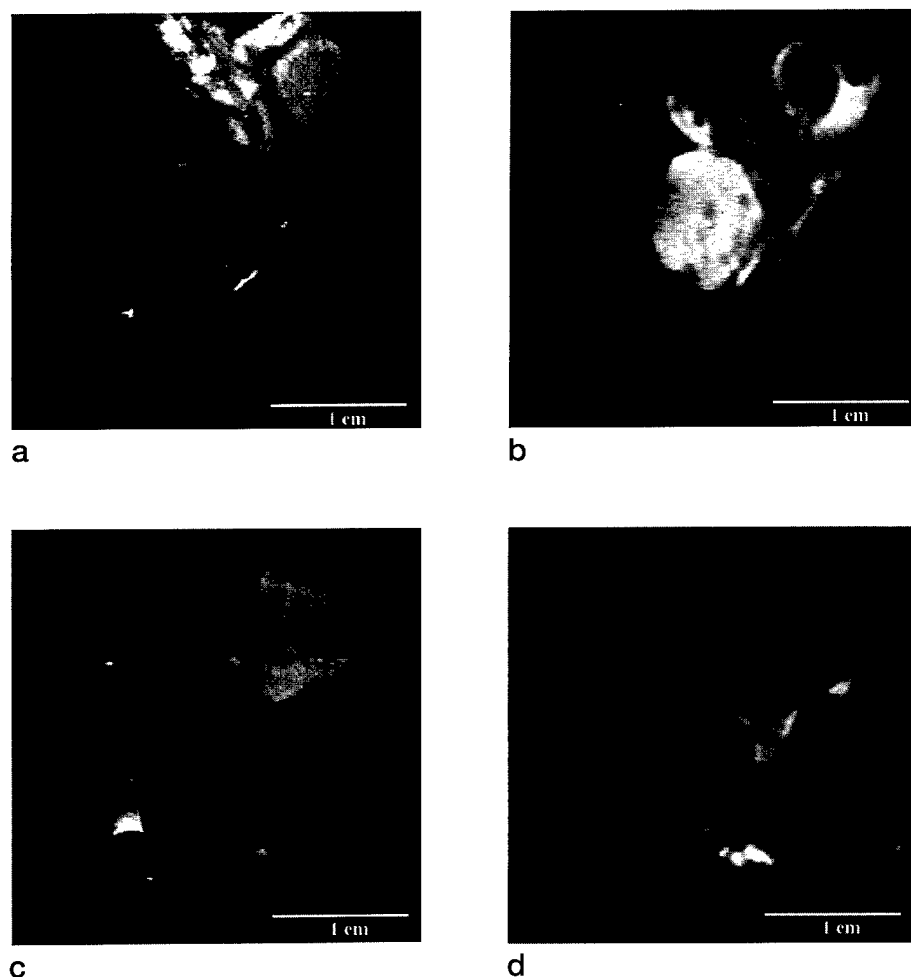


FIG. 2. Representative MR images from implanted breast tumors. (a)  $T_2$ -weighted image of a 4-week-old MCF7 tumor (M3) with 128 phase encodes. (b) Diffusion-weighted image of tumor M3 with  $b = 636 \text{ s/mm}^2$  and 64 phase encodes. (c) A  $T_2$ -weighted image of a 4-week-old T47D tumor (T5) with 128 phase encodes. (d) Diffusion-weighted image of tumor T5 with  $b = 636 \text{ s/mm}^2$  and 64 phase encodes.

4- $\mu\text{m}$  thick slices from each section were stained with Hematoxylin-Eosin and by using a modified trichrome technique to stain mucopolysaccharides of fibrous tissue.

## RESULTS

In previous work in our laboratory (5, 15–17), we studied a tumor model where breast cancer cells were implanted in the mouse flank. Tumors from both cell lines that were studied in this work developed faster in the mammary fat pad than had previously been observed in the flank. Average ages and diameters for the 10 tumors included in this study are given in Table 1. After 4 weeks, most of the tumors had reached a size of 0.5–1.0 cm in diameter. In 6- to 8-week-old tumors, it was possible to see regions of necrosis, usually near the center of the tumor. These could be observed both on the  $T_2$ -weighted images, and on the highly diffusion-weighted images. After 11 weeks, one of the MCF7 tumors had reached a size of 2.5 cm in diameter, and developed a large necrotic core. More ne-

crosis was present in the T47D tumors than in MCF7 tumors having similar age and size.

Typical image signal-to-noise for viable tumor ranged from 60:1 on  $b = 0 \text{ s/mm}^2$  images to 40:1 on  $b = 754 \text{ s/mm}^2$  images (where the noise was estimated from the standard deviation in a ROI in the background). Areas of necrosis could be identified as having increased signal intensity on the  $T_2$ -weighted images (15, 16), and reduced signal intensity on the higher diffusion-weighted images. MCF7 and T47D tumors had similar appearances for all imaging sequences. Representative images are shown in Fig. 2. Figures 2a and 2b show a 4-week-old MCF7 tumor (M3), where Fig. 2a is a high-resolution  $T_2$ -weighted image, and Fig. 2b is a lower resolution diffusion-weighted image ( $b = 636 \text{ s/mm}^2$ ). Figures 2c and 2d show a 4-week-old T47D tumor (T5) for comparison.

Motion artifacts due to breathing were visible in the upper abdominal region, but very little phase-smearing was observed in the region of the tumor. Motion of the tumor occurring between scans was limited to a few pixels over the entire set of  $b$  values. This motion was qualitatively evaluated by outlining the tumor on

the  $b = 0$  image, and displaying this outline on subsequent images.

Mean ADCs were calculated for viable and necrotic regions within the tumors to determine the specificity of the ADC for characterizing the tissue. Figure 3a shows typical ROIs defined on a high-resolution  $T_2$ -weighted image in water, viable tumor, and necrotic tumor for a 3-week-old T47D tumor ( $T_2$ ). A histological section stained with H&E corresponding to this image is shown in Fig. 3b. The beginning of necrotic regions near the center of the tumor is evident even though this tumor is relatively young. A semilog plot of the mean signal intensities within these ROIs is shown in Fig. 3c. 200 $\times$  magnification views of hematoxylin-eosin-stained histological sections corresponding to these regions are shown in Figs. 3d and 3e. Figure 3d shows a region of viable tumor and Fig. 3e corresponds to the necrotic center of the tumor.

ROIs were defined in viable and necrotic tissue on as many slices as possible (as selected on the  $T_2$ -weighted images) and mean ADCs for these regions are shown in

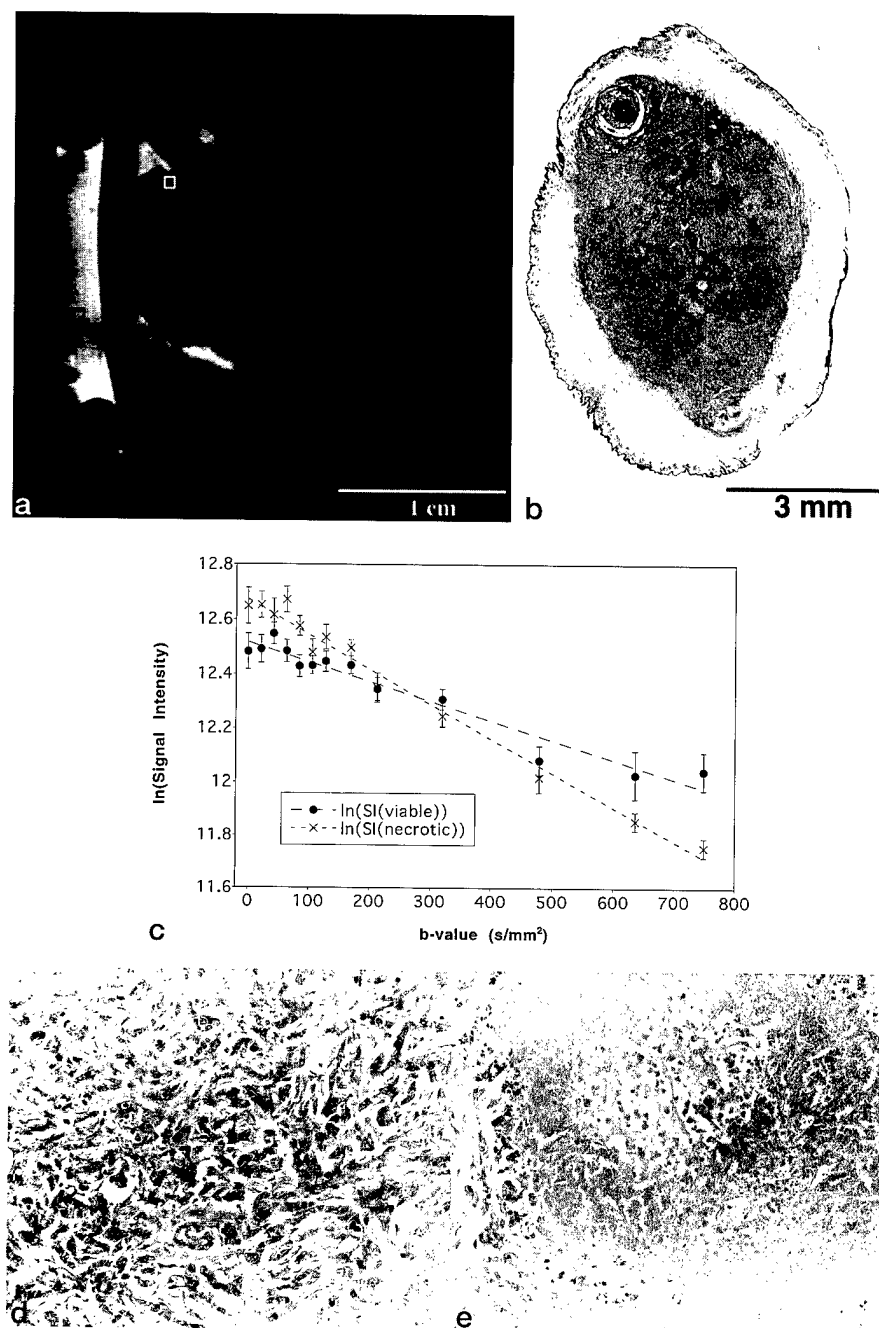


FIG. 3. (a)  $T_2$ -weighted image of a 3-week-old T47D tumor (T2). Typical ROIs are shown outlining regions containing water, viable tumor (white), and necrosis (black). (b) Low-magnification view of a H&E-stained histological section corresponding to this image. Areas of necrosis are marked with arrows. (c) Mean signal intensities within these ROIs for  $b = 0$  to  $754 \text{ s/mm}^2$ . (d)-(e)  $200\times$  magnification views of the H&E-stained sections corresponding to viable tumor and necrosis, respectively.

Table 1. The standard error in the mean for these measurements is reported as the experimental uncertainty. Water ADCs were calculated as a reference for each tumor, and reflect the range of temperatures within the bore for the experiments. The signal decay from the water standards was highly linear. No attempt was made to correct measured ADCs in tumors for temperature, since the tumor is assumed to be affected little by the ambient temperature. The results show a well-defined separation

between ADCs of necrosis and viable tissue for all T47D tumors ( $P < 0.02$  using a Mann-Whitney Rank Sum Test). Since easily identifiable necrotic regions were present only on two MCF7 tumors, no statistical test was performed to compare between necrotic and viable tumor for MCF7. There was no statistically significant difference in calculated ADCs of viable tumor between MCF7 tumors and T47D tumors ( $P > 0.05$  using a standard  $t$  test).

ADC maps were calculated from a straight-line fit of the natural logarithm of the signal intensity to the diffusion-weighting  $b$  factor on a pixel-by-pixel basis. These maps show significant contrast between areas of necrosis and areas of viable tumor, and provide a highly detailed representation of gross tumor morphology. Representative ADC maps are shown in Fig. 4. Figures 4a and 4b show one slice from an 8-week-old MCF7 tumor (M4), which has begun to develop small regions of necrosis near its center. Figure 4a is an ADC map, while Fig. 4b shows a histogram with the distribution of ADCs within the tumor. The results from an older, 11-week-old MCF7 tumor (M5) with a large necrotic center are shown in Figs. 4c and 4d. Two distinct peaks corresponding to the viable and necrotic areas are visible in the histogram for this tumor. These ADC maps show good correlation with gross morphological features of the tumors, as observed on the histological slices. No consistent biexponential signal decay could be observed within the tumor, even in regions showing high vascularity on histology where the contribution to the signal from blood

flowing in the microcirculation would be expected to be strongest. In many pixels, a signal increase was observed at low  $b$  values, likely indicating that small macroscopic motions had occurred between scans.

## DISCUSSION

Tumors from both cell lines grew faster and larger in the mammary fat pad than had previously been observed in

Table 1  
Measured Apparent Diffusion Coefficients for Regions of Interest in T47D and MCF7 Human Breast Tumors

Tumor	Diameter (cm)	Apparent Diffusion Coefficients		
		Water (10 <sup>-3</sup> mm <sup>2</sup> /s)	Necrosis (10 <sup>-3</sup> mm <sup>2</sup> /s)	Viable tumor (10 <sup>-3</sup> mm <sup>2</sup> /s)
T47D				
T1 (3 weeks) <sup>a</sup>	1.0	2.10 ± 0.07 <sup>b</sup>	2.00 ± 0.07	0.68 ± 0.03
T2 (3 weeks)	1.0	2.55 ± 0.02	1.46 ± 0.06	0.69 ± 0.06
T3 (4 weeks)	0.4	2.52 ± 0.04	1.57 ± 0.08	0.49 ± 0.01
T4 (4 weeks)	0.5	2.35 ± 0.02		0.51 ± 0.07
T5 (5 weeks)	1.0	2.36 ± 0.03	1.49 ± 0.12	0.49 ± 0.04
Mean value			1.63 ± 0.12	0.57 ± 0.05
MCF7				
M1 (4 weeks)	0.7	2.34 ± 0.18		0.47 ± 0.02
M2 (4 weeks)	0.8	2.49 ± 0.07	1.26 ± 0.08	0.44 ± 0.05
M3 (4 weeks)	1.0	2.32 ± 0.10		0.48 ± 0.04
M4 (8 weeks)	1.5	2.36 ± 0.08		0.49 ± 0.02
M5 (11 weeks)	2.5	2.25 ± 0.05	1.30 ± 0.12	0.43 ± 0.04
Mean value			1.28 ± 0.02	0.46 ± 0.01

<sup>a</sup> The tumor age refers to the time from day of implantation to the day of measurement.

<sup>b</sup> The standard deviation of pixel intensities within the ROI is reported as the measured uncertainty. For all ROIs,  $n > 25$  pixels.

the flank. MCF7 tumors grew faster and to a larger size than corresponding T47D tumors in this study. We hypothesize that this is due to better nutrient and oxygen delivery, as a result of increased vascularity in MCF7 tumors. More blood vessels were apparent on histology in MCF7 tumors than T47D. In general, more necrosis was present in T47D tumors, and even highly necrotic regions in the MCF7 tumors contained more cellular debris, and islands of viable tumor cells, indicating more recently formed necrosis.

Measured ADCs were highly specific for necrotic and viable tumor in both MCF7 and T47D tumors. The higher diffusion rates in necrotic areas reflect increased volume of extracellular space and increased mobility of water molecules in the extracellular compartment. The tortuosity of the extracellular compartment is reduced in necrosis compared with viable neoplastic tissue due to the decreased density of cells. Additionally, the relative volume fraction of water in the extracellular space is greatly increased in necrotic regions due to cell lysis. In addition to being specific for identification of necrotic regions, it is plausible that the measured ADC is an indication of the stage of the necrosis. In initial stages of the formation of necrosis, the cells and cytoplasmic compartments swell and the nucleus may shrink and become fragmented. After disruption of the cell membrane, the cell contents are released and cellular details are lost. This results in the appearance of sparsely distributed nuclear dust, membrane fragments and proteins. In addition, in most cases we could observe islands of still viable cells within the necrotic regions. However, the spatial variation of these morphologically distinct features occurs on a scale much smaller than the slice

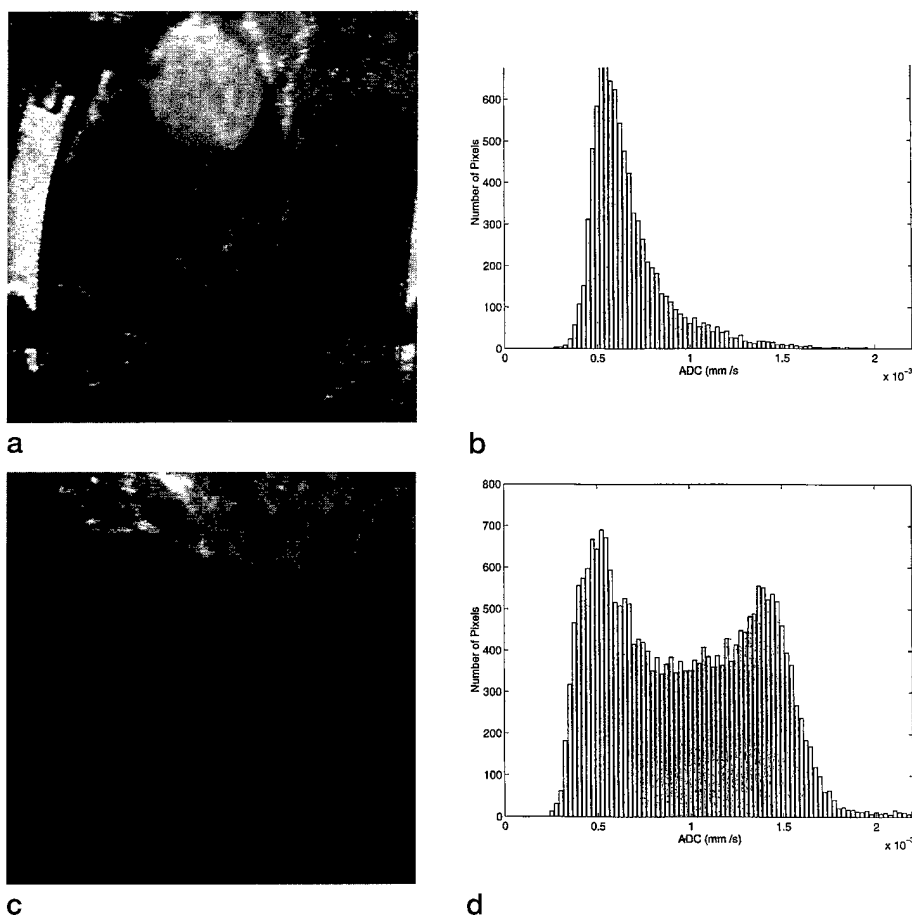


FIG. 4. (a) ADC map of an 8-week-old MCF7 tumor (M4), which has begun to develop small regions of necrosis near its center (areas of high signal intensity). (b) Histogram showing the distribution of ADCs within the tumor. (c)-(d) The results from an older, 11-week-old MCF7 tumor (M5) with a large necrotic center. (c) ADC map, (d) ADC histogram.

thickness of 1 mm. Therefore, the measured ADC for a pixel may reflect water mobility at all stages of necrosis, as well as in viable tumor.

Although no statistically significant difference was observed between viable tumor in MCF7 and T47D tumors, the measured ADCs in necrotic regions in T47D tumors were higher than in corresponding necrotic regions in MCF7 tumors. This is consistent with what is expected from partial volume effects since the necrosis found in T47D tumors was, in general, more progressed than that found in MCF7 tumors and is therefore expected to be more edematous.

ADC maps showed relatively uniform signal intensities within areas of necrotic and viable tumor, and excellent contrast was observed between necrotic regions within the tumors and areas of viable neoplastic tissue. The maps compared well to gross tumor morphology as evidenced by histological sections corresponding to the images. A more detailed comparison to histology could not be made because of the difference of a factor of 200 in slice thickness between the MR images and histological slices. The existence of small macroscopic motions of the tumor occurring between scans during the long examination times precluded an investigation of IVIM effects for this data.

The results suggest that diffusion-weighting imaging, with an appropriate choice of weighting parameters could provide a valuable noninvasive technique for characterizing tumor response to therapy. Currently, locally advanced cancer is managed by using a combined modality treatment including multiagent chemotherapy, surgery, and radiation. Unfortunately, the response of the tumors to these therapies is highly variable, and not well-predicted, making individual treatment planning a very difficult problem. Tumor response to therapy is evaluated conventionally by a combination of clinical examination and x-ray techniques. However, tumor response in the form of cell death and necrosis precedes changes that can be detected by using these methods, and in many cases, a large degree of necrosis can occur with no detectable change in size or radiographic appearance. With the development of specialized gradient coil hardware to provide adequate diffusion weighting (18), it is likely that diffusion imaging by using MR can be used in a clinical setting to more efficiently monitor tumor response to therapy.

## CONCLUSIONS

We have applied MR diffusion imaging techniques to human breast cancer implanted in nude mice. The results of this study indicate that the ADC as measured by using a PGSE sequence is specific for necrosis and viable tumor. Maps of the ADC reflected well the gross morphological features of the tumors as revealed by histological examination. The results indicate potential for characterizing solid tumors by using diffusion imaging, and may have implications for monitoring tumor response to therapy.

## ACKNOWLEDGMENTS

The authors thank Dov Grobeld for computer programming.

## REFERENCES

1. K. G. Helmer, B. J. Dardzinski, C. H. Sotak, Time dependent diffusion in RIF-1 tumors: in vivo extraction of geometrical parameters and identification of necrosis, in "Proc., SMR, 2nd Annual Meeting, San Francisco, 1994," p. 1044.
2. J. Dunn, S. Ding, J. O'Hara, K. Liu, E. Rhodes, J. Weaver, H. Swartz, The apparent diffusion coefficient measured by MRI correlates with  $pO_2$  in a RIF-1 tumor. *Magn. Reson. Med.* **34**, 515-519 (1995).
3. M. Zhao, J. G. Pipe, J. Bonnett, J. L. Evelhoch, Early detection of treatment response by diffusion-weighted  $^1H$ -NMR spectroscopy in a murine tumor in vivo. *Br. J. Cancer* **73**, 61-64 (1996).
4. M. Eis, T. Els, M. Hoehn-Berlage, High resolution quantitative relaxation and diffusion MRI of three different experimental brain tumors in rat. *Magn. Reson. Med.* **34**, 835-844 (1995).
5. E. Furman, R. Margalit, P. Bendel, A. Horowitz, H. Degani, In vivo studies by magnetic resonance imaging and spectroscopy of the response to tamoxifen of MCF7 human breast cancer implanted in nude mice. *Cancer Commun.* **3**, 287-297 (1991).
6. H. Degani, S. M. Ronen, E. Furman-Haran, Breast cancer: spectroscopy and imaging of cells and tumors, in "NMR in Physiology and Biomedicine" (R. J. Gillies, Ed.), pp. 329-352, Academic Press, San Diego, 1994.
7. D. LeBihan, E. Breton, D. Lallemand, P. Grenier, E. A. Cabanis, M. Laval-Jeantet, MR imaging of intravoxel incoherent motions: application to diffusion and perfusion in neurologic disorders. *Radiology* **161**, 401-407 (1986).
8. J. J. Neil, J. H. Ackerman, Detection of pseudodiffusion in rat brain following blood substitution with perfluorocarbon. *J. Magn. Reson.* **97**, 194-199 (1992).
9. D. R. Pickens, D. Jolgren, C. H. Lorenz, J. L. Creasy, R. R. Price, MR perfusion imaging of an excised animal kidney. *Invest. Radiol.* **27**, 287-292 (1992).
10. D. Le Bihan, Intravoxel incoherent motion imaging. in "Diffusion and Perfusion Magnetic Resonance Imaging: Applications to Functional MRI" (D. Le Bihan, Ed.), pp. 270-274, Raven Press, New York, 1995.
11. M. Neeman, J. P. Freyer, L. O. Sillerud, Pulsed-gradient spin-echo diffusion studies in NMR imaging: effects of the imaging gradients on the determination of diffusion coefficients. *J. Magn. Reson.* **90**, 303-312 (1990).
12. M. Eis, M. Hoehn-Berlage, Correction of gradient crosstalk and optimization of measurement parameters in diffusion MR imaging. *J. Magn. Reson.* **107**, 222-234 (1995).
13. M. Neeman, J. P. Freyer, L. O. Sillerud, A simple method for obtaining cross-term-free images for diffusion anisotropy studies in NMR microimaging. *Magn. Reson. Med.* **21**, 138-143 (1991).
14. P. R. Bevington, D. K. Robinson, "Data Reduction for the Physical Sciences," McGraw-Hill Book Company, New York, 1992.
15. H. Degani, E. Furman, S. Fields, Magnetic resonance imaging and spectroscopy of MCF7 human breast cancer: pathophysiology and monitoring of treatment. *Clin. Chim. Acta* **228**, 19-33 (1994).
16. E. Furman-Haran, A. F. Maritzek, I. Goldberg, A. Horowitz, H. Degani, Tamoxifen enhances cell death in implanted MCF7 breast cancer by inhibiting endothelium growth. *Cancer Res.* **54**, 5511-5514 (1994).
17. E. Furman-Haran, R. Margalit, A. F. Maritzek, H. Degani, Angiogenic response of MCF7 human breast cancer to hormonal treatment: assessment by dynamic Gd-DTPA-enhanced MRI at high spatial resolution. *J. Magn. Reson. Imaging* **6**, 195-202 (1996).
18. C.F. Maier, H.N. Nikolov, B.K. Rutt, Practical design of a high-strength gradient coil for diffusion/microvascular imaging of breast tumors, in "Proc., SMR and ESMRMB, 3rd Annual Meeting, Nice, 1995," p. 312.

Best Available Copy

COPY

June 5, 1997

Dear Dr. Fenster:

Your "Application to Use Animals for Research or Teaching" entitled:

"Magnetic Resonance Imaging of Microvascular Blood Flow in a Mouse Melanoma Model"  
 Funding Agency: US Army

has been approved by the University Council on Animal Care. This approval expires in one year on the last day of the month. The number for this project is # 97127-6.

1. This number must be indicated when ordering animals for this project.
2. Animals for other projects may not be ordered under this number.
3. If no number appears on this approval please contact this office when grant approval is received. If the application for funding is not successful and if you wish to proceed with the project, request that an internal scientific peer review be performed by your animal care committee.
4. Purchases of animals other than through this system must be cleared through the ACVS office. Health certificates will be required.

ANIMALS APPROVED

Mice - nu/nu, 4-8 wks, F

- 24

REQUIREMENTS/COMMENTS

Please ensure that individual(s) performing procedures, as described in this protocol, are familiar with the contents of this document.

Procedures in this protocol must be carried out according to the following SOPs. Please contact the Animal Use Subcommittee office (651-2111 ext. 6770) in case of difficulties or if you require copies.

SOPs #100-01: "Monitoring/Tumor Growth/Rodents"  
 #310-01: "Holding Period Post-Admission"  
 #320-01: "Euthanasia"  
 #321-01: "Criteria for Early Euthanasia/Rodents"

1. The nude mice will need to be housed in sterilized housing with sterilized feed and water. Entrance into the room will require proper protective clothing and procedures. Please notify Dr. Martin (651-2111 ext. 3033) well in advance of ordering mice so the necessary arrangements can be made.

c.c. Approved New Protocol - A. Fenster, C. Maier, S. Henderson  
 Approval Letter - C. Maier, S. Henderson, K. Perry



**THE UNIVERSITY OF WESTERN ONTARIO - COUNCIL ON ANIMAL CARE**  
**APPLICATION TO USE ANIMALS FOR RESEARCH OR TEACHING**

**Project Title:** Magnetic Resonance Imaging Of Microvascular Blood Flow in a Mouse Melanoma Model

**New Animal Application** ☒ **or Renewal** • **Protocol Renewal #** \_\_\_\_\_  
**To Take Effect Immediately** **Yes** • **No** ☒ **If NO - What Month** June 1, 1997  
**Principal Investigator:** Aaron Fenster **Phone No.** 663-3834  
**Department:** Imaging Research **Institution:** RRI  
**Office Address:** Imaging Research Labs, RRI

**OTHER PERSONNEL:** (Associated Scientists, Graduate Students, Staff)

<u>Name</u>	<u>Position</u>	<u>Phone</u>
Cynthia Maier	Grad student	663-5777 x4147
Dr. Ravi Menon	RRI Scientist	663-5777 x4148
Dr. Paula Gareau	Post doctoral fellow	663-5777 x4077
Dr. Ian MacDonald	Associate professor	661-3053
Sarah Henderson	Research technician, Anaesthesia	663-5777 x4309

**Emergency Contact:** Cynthia Maier **Work Phone:** as above **Home Phone:** 439-3218  
**Proposed Start Date:** June 1, 1997 **Proposed End Date:** August 31, 1997  
**1. Funding Source:** U.S. Army **Source Grant No.** R50213  
**Grant Title:** Microvascular magnetic resonance imaging for the diagnosis of breast cancer  
**2. Funding Source:** MRC **Source Grant No.** R50119  
**Grant Title:** Development and Validation of 3-dimensional ultrasound imaging for the diagnosis and management of prostate cancer  
**Room Location of:** a) Surgeries b) Procedures: 4T MR Imager  
**This application is for:** research ☒ teaching \_\_\_\_\_ testing \_\_\_\_\_

**C.C.A.C. Category of Invasiveness (See Appendix A)** C  
**Teaching** • **Course Number** \_\_\_\_\_ **Department** \_\_\_\_\_  
**Research** • ☒  
**Testing** • \_\_\_\_\_  
**Acute** • **Chronic** ☒ **Both** • \_\_\_\_\_

**ANIMAL HUSBANDRY:**

**Housing:** **Standard:** \_\_\_\_\_ **or Special Requirements** isolation for nude mice  
**Location of Housing:** Animal Care Facility, UWO Health Sciences, 5th Floor  
**Food/Diet:** **Standard:** X **or Special** \_\_\_\_\_

**ANIMALS REQUESTED:** **SOURCE:** **Standard** ☒ **Other** • \_\_\_\_\_

<u>Animal (strain)</u>	<u>Age/Weight</u>	<u>Sex</u>	<u>No./Expt.</u>	<u>Total/Year</u>
nu/nu	4-8 weeks	F	6	24

A/P  
Janice Koenig



**ANAESTHESIA AND ANALGESIA (list all agents used)**

Preanaesthetic: \_\_\_\_\_  
 General Anaesthetic: Ketamine/xylazine, isoflurane (as per ACVS guidelines)  
 Tranquillizer: \_\_\_\_\_  
 Analgesic: \_\_\_\_\_  
 Other Agents: Nicotinamide  
 Postoperative Care Provided by: \_\_\_\_\_ Phone: \_\_\_\_\_  
 Duration of Survival of Animal: 3-4 weeks  
 Method of Euthanasia: CO<sub>2</sub> inhalation  
 Will film and/or video recording be used? Yes • No **X**  
 If yes, for what purpose? \_\_\_\_\_  
 What will be photographed/videoed? \_\_\_\_\_

**BRIEF LAY SUMMARY OF PROJECT:** Describe concisely in lay terms: a) the purpose of the project; b) the expected benefit; c) the reason for using animals; and d) the reason for using the species requested. Separate applications should be submitted for significantly different purposes to facilitate data compilation and review:

a) Purpose: The purpose is to develop new Magnetic Resonance Imaging techniques for measuring blood flow in tumor microcirculation. b) Expected Benefit: New microvessel formation in tumors (angiogenesis) has been shown to correlate with invasiveness and patient prognosis for breast cancer, prostate cancer, and colorectal cancers. A non-invasive technique for detecting these new blood vessels could yield important prognostic information prior to surgery, enabling improved patient management. c) Reason for Use of Animals: It is not possible to mimic blood flow in such small vessels using *in vitro* methods. This necessitates the use of an animal tumor model. d) Reason for Using Species: A high degree of tumor vascularity is necessary because it is very difficult to detect such small flows using MRI. The higher the vascular volume, the stronger the expected signal. B16F1 melanoma cells will be used since they are well-characterized and form rapidly growing, highly vascularized tumors. We will use athymic nude mice to ensure rapid primary melanoma growth.

**EXPERIMENTAL METHOD:** Use up to a maximum of four typed inserted sheets for:

1. A Detailed Summary of the Proposal:

On the first page provide a summary outlining: a) rationale; b) hypothesis; c) objective(s); d) approach and research plan; and e) the rationale for the numbers of animals requested. Grant summary pages are acceptable.

2. A Description of the Experimental Procedures:

On the remaining pages, provide additional detailed descriptions of the animal use. Divide into experiments. For each experiment, detail: a) all aspects of housing and feeding; b) all procedures performed on animals in each group; c) any agents or procedures which have the potential to cause pain and/or pronounced debilitation; d) anaesthetic and analgesic regimes, if applicable, including dose, route, frequency and duration. If animals are to be used chronically, detail: e) post operative care; f) frequency of monitoring; g) the endpoint of animal use; and h) criteria which will be used to euthanize animals prior to the endpoint. Grant pages are not acceptable.

## **1. A Detailed Summary of the Proposal:**

**a) Rationale:** We wish to develop IVIM imaging techniques for measurement of tumor blood flow using an animal tumor model. We will use a mouse melanoma cell line implanted in nude mice. This cell line is known to form well-vascularized tumors rapidly. A high degree of vascularity is necessary due to the technical difficulty of measuring a MR signal from blood flowing in small vessels.

**b) Hypothesis:** Recently, MRI has been used to acquire high-resolution, three-dimensional images of the brain that are sensitive to blood flow in very small vessels using a technique known as Intravoxel Incoherent Motion Imaging (IVIM). Human cancers are known to stimulate the growth of new blood vessels in the peripheral normal tissue. The degree to which this new blood vessel formation occurs has been shown to correlate strongly with the invasiveness of the primary tumor. This neovascularization is different from normal microvasculature both in the geometry of individual vessels and in spatial patterns of vessel formation. It is our hypothesis that the distinctive anatomical vascular patterns and flow properties associated with tumor neovascularization can be exploited using IVIM to provide valuable prognostic information.

**c) Specific Objective:** Optimize new MRI Intravoxel Incoherent Motion (IVIM) techniques for sensitivity to blood flow in tumor microvessels, i.e. vessels <100 micrometers in diameter.

**d) Approach and Research Plan:** We will perform IVIM imaging in a mouse melanoma model that is known to be highly vascularized. Performing these experiments in an animal tumor model will: (a) allow very high spatial resolution, high signal-to-noise MR images and therefore very accurate IVIM measurements, (b) allow longer total examination times than would be practical in humans (c) permit direct manipulation of tumor blood flow. The specific purpose of these experiments will be to identify a relationship between MR signal and microvessel blood flow on an IVIM exam. This will be accomplished by continuous acquisition of a series of MR images with identical IVIM-weighting throughout a period in which the blood flow is increased dramatically following a bolus injection of the vasodilator Nicotinamide. Nicotinamide is known to increase tumor blood flow significantly approximately 15-20 minutes after an intraperitoneal injection, and a concomitant modulation of the MR signal arising from flow in the microvasculature is expected. This modulation of blood flow will allow a unique identification of the fraction of total MR signal that originates from the microvasculature, and a map of microvessel distribution can therefore be calculated.

**e) Rationale for Number of Animals Requested:** 4 groups of 6 mice each will be injected with cancer cells. These groups of mice will be treated identically, however, it is necessary to treat one group at a time due to availability of MRI time. Injections with tumor cells for each group will be staggered by 3 weeks to provide continual availability of mice with tumors that are of a size ideal for MR imaging; the MR imager is a shared resource and experiment time must be reserved well in advance. It is expected that tumors will have a size of approximately 0.7-1 cm in diameter at 2-3 weeks post injection of cells. It is estimated that 15-20 animals will be required for statistical significance; an additional 4 animals are requested to allow optimization of experimental parameters related to the MRI image acquisition.

## 2. A Description of the Experimental Procedures:

a) Housing and Feeding: Mice will be housed in microisolator cages at the 5th floor animal facility in the UWO Health Sciences building. They will be provided with food and water *ad libitum*.

b) - h) Procedures involving Animals: Mice will be purchased in 4 groups of 6 each (with arrival dates staggered at 3 week intervals), and will be allowed to acclimatize for 1 week prior to injection with B16F1 melanoma cells. Mice will receive a subcutaneous injection in the flank with  $1 \times 10^5$  cells in a volume of 0.1 ml of medium each. Mice will be monitored every 3-4 days for approximately 1 1/2 weeks or until tumor growth is evident. After this, mice will be monitored daily for their general state of health, and particularly for signs of distress due either to growth of the primary tumor, or to internal metastatic tumors (according to S.O.P. #100-01). Physiological signs (respiratory, appearance, behavior, posture, locomotion, ocular) will be monitored and if signs of distress are evident, early euthanasia will be carried out by CO<sub>2</sub> inhalation according to S.O.P. #320-01.

At 2-3 weeks post implantation, the tumors will have reached a size of about 0.7 - 1 cm in diameter, at which time MR imaging of the tumors can take place. During this period, mice will be removed, one at a time, from the 5th floor facility for MR imaging. Mice will be transported in a covered, ventilated container directly to the RRI 4Tesla MRI facility where they will be anaesthetized using an intraperitoneal injection of Ketamine + Xylazine (100 mg/kg Ketamine + 10 mg/kg Xylazine as recommended by Dr. S.J. Fussell). Tumor size will be measured using calipers. An intraperitoneal catheter (Jelco 25 gauge catheter) will be inserted, and surgical tape used to hold the catheter in place during the MR exam. The mouse will be placed on a small acrylic holder, and surgical tape will be used to hold the mouse in position during the MR exam (without impairing breathing), with particular attention to restraining motion of the tumor-bearing flank. The surgical tape to be used sticks very well only to itself and not to the mouse's skin. The mouse + holder will then be placed in an approximately 7cm diameter acrylic cylinder through which a mixture of oxygen/isofluorane vapour will be circulated (1-2% isofluorane vapour as recommended by Dr. S.J. Fussell). Isofluorane will be used for anaesthetic throughout the 2-3 hour MR examination since it is known to have minimal effect on the cardiovascular system. No painful procedures will be performed; the purpose of the anaesthetic is to allow positioning of the tumour-bearing flank during the imaging protocol. Normal thermia will be maintained during the experiments by wrapping the acrylic cylinder with warm H<sub>2</sub>O packs (maintained at 37 degrees C) and bubblewrap. After initial set-up and localization images (approximately 1 hour), baseline images will be obtained for 15 minutes. For 5/6 mice in each group, Nicotinamide (Sigma Chemical Co. Ltd.) at a dose of 500 mg/kg (dissolved in sterile saline solution at a volume of 0.25 ml/25 gm mouse) will be injected via the IP catheter in a bolus injection. The 6th mouse in each group will be used as a control for the effect of Nicotinamide, where an equal volume of saline solution will be injected instead of the Nicotinamide solution. Images will be continuously acquired throughout and following the injection for 45 minutes (or return to baseline values). Mice will be returned to the 5th floor animal facility and euthanized by CO<sub>2</sub> inhalation according to S.O.P. #320-01 immediately following the experiment.

**SAFETY REQUIREMENTS: DANGERS/HAZARDS**

(If the answer to a heading question is "NO", proceed to the next heading)

**BIOHAZARDS:** Will the animal use involve a biohazard? No

1. Will the proposed animal use involve microorganisms at MRC level 2 or higher (level B and above) \_\_\_\_\_

If yes, identify agents and MRC risk level \_\_\_\_\_

Is this organism infectious to man? \_\_\_\_\_

Route of infection? Handling waste \_\_\_\_\_ Body Excretions \_\_\_\_\_

Aerosol \_\_\_\_\_ Fomites \_\_\_\_\_ Trauma \_\_\_\_\_ Other \_\_\_\_\_

Is the agent zoonotic? \_\_\_\_\_

Is this organism infectious to animals? \_\_\_\_\_

What are the species at risk? \_\_\_\_\_

2. Will proposed animal use involve genetically engineered organisms or cells containing engineered molecules \_\_\_\_\_

If yes, indicate what changes have been effected \_\_\_\_\_

Is this expected to increase the invasiveness, toxicity or tumorigenicity of the agent in the animal? \_\_\_\_\_

3. Will proposed animal use involve human derived cells? \_\_\_\_\_

If yes, specify cell type and origin \_\_\_\_\_

4. What is the route of administration of the biohazardous agent? \_\_\_\_\_

5. How is infected material to be disposed of? \_\_\_\_\_

6. Will animals need to be housed in containment or isolation? \_\_\_\_\_

**CHEMICALS:** Will potentially toxic or carcinogenic substances be used? No

Agent: \_\_\_\_\_ Chemical Form: \_\_\_\_\_

Provide details of the dose and routes of administration and excretion:

**RADIOISOTOPES:** Will radioisotopes be used? No

Will they be present in housed animals? \_\_\_\_\_

Radioisotope Permit Holder: \_\_\_\_\_ Number: \_\_\_\_\_

Radioactive Isotope: \_\_\_\_\_ Chemical Form: \_\_\_\_\_

Dose given to the animal: \_\_\_\_\_ kBq/kg Total (kBq): \_\_\_\_\_

Provide details of the route of administration and excretion:

**RADIATION / X-RAYS / MRI:** Will radiation, X-rays, CT scanning, MR Imaging be employed? Yes

If yes, give details:

Magnetic Resonance Imaging will be performed as described in detail in Part 2 of the Experimental Methods section of this application.

**PREVENTATIVE MEASURES**

For all of the above, describe measures to prevent or reduce the risk:

**SAFETY REVIEW: TO BE REVIEWED AND APPROVED BY APPROPRIATE SAFETY AUTHORITY**

Signature: \_\_\_\_\_

Date: 11/4/97

THE JOHN P. ROBERTS RESEARCH INSTITUTE

**TECHNICAL EXPERIENCE:** Describe briefly the qualifications and experience of personnel with respect to the procedures they will perform on animals. Include the date of the Graduate Course on "Animal Care and Use" and list workshops attended. Please attach one copy of up to three representative reprints of related work carried out by the research team:

Dr. Ian MacDonald, Dept. of Medical Biophysics, will be responsible for injection of the cancer cells into mice. He has extensive experience with this cell line, and in implanting tumors in mice. A recent publication entitled "Intravital Video Microscopy of the Chorioallantoic Microcirculation: A Model System for Studying Metastasis, Microvascular Research 44: 185-199, 1992 " describing related work with the cell line is attached.

Cynthia Maier and Dr. Paula Gareau will perform all MRI experiments and related procedures. Cynthia Maier is a Ph.D. student, and has attended the ACVS Animal Care and Use Workshop (Nov.19-Nov.28): Basic Injections, Rodent Handling, and Rodent Anaesthesia. She recently completed a similar research project at the Weizmann Institute of Science in Israel (See attached publication "Quantitative Diffusion Imaging in Implanted Human Breast Tumors", Magnetic Resonance in Medicine 37: 1997) where she was responsible for all procedures related to animal use (routine care of mice, use of injectable anaesthetic, MR imaging, euthanasia). Dr. Gareau has a Ph.D. from the Dept. of Biomedical Sciences at the University of Guelph. She was previously employed as Research Coordinator/MRI Operator at the MRI Facility in the Ontario Veterinary College (Jan.93 - Jan.97). In this position she was responsible for all animal manipulations relating to their use in studies which used MRI/MRS. This included induction and maintenance of general anaesthesia via injectable and inhalational agents, various injections protocols and catheterizations (iv, ip,sc,im), handling of compressed gases and euthanasia. For initial experiments, Ms. Maier and Dr. Gareau will be assisted by Sarah Henderson, a research technician in the Department of Anaesthesiology, who has 11 years experience anaesthetizing animals with isoflurane and other agents.

**DECLARATION**

1. I believe that the proposed animal use conforms to my stated objectives, will advance knowledge and will employ the best methods on the smallest number of animals to obtain valid information.
2. I believe that, wherever possible, all procedures having the potential to cause pain or stress have been refined and/or reduced to minimize animal discomfort.
3. I confirm that the experimental method accurately describes ALL the proposed animal use. I accept responsibility for procedures performed on animals in this project. All procedures will be carried out by, or under the guidance of, trained and competent personnel using recognized techniques.
4. All animals in this project will be used in compliance with the regulations of The Animals for Research Act of the province of Ontario, the guidelines of the Canadian Council on Animal Care and the policies and procedures of the University of Western Ontario Council on Animal Care.
5. I am aware that the data provided in this protocol will be entered into the Animal Research Protocol Management System and submitted to the Canadian Council on Animal Care.
6. I will ensure that any individual who will perform any procedure(s), as described in this protocol, will be familiar with the contents of this document.

Signature of Principal Investigator: \_\_\_\_\_

Date

*April 9/97***APPROVAL OF ANIMAL USE SUBCOMMITTEE**

Signature of Chair: \_\_\_\_\_

Date

*05.06.97***APPROVAL OF UNIVERSITY COUNCIL ON ANIMAL CARE**

Signature of Executive Officer: \_\_\_\_\_

Date

*L. D. Martin*  
*June 5/97*

(Adopted by UCAC 27/05/93; Senate 08/07/93)